Supplement to aerosol-cloud effects during Saharan dust episodes: The dusty cirrus puzzle

Axel Seifert[1], Vanessa Bachmann[1]Florian Filipitsch[3], Jochen Förstner[1], Christian Grams[4], Gholam Ali Hoshyaripour[4], Julian Quinting[4], Anika Rohde[4], Heike Vogel[4], Annette Wagner[2]and Bernhard Vogel[4]

[1]Deutscher Wetterdienst, Offenbach, Germany
[2]Deutscher Wetterdienst, Hohenpeißenberg, Germany
[3]Deutscher Wetterdienst, Lindenberg, Germany
[4]Institute of Meteorology and Climate Research (IMK-TRO), Karlsruhe Institute of Technology (KIT), Karlsruhe, Germany

This supplement provides additional figures, and thus more detailed insights into the ICON-D2-ART simulations of the Saharan dust events of 2021 and 2022. Most of the plots are similar to the figures presented in the paper but there are also some additional diagnostics, e.g., for ice nucleating particles, ice supersaturation, and radar reflectivity.

1 Validation using surface station data (Ceilometer, Pyranometer)

The retrieval of solar irradiance at the surface from the CERES instrument on board the Aqua and Terra satellites can be challenging in cloudy conditions. Hence, it is desirable to complement the satellite-based validation by the use of surface stations. DWD operates a network of 25 pyranometers in Germany, which can be used for this purpose. Due to the rather short time periods of 5 days we refrain from a decomposition in clear-sky and cloudy for the pyranometer data. Dusty conditions are defined based on ICON-D2-ART dust AOD exceeding 0.1. Figure S1 shows the results for all dust episodes investigated in this study.

DWD also operates a ceilometer network in Germany. Ceilometers are ground-based remote sensing instruments that provide profile-based information on cloud base heights over time. This allows a height-resolved validation of cloud fraction, with the limitation, that cirrus clouds can only be detected properly in the absence of dense clouds below the cirrus. Figure S2 presents the validation results of seven representative stations from DWD's ceilometer network for the period 1-5 March 2021. All simulations except ACI-dusty show a strong underestimation of cirrus cloud fraction in 7-10 km height (Fig. S2a). This underestimation is eliminated by ACI-dusty thanks to the newly developed dusty cirrus parameterization, which leads to a corresponding improvement in the height-resolved MAE (Fig. S2b). Likewise, the overall bias and MAE, accumulated over all height levels, is strongly improved by the ACI-dusty simulation whereas no significant difference exists between the other three simulations. These results support the conclusions based on satellite data as presented in the main paper. As the investigation of cirrus clouds during the other two dusty cirrus events is hindered by widespread mid- and low-level clouds, we refrain from using ground-based ceilometer data for a validation of these events.

Corresponding author: Axel Seifert, axel.seifert@dwd.de

2 Statistical evaluation

Figures S3-S8 show the bias and MAE for each of the six Saharan dust episodes similar to Figs. 6 and 12 of the paper

Figures S9-S15 present bias and MAE for SEVIRI IR and VIS as well as MODIS cloud cover compared to their model equivalents. For SEVIRI we use the symmetric cloud impact factor for the clear-sky/cloudy classification. Overall, this analysis is consistent with the validation using CERES SSF radiative fluxes.

Figure S16-S24 show the scatter plots for the (model-obs) error of the radiative fluxes as function of mineral dust AOD.

3 Dusty cirrus episode of 15-19 March 2022

Figures S25-S28 are similar to the analysis in the paper and provide additional plots of the ICON-ART AOD and SEVIRI images. Figure S29 shows ice and liquid water path for ACI-dusty and ACI. This shows the contribution of the dusty cirrus parameterization to the (total) ice water path (TQI_DIA in the ICON output), which can be quite significant due to the high ice water content of the dusty cirrus. Figure S30 shows some radar reflectivity plots. Here a simple Rayleigh forward calculation is compared with the European Opera composite. Figure S31 shows examples of MODIS cloud cover and corresponding ICON-ART cloud cover. Note that for these and the following plots of the Supplement Aqua and Terra overpasses are combined, i.e., all available satellite data within a 20 min time window is used. These combined Aqua and Terra datasets are also used for the CERES statistics of this study. Figures S32-S34 are the radiative fluxes of additional Aqua/Terra overpasses. A more complete set of vertical profiles from radiosondes is shown in Figs. S35-S38.

Figure S39 shows a scatter plot of the ice saturation ratio for radiosondes and corresponding ICON-ART profiles. This would require a more detailed investigation, but it shows no obvious bias for the 'no dust' and ARI simulations. In contrast, the ice supersaturations for ACI and ACI-dusty are low biased compared to the observations, especially for $s_i > 1$. This suggests that the ice nucleating ability of the mineral dust, or the dust concentrations, are overestimated by the model.

Figure S40 shows the ice particle concentration as a function of temperature and ice saturation ratio. The dashed line is the water saturation and the dotted line is the homogeneous nucleation threshold. Ice particle concentration due to heterogenous INPs is shown in blue to green colors, whereas yellow to purple indicates ice formation due to homogeneous nucleation. For ARI there is no difference between clean (AOD < 0.05) and dusty (AOD > 0.1). The fact that homogeneous nucleation events are much more frequent for dusty grid points is a spurious correlation because the dust has no microphysical effect in the ARI simulation. The homogeneous nucleation events occur within the frontal zone that also carries the dust. For ACI and ACI-dusty heterogeneous, ice nucleation is drastically increased in the dusty air mass and homogeneous nucleation is strongly suppressed.

The implementation of the INAS ice nucleation scheme in the 'no dust' simulation assumes a constant dust background with three lognormal dust modes. The dust number densities of the three modes are $1\times10^3\mathrm{m}^{-3}$, $1\times10^3\mathrm{m}^{-3}$ and $1\times10^2\mathrm{m}^{-3}$, the mean diameters are chosen as 0.2×10^{-6} m, 0.4×10^{-6} m and 0.6×10^{-6} m, and the standard deviations of the three lognormal modes are 1.7, 1.6 and 1.5, as in ICON-ART. For simulations with prognostic dust, the total surface area of this constant background is used as a lower threshold for the input to the INAS scheme.

4 Dusty cirrus episode of 1-5 March 2021

Figures S41 to S53 provide plots and diagnostics for the Saharan dust event of early March 2021 with the dusty cirrus on 3 March 2021. Unfortunately, some SEVIRI data is missing in the DWD database for this event, which limits the number of plots that can be shown here. The comparison with radiosondes has not been shown in the paper, but some interesting examples are given in Figs. S49-S53.

5 Dusty cirrus case of 4-8 May 2022

Figures S54 to S64 give an overview of the dust event of early May 2022. The dust AOD shows the stationary dust plume over the Alpine region during 5-6 May 2022. During summer 2022 ICON-ART developed a too high dust background in the northern hemisphere, which explains the fact that there is dust everywhere during this period. This has later been corrected with a revised dust emission scheme but is still present in these simulations. This dust background does not affect the dusty cirrus. The comparison with radiosondes in Figs. S63-S64 shows mixed results, sometimes ACI is better for this case, sometimes ACI-dusty.

6 Saharan dust episode of 21-25 Feb 2021

Figures S65 to S76 show the results for the Saharan dust event of 21-25 Feb 2021. No evidence of dusty cirrus formation was found during that period, although the dust AOD exceeds 0.5 over significant areas of the model domain, especially on 22 Feb. There are very few signs of a dusty cirrus in the ACI-dusty simulation and, hence, no significant difference between ACI and ACI-dusty. Only the profiles of Idar-Oberstein in Fig. S76 show a spurious dusty cirrus formation in ACI-dusty.

7 Saharan dust episode of 27 April - 1 May 2022

The dust episode of late April 2022 shown in Figs. S77 to S87 has only moderate dust AOD, but ACI-dusty simulates an enhanced cirrus cloud formation during that period. In most diagnostics the ACI looks more realistic than ACI-dusty, but, for example, the sounding from Trappes on 28 April (Fig. S86) is better matched by ACI-dusty.

8 Saharan dust episode of 18-22 June 2021

In June 2021 deep convection was influenced by Saharan dust (Figs.S88-S101). Hence, this event differs from the other dust episodes in this study. Convection developed mostly at the boundary between the two air masses, but not so much in the region of the highest AOD. Nevertheless, a subjective comparison with satellite data suggests an overestimation of dusty cirrus in ACI-dusty, e.g., on 20 June 12 UTC over northern Italy, Austria, and Bavaria. Due to the convective nature of this event, validation with sparse radiosonde data is difficult. For San Pietro Campofiume (Italy, Fig. S97) the ACI-dusty simulation is slightly better than ACI, no difference is visible for Munich (Bavaria, Fig. S98), and for Kümmersbruck (Bavaria, Fig.S99) ACI-dusty is again better. Hence, while the satellite data suggests advantages for ACI and spurious dusty cirrus in ACI-dusty, the radiosondes do not necessarily confirm this and often show a good match with ACI-dusty.

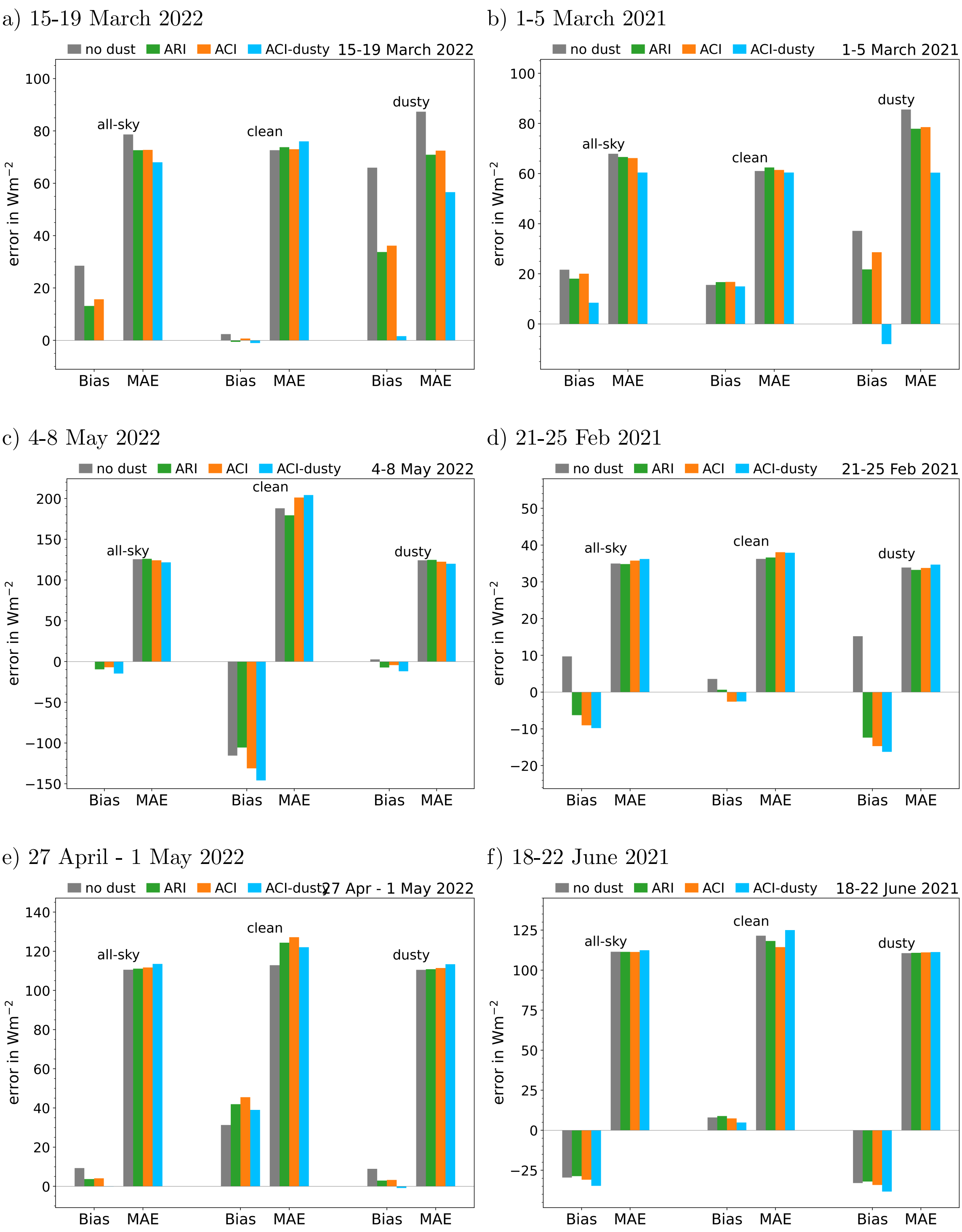

Figure S1. Validation of solar irradiance at the surface using DWD's pyranometer network for the six individual dust episodes

a) Bias (ceilometer profile)

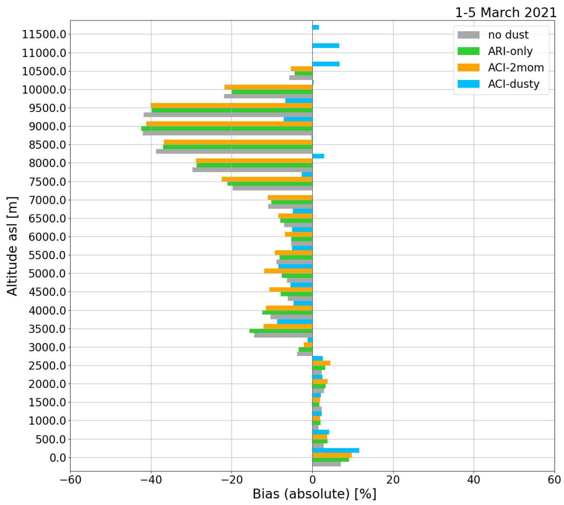

b) MAE (ceilometer profile)

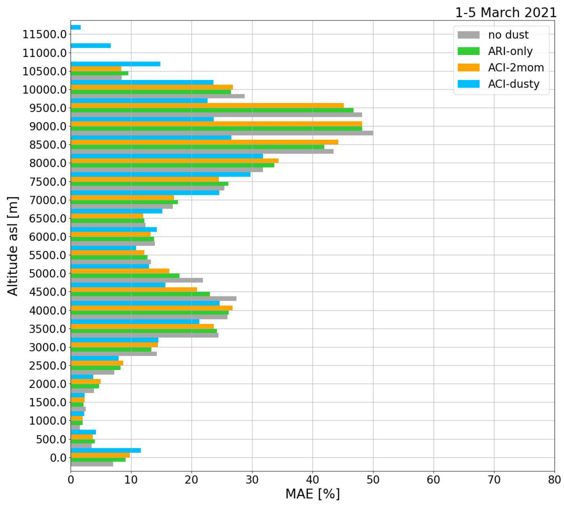

c) Bias (all heights)

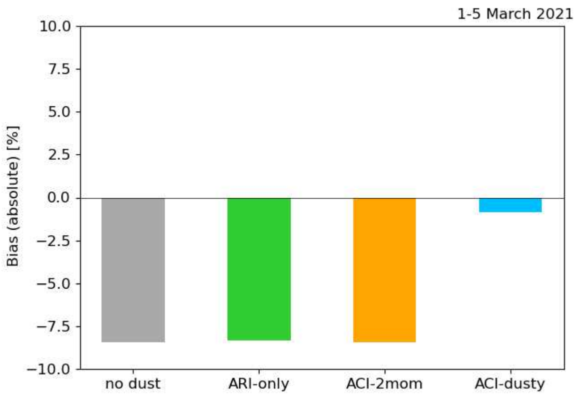

d) MAE (all heights)

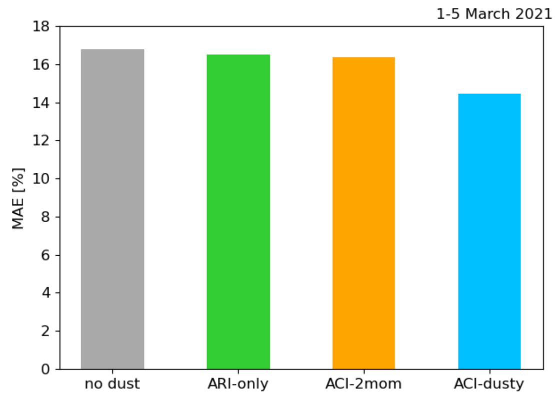

Figure S2. Validation of cloud fraction with ceilometer data of 7 representative stations in Germany (Hohenpeissenberg, Lindenberg, Leipzig, Stuttgart, Oberschleissheim, Meiningen, and Konstanz) during the dusty cirrus event from 1-5 March 2021. To focus on the dusty cirrus occurrence, we use ICON-ART AOD greater 0.1 as a filter.

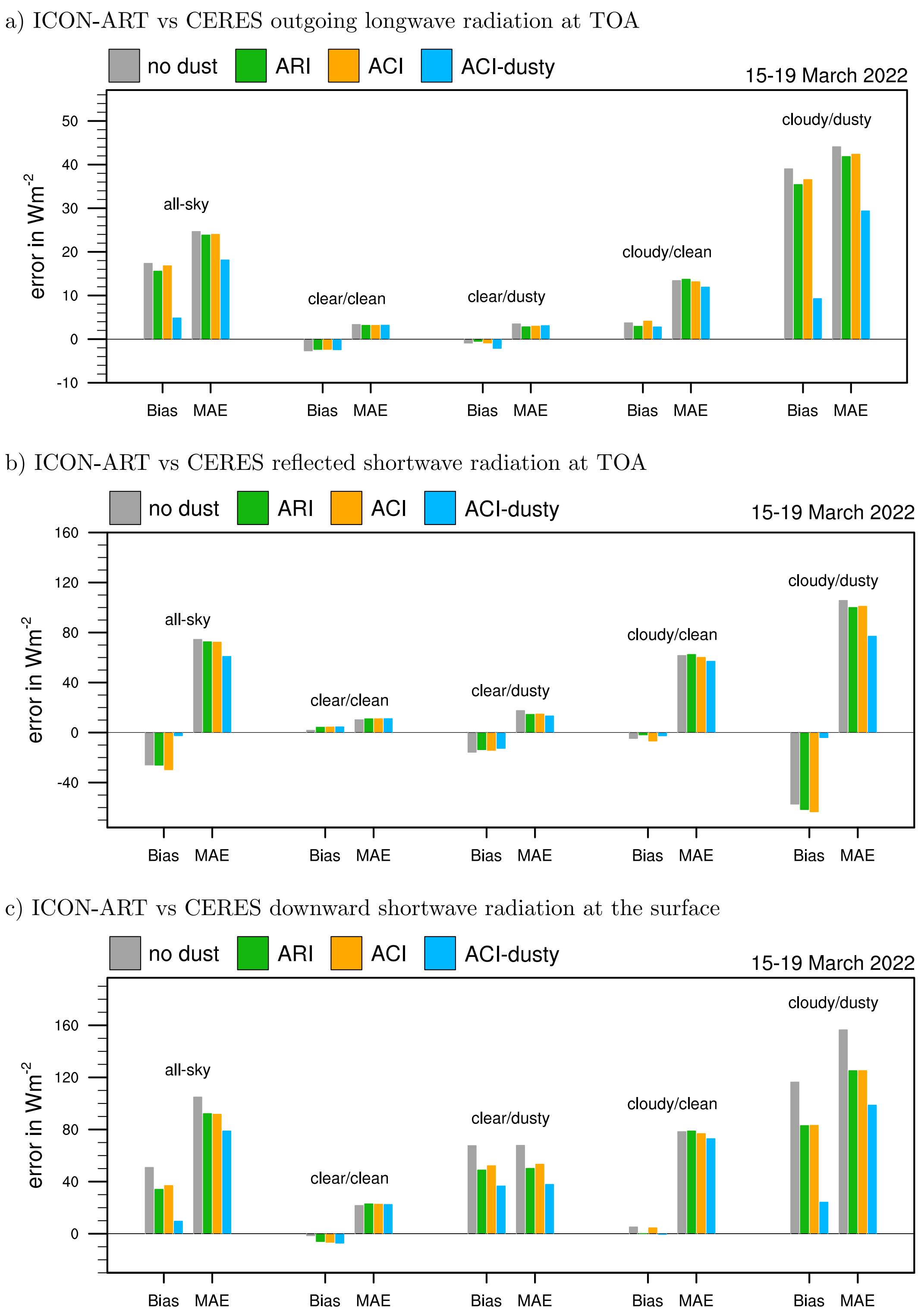

Figure S3. Bias and mean absolute error (MAE) of ICON-ART compared to CERES SSF level 2 radiative fluxes for 15-19 March 2022. Shown are the outgoing longwave radiation at the top of atmosphere (TOA), the reflected shortwave at TOA and to solar irradiance at the surface (from top to bottom)

a) ICON-ART vs CERES outgoing longwave radiation at TOA

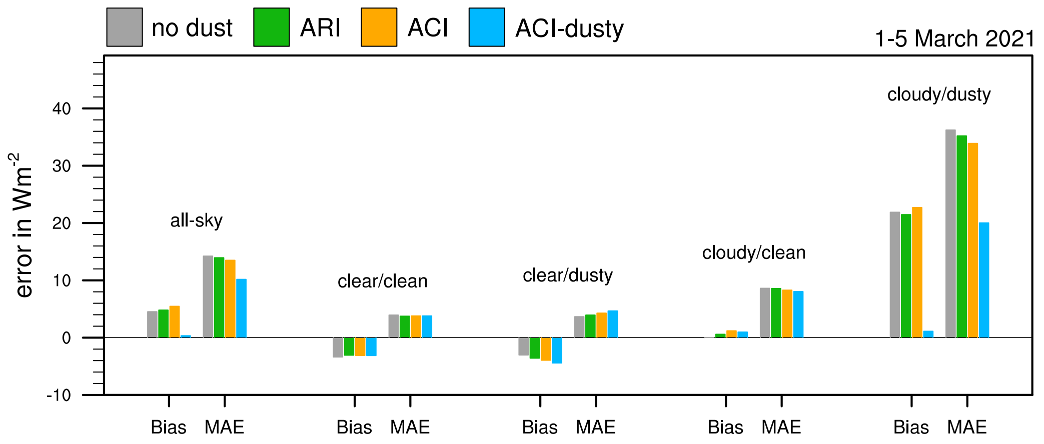

b) ICON-ART vs CERES reflected shortwave radiation at TOA

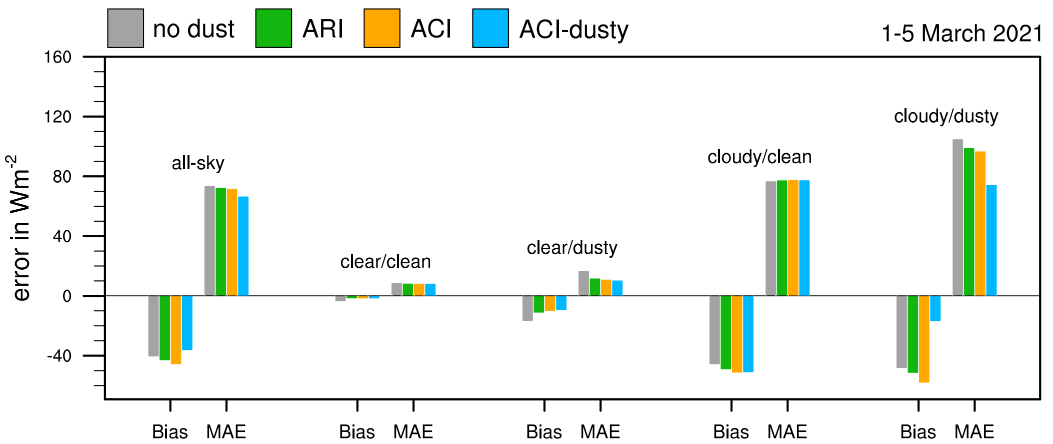

c) ICON-ART vs CERES downward shortwave radiation at the surface

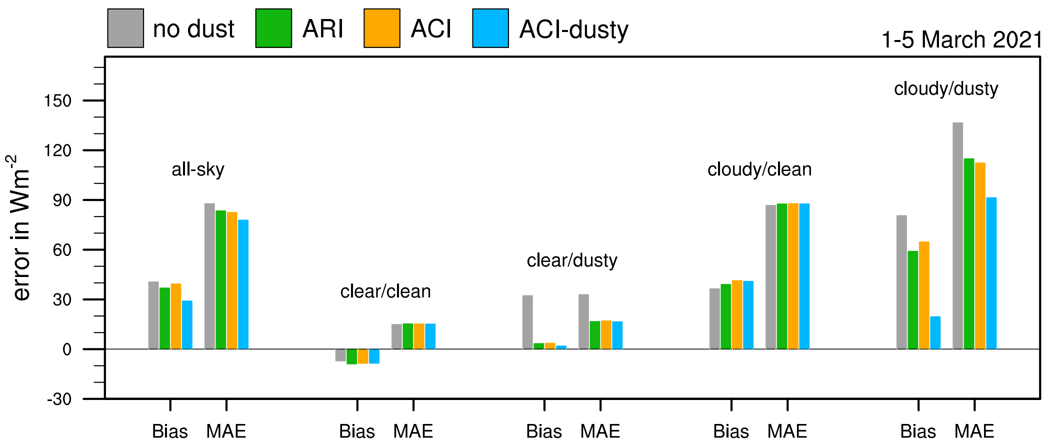

Figure S4. Bias and mean absolute error (MAE) of ICON-ART compared to CERES SSF level 2 radiative fluxes for 1-5 March 2021. Shown are the outgoing longwave radiation at the top of atmosphere (TOA), the reflected shortwave at TOA and to solar irradiance at the surface (from top to bottom)

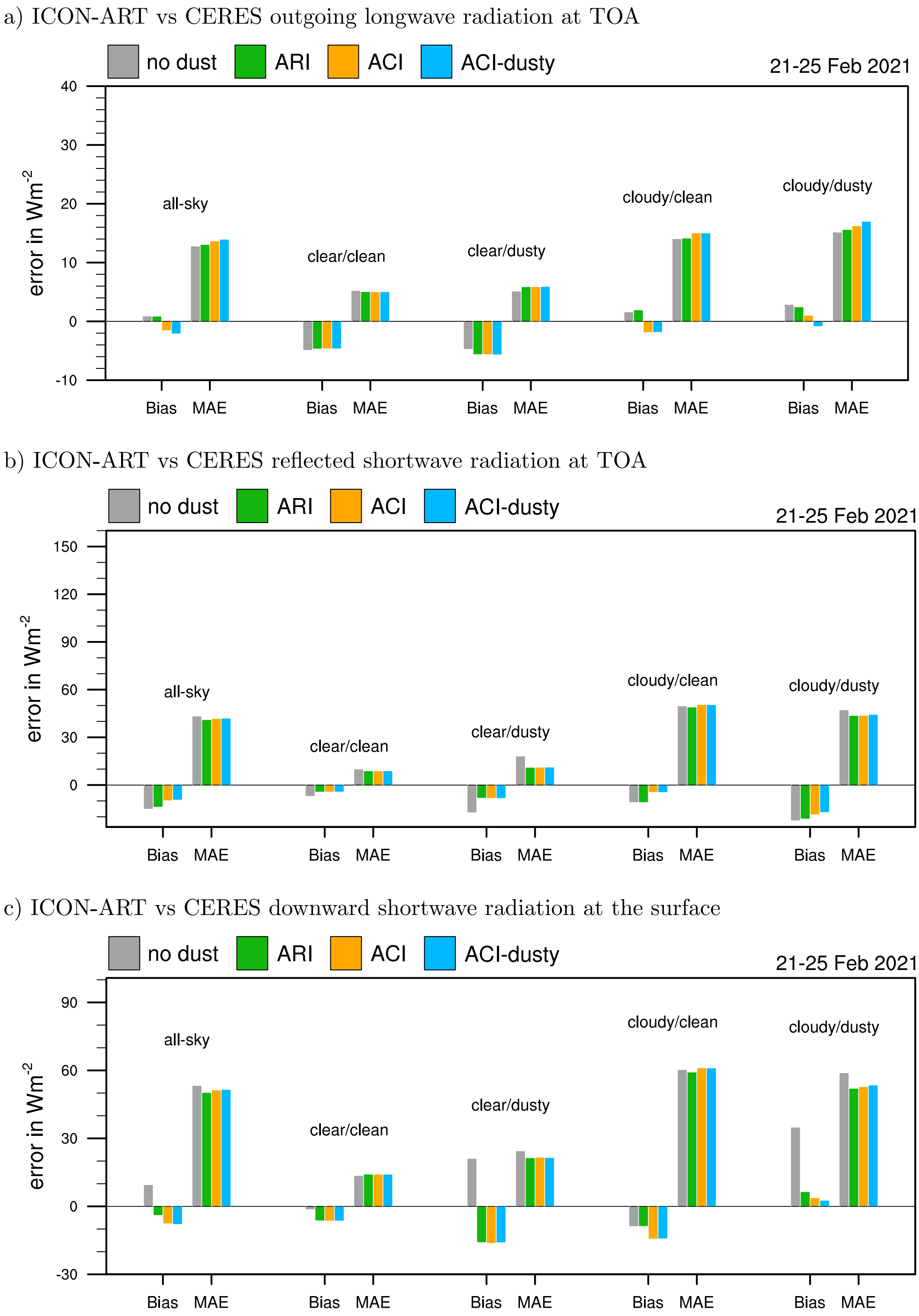

Figure S5. Bias and mean absolute error (MAE) of ICON-ART compared to CERES SSF level 2 radiative fluxes for 21-25 Feb 2021. Shown are the outgoing longwave radiation at the top of atmosphere (TOA), the reflected shortwave at TOA and to solar irradiance at the surface (from top to bottom)

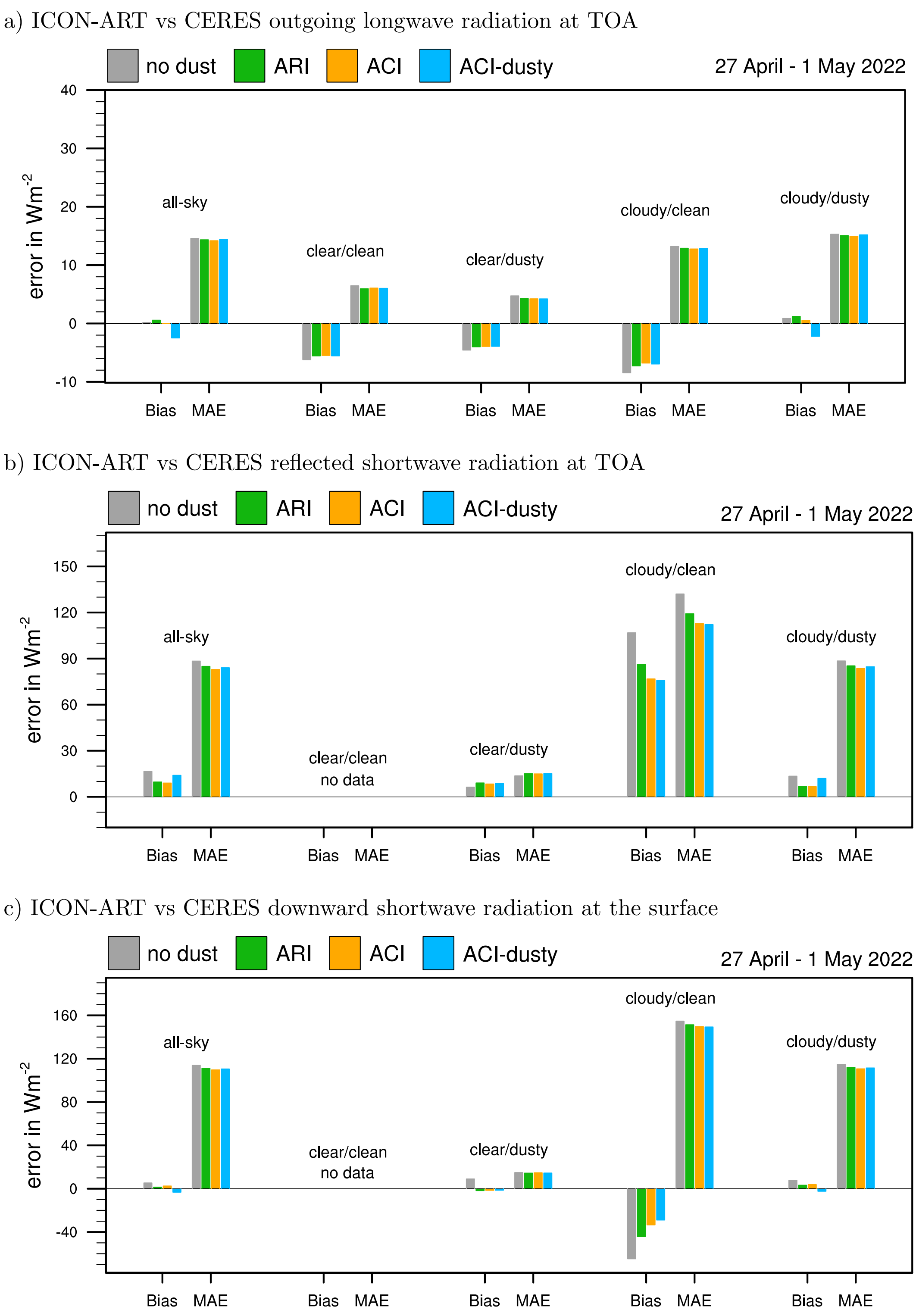

Figure S6. Bias and mean absolute error (MAE) of ICON-ART compared to CERES SSF level 2 radiative fluxes for 27 April to 1 May 2022. Shown are the outgoing longwave radiation at the top of atmosphere (TOA), the reflected shortwave at TOA and to solar irradiance at the surface (from top to bottom)

a) ICON-ART vs CERES outgoing longwave radiation at TOA

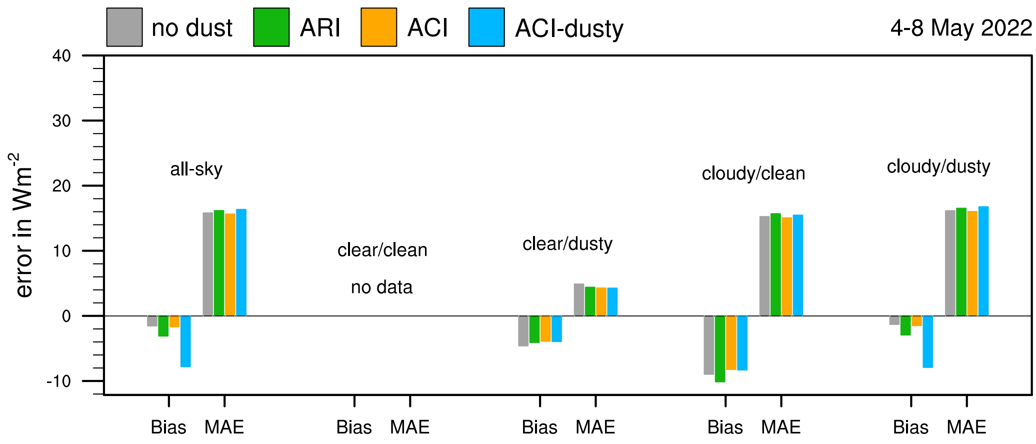

b) ICON-ART vs CERES reflected shortwave radiation at TOA

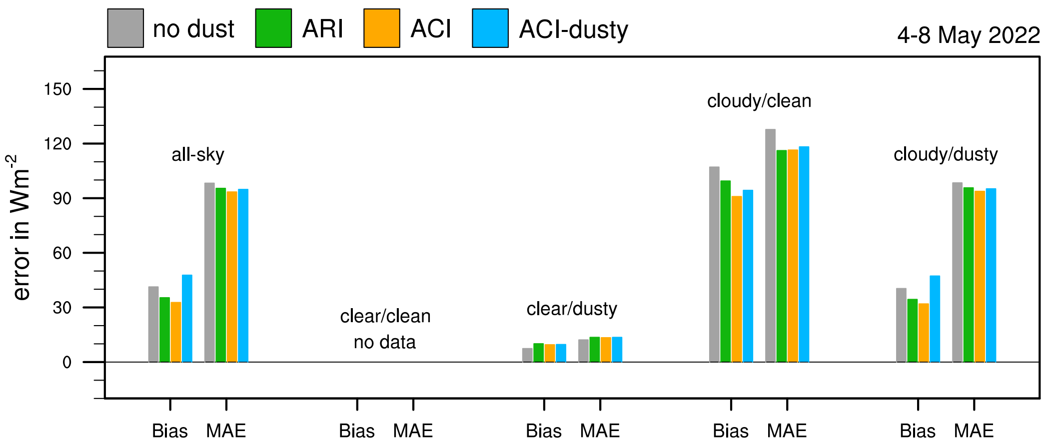

c) ICON-ART vs CERES downward shortwave radiation at the surface

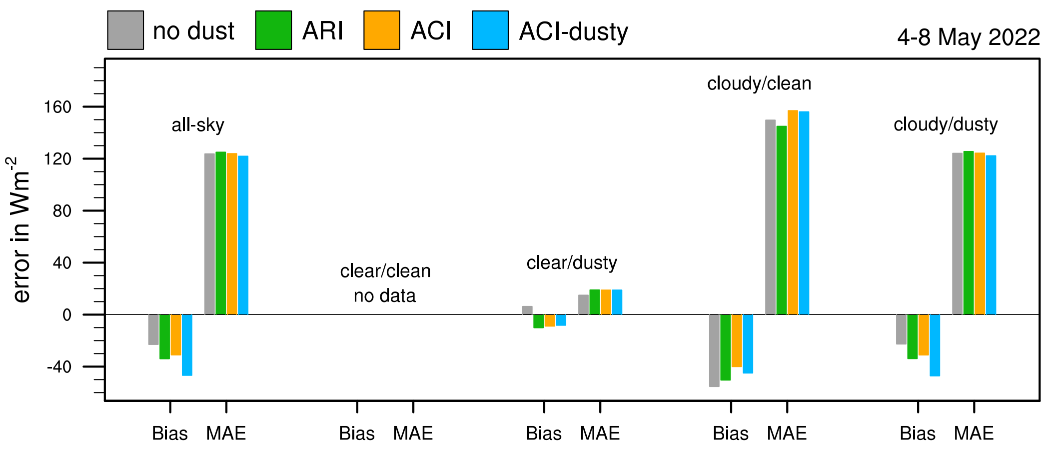

Figure S7. Bias and mean absolute error (MAE) of ICON-ART compared to CERES SSF level 2 radiative fluxes for 4-8 May 2022. Shown are the outgoing longwave radiation at the top of atmosphere (TOA), the reflected shortwave at TOA and to solar irradiance at the surface (from top to bottom)

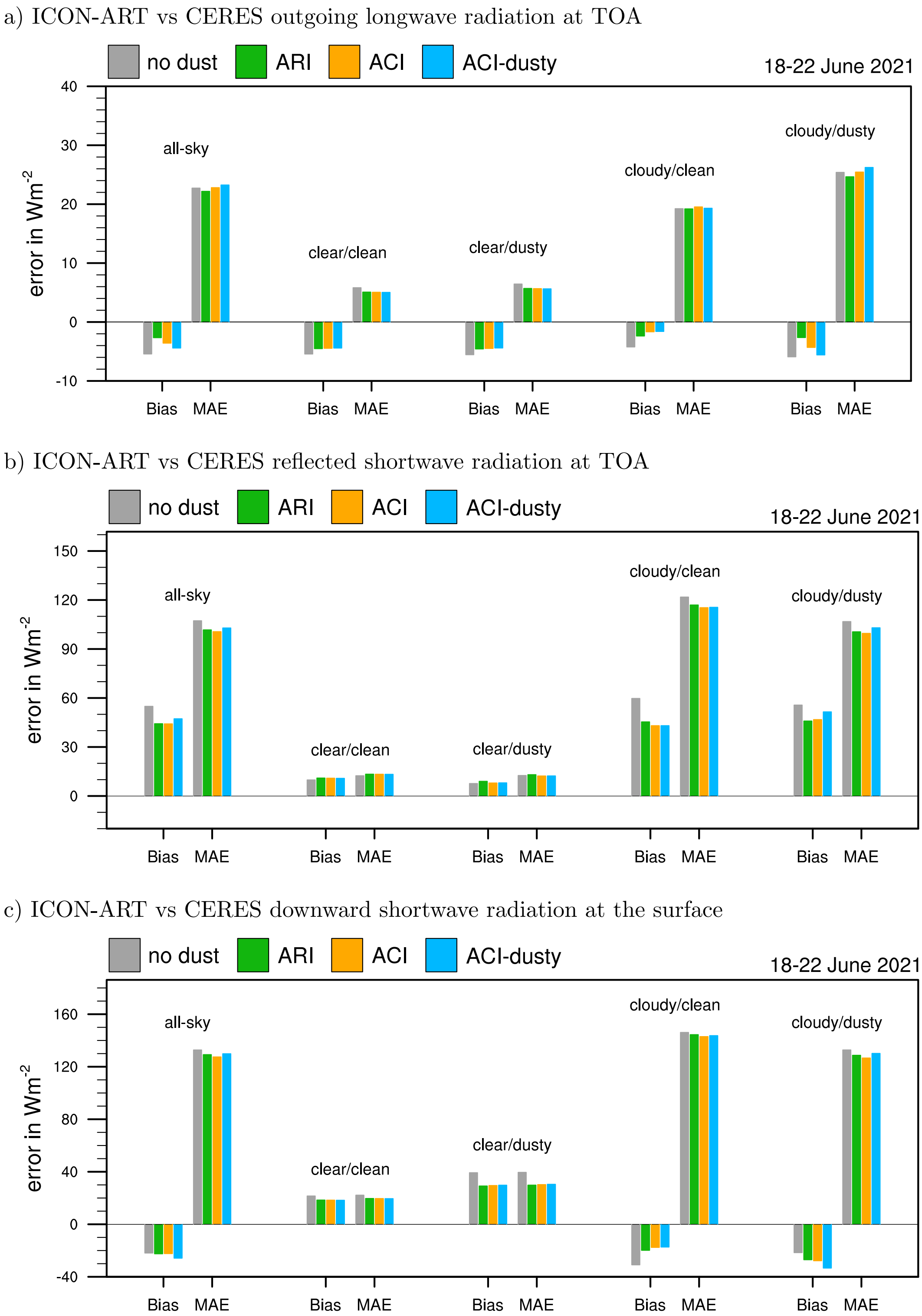

Figure S8. Bias and mean absolute error (MAE) of ICON-ART compared to CERES SSF level 2 radiative fluxes for 18-22 June 2021. Shown are the outgoing longwave radiation at the top of atmosphere (TOA), the reflected shortwave at TOA and to solar irradiance at the surface (from top to bottom)

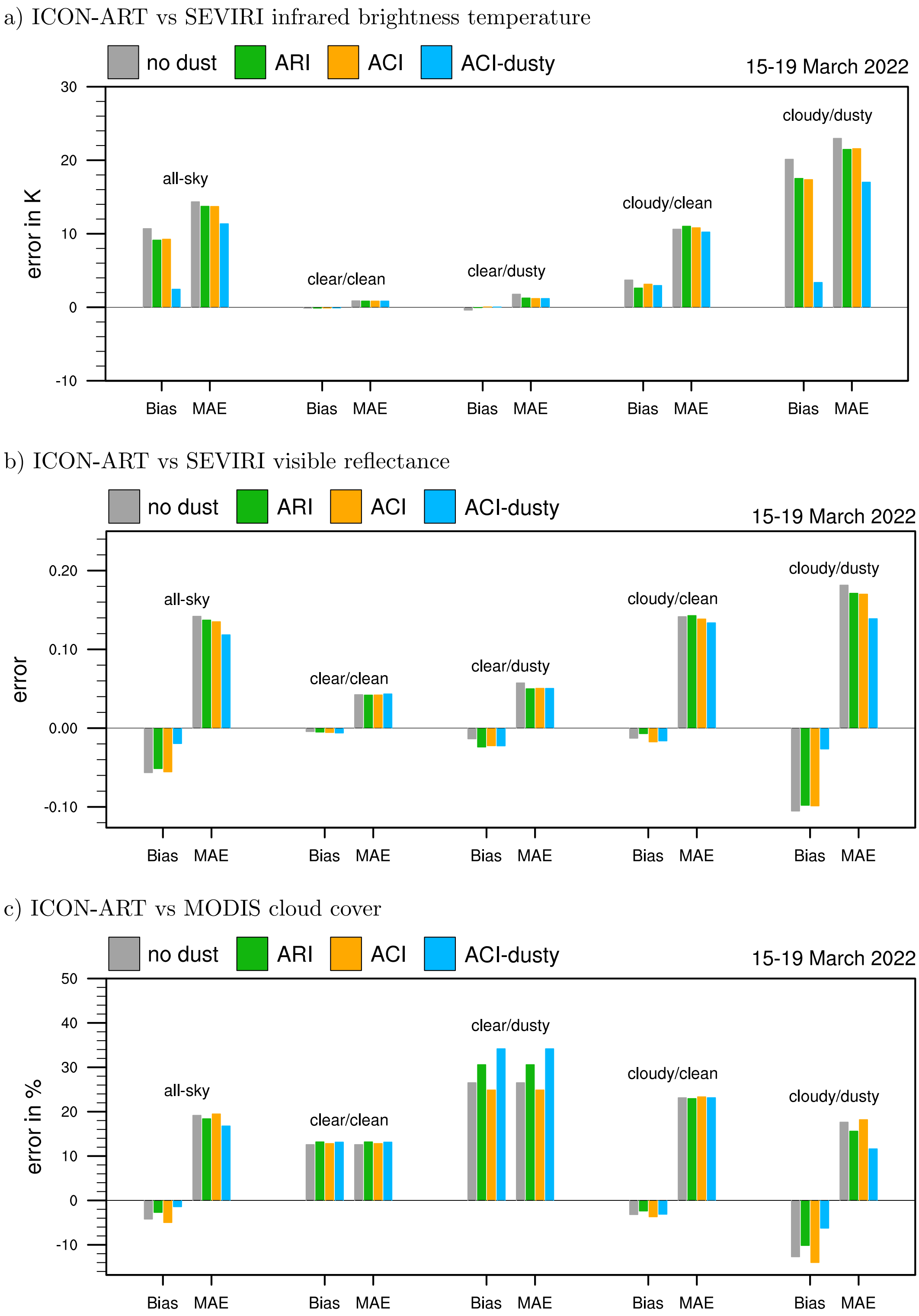

Figure S9. Bias and mean absolute error (MAE) of ICON-ART compared to SEVIRI IR and VIS and MODIS cloud cover for 15-19 March 2022. The comparision with SEVIRI uses the symmetric cloud impact factor to classify between cloudy and clear-sky. For MODIS the clear sky vs cloudy in determined by the observations only.

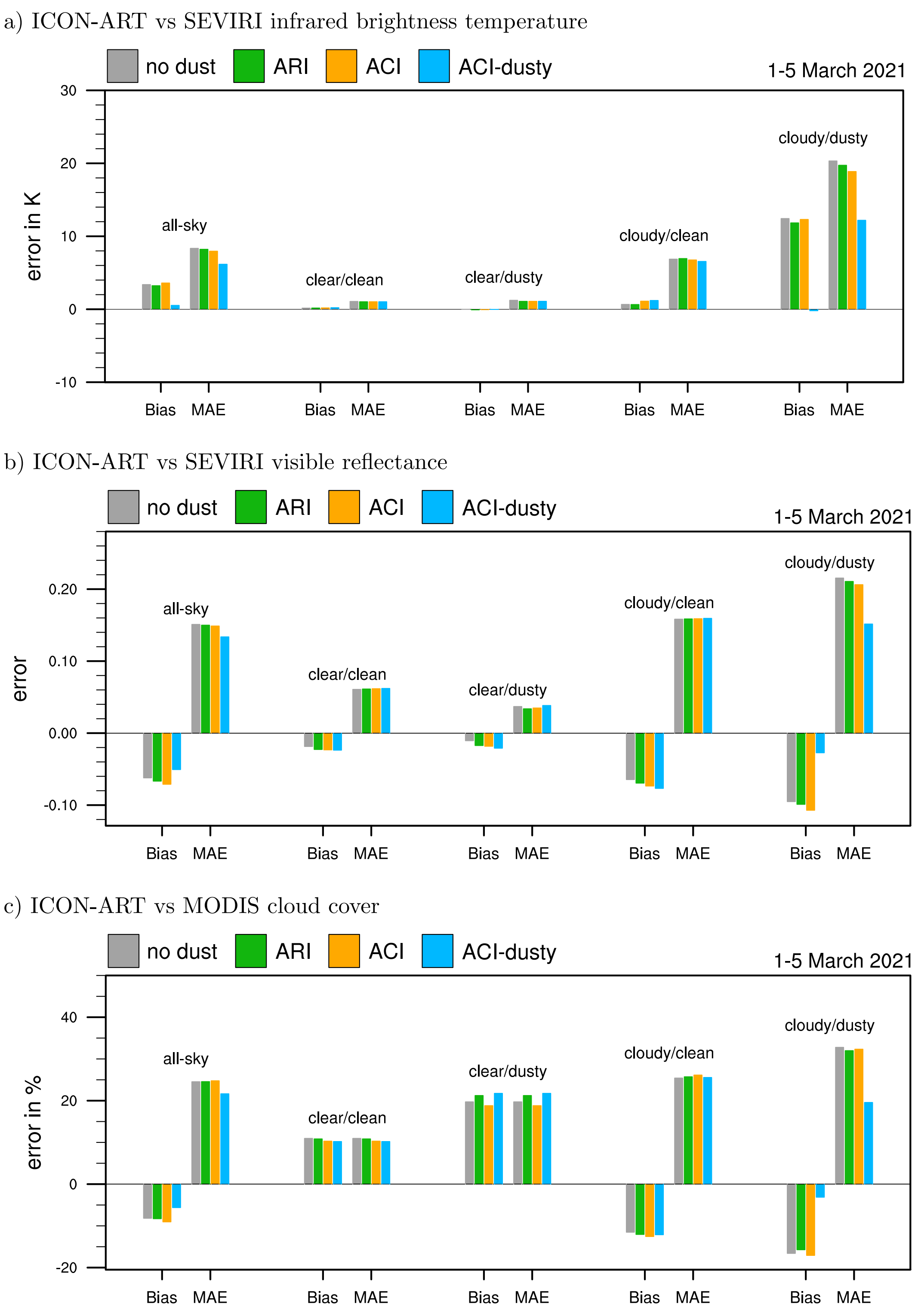

Figure S10. Bias and mean absolute error (MAE) of ICON-ART compared to SEVIRI IR and VIS and MODIS cloud cover for 1-5 March 2021. The comparision with SEVIRI uses the symmetric cloud impact factor to classify between cloudy and clear-sky. For MODIS the clear sky vs cloudy in determined by the observations only.

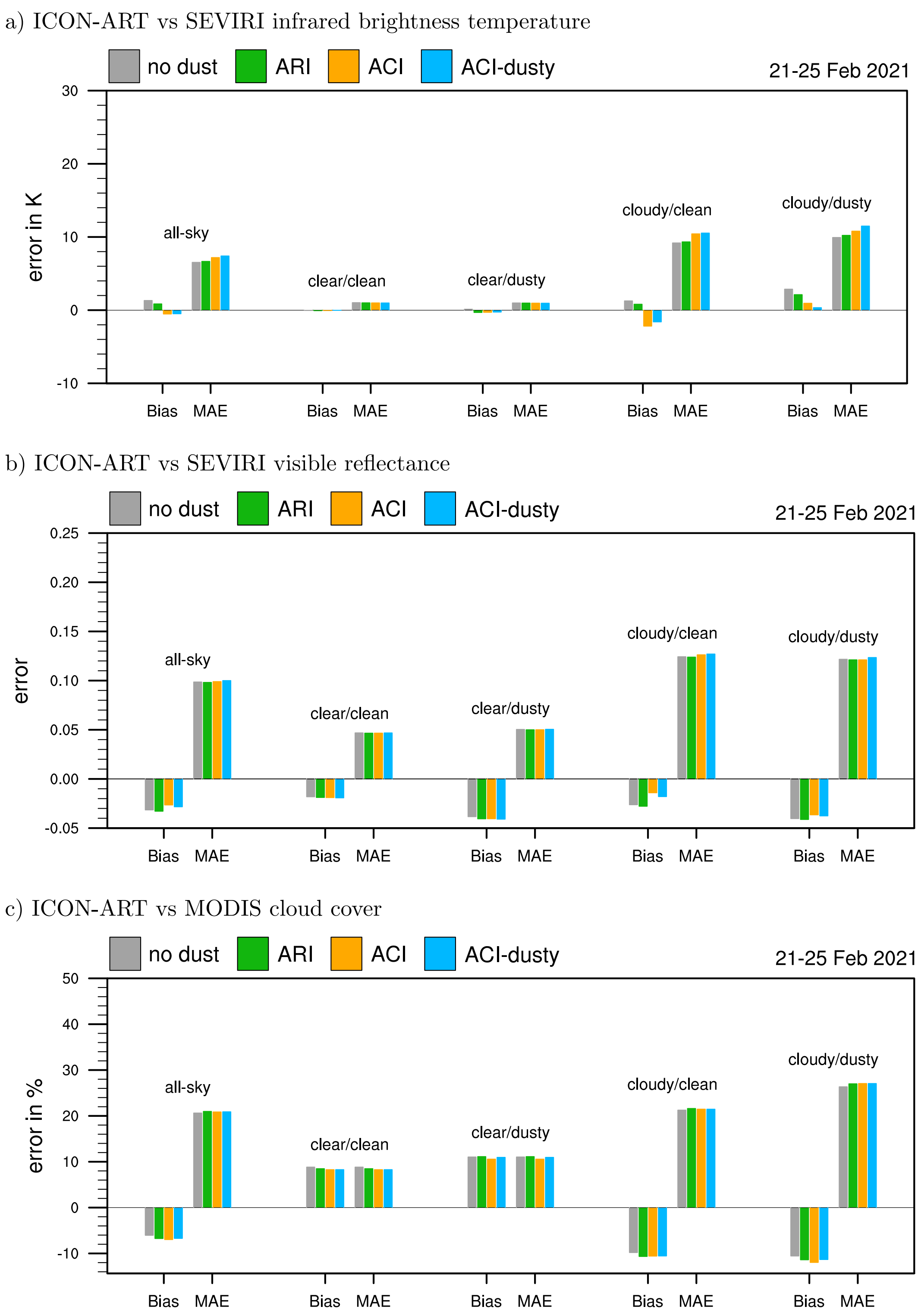

Figure S11. Bias and mean absolute error (MAE) of ICON-ART compared to SEVIRI IR and VIS and MODIS cloud cover for 21-25 Feb 2021. The comparision with SEVIRI uses the symmetric cloud impact factor to classify between cloudy and clear-sky. For MODIS the clear sky vs cloudy in determined by the observations only.

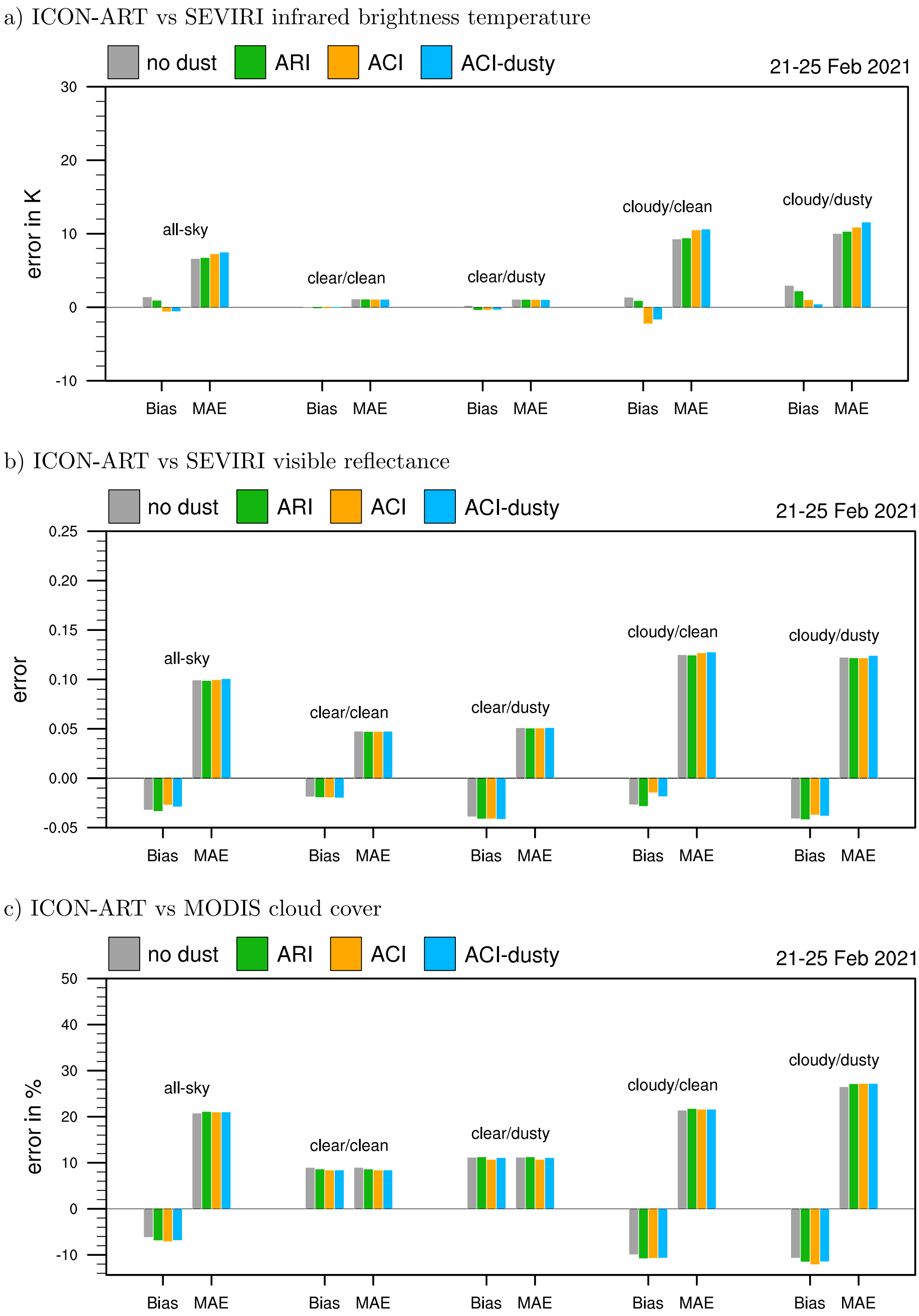

Figure S12. Bias and mean absolute error (MAE) of ICON-ART compared to SEVIRI IR and VIS and MODIS cloud cover for 27 April to 1 May 2022. The comparision with SEVIRI uses the symmetric cloud impact factor to classify between cloudy and clear-sky. For MODIS the clear sky vs cloudy in determined by the observations only.

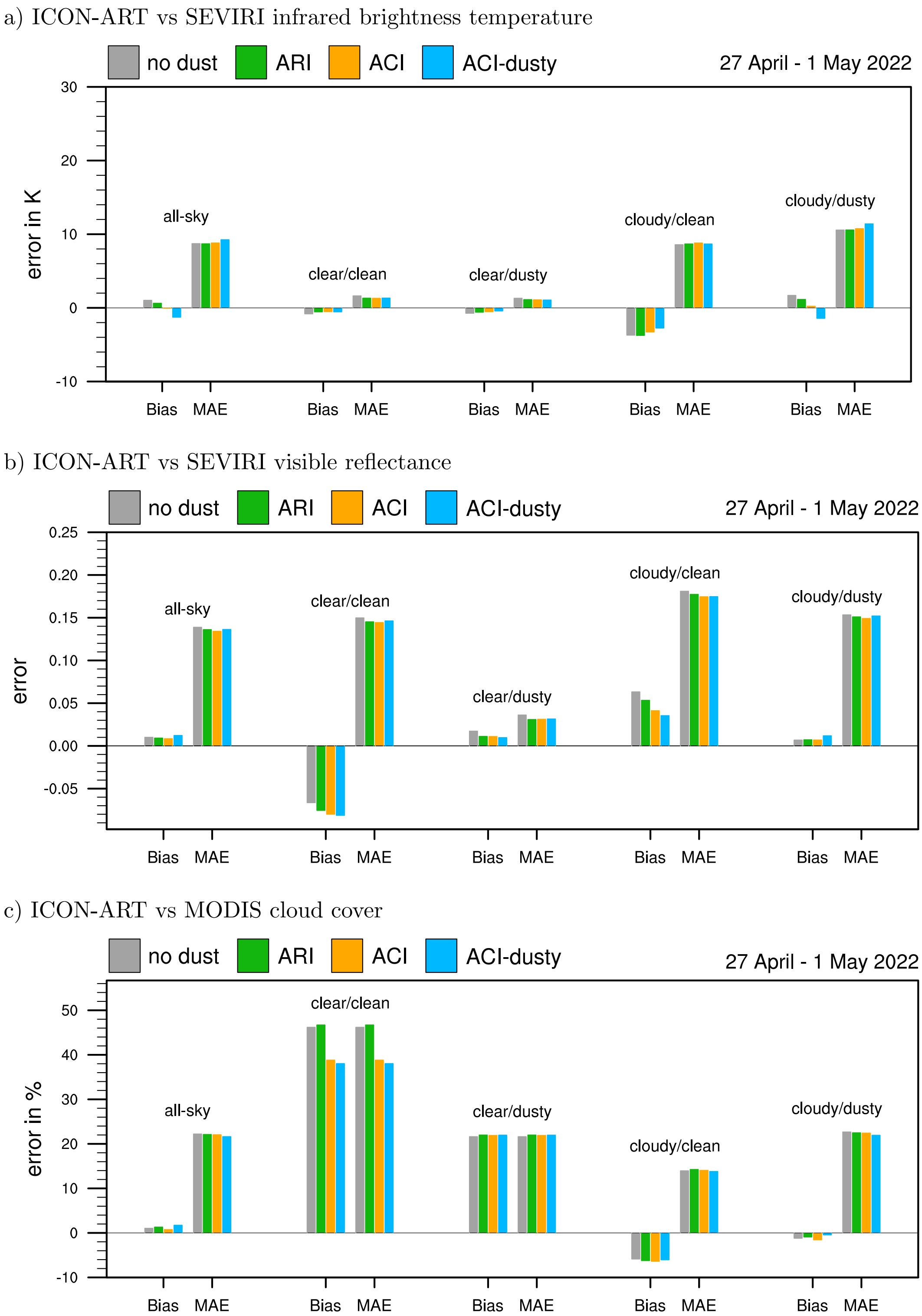

Figure S13. Bias and mean absolute error (MAE) of ICON-ART compared to SEVIRI IR and VIS and MODIS cloud cover for 18-22 June 2021. The comparision with SEVIRI uses the symmetric cloud impact factor to classify between cloudy and clear-sky. For MODIS the clear sky vs cloudy in determined by the observations only.

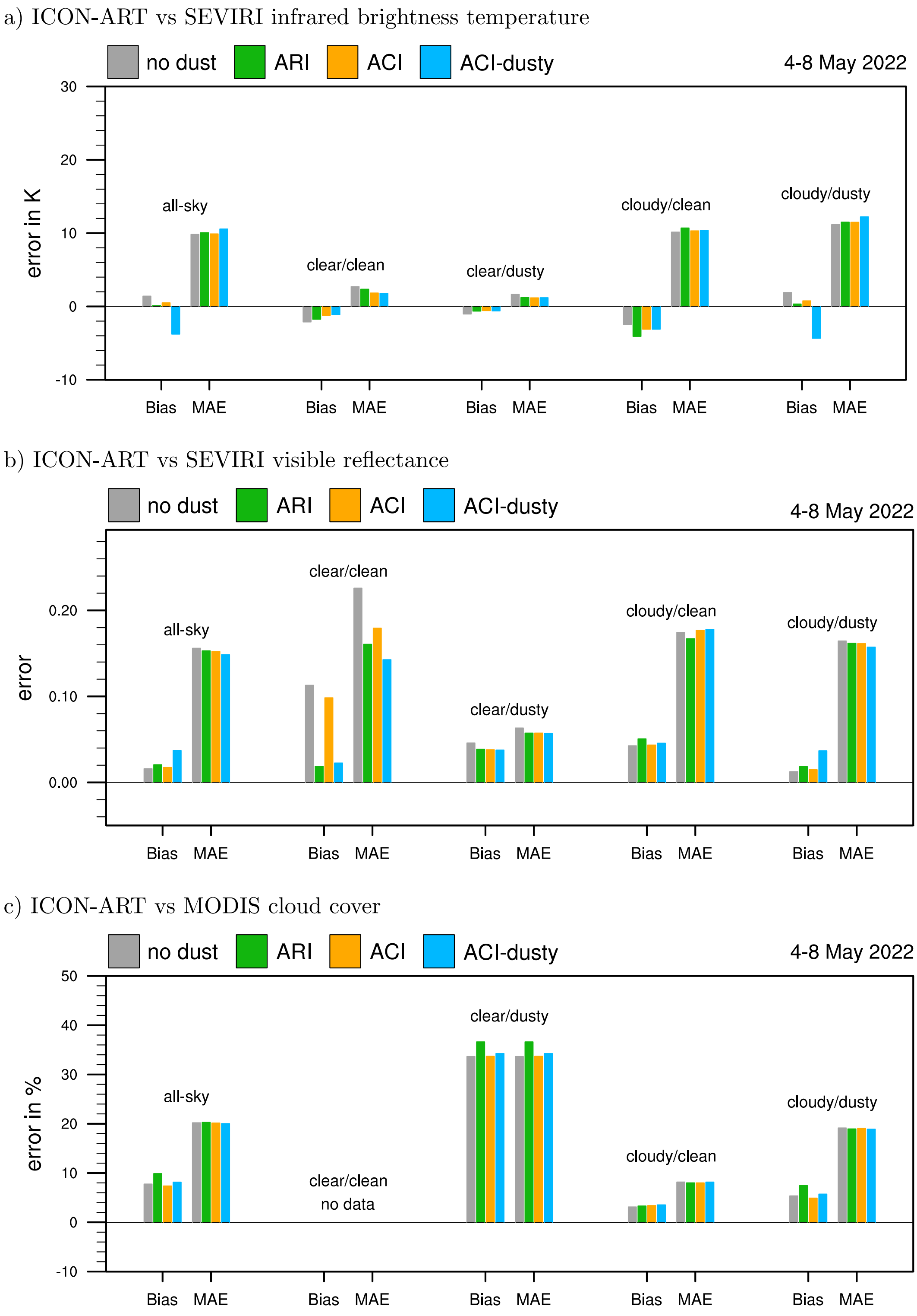

Figure S14. Bias and mean absolute error (MAE) of ICON-ART compared to SEVIRI IR and VIS and MODIS cloud cover for 21-25 Feb 2021. The comparision with SEVIRI uses the symmetric cloud impact factor to classify between cloudy and clear-sky. For MODIS the clear sky vs cloudy in determined by the observations only.

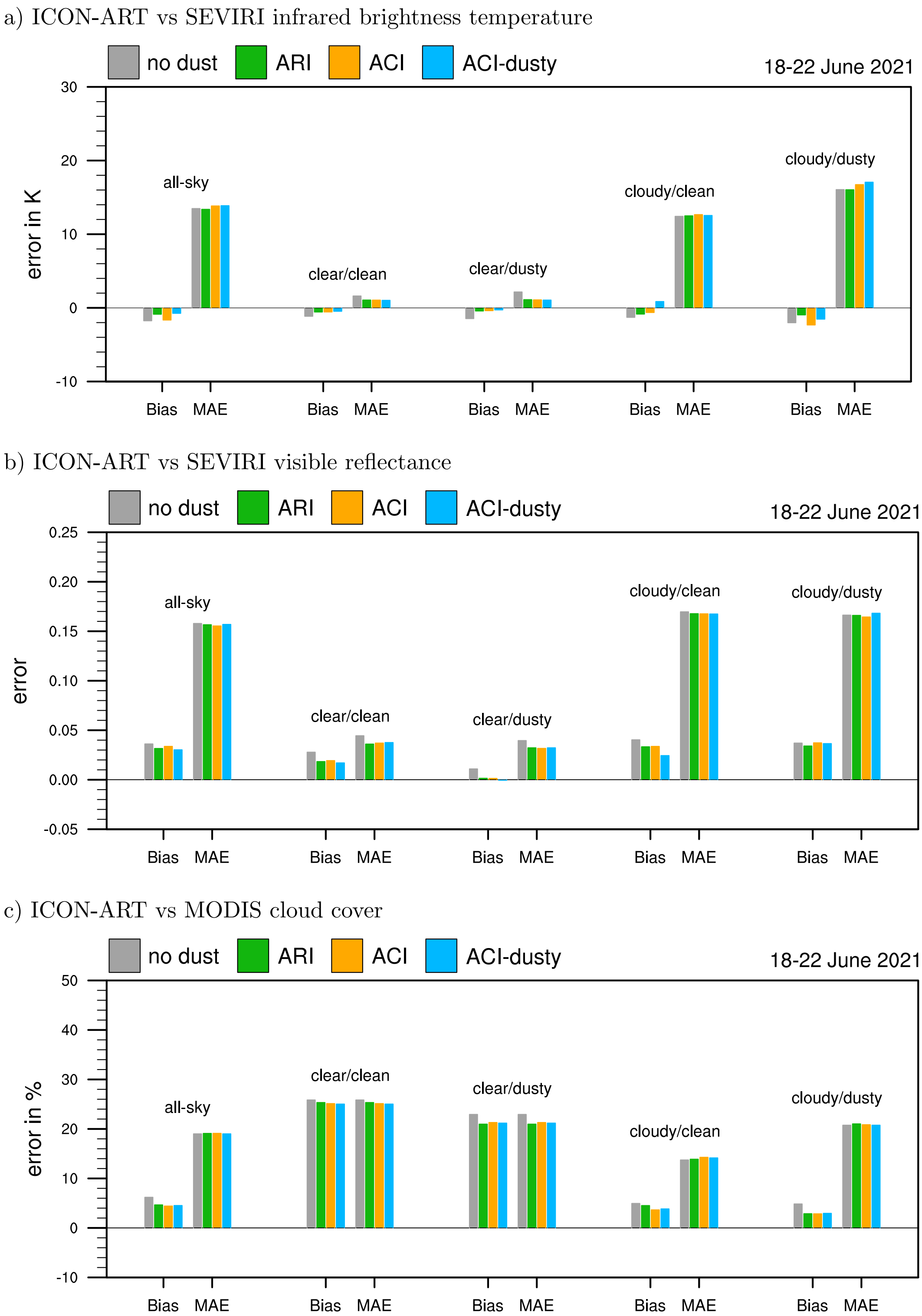

Figure S15. Bias and mean absolute error (MAE) of ICON-ART compared to SEVIRI IR and VIS and MODIS cloud cover for all Saharan dust episodes. The comparision with SEVIRI uses the symmetric cloud impact factor to classify between cloudy and clear-sky. For MODIS the clear sky vs cloudy in determined by the observations only.

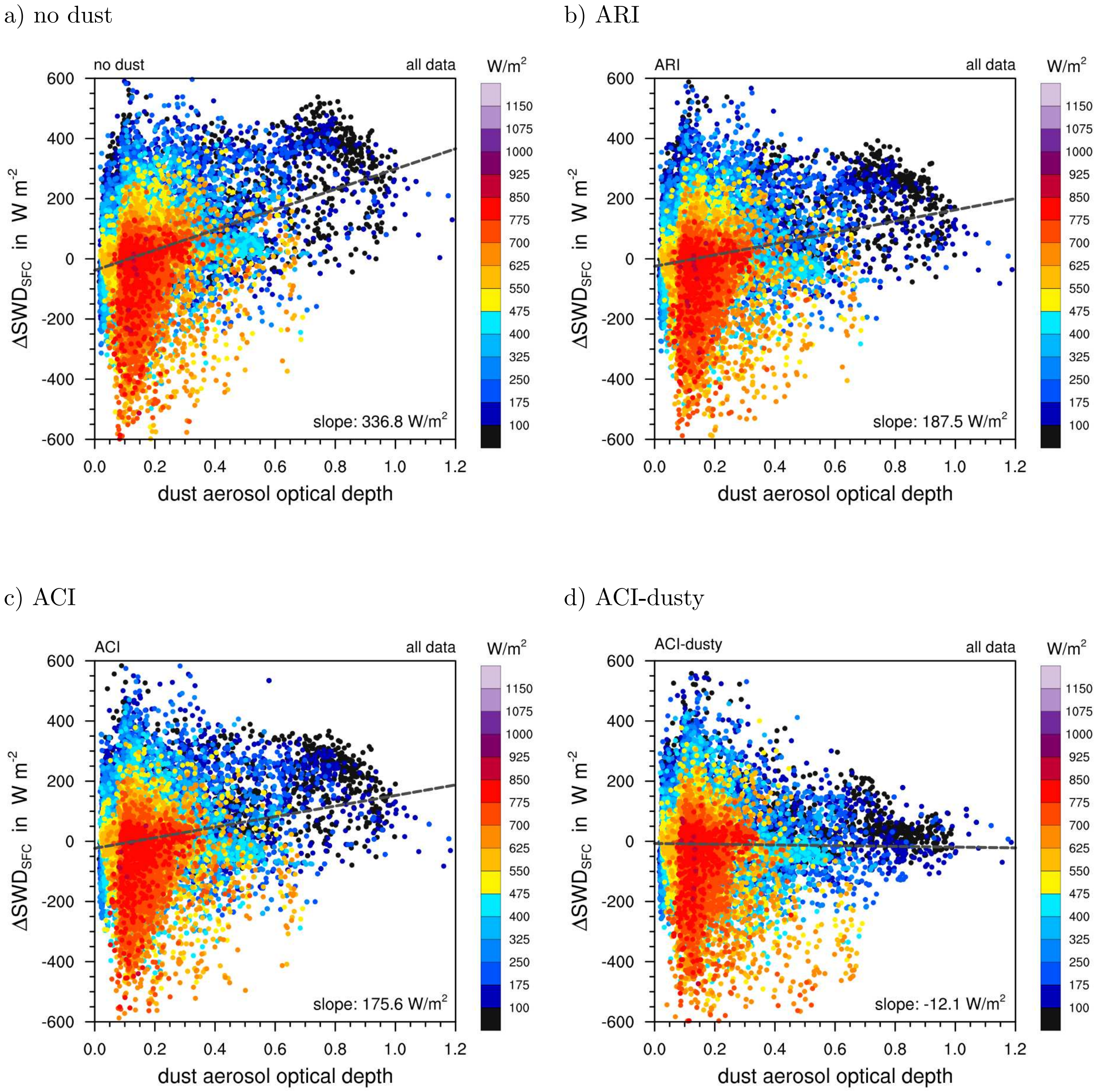

Figure S16. Scatter plots of errors in solar irradiance at the surface as function of mineral dust AOD predicted by ICON-ART. Shown is (model-obs) for individual CERES footprints with a diameter of 25 km.

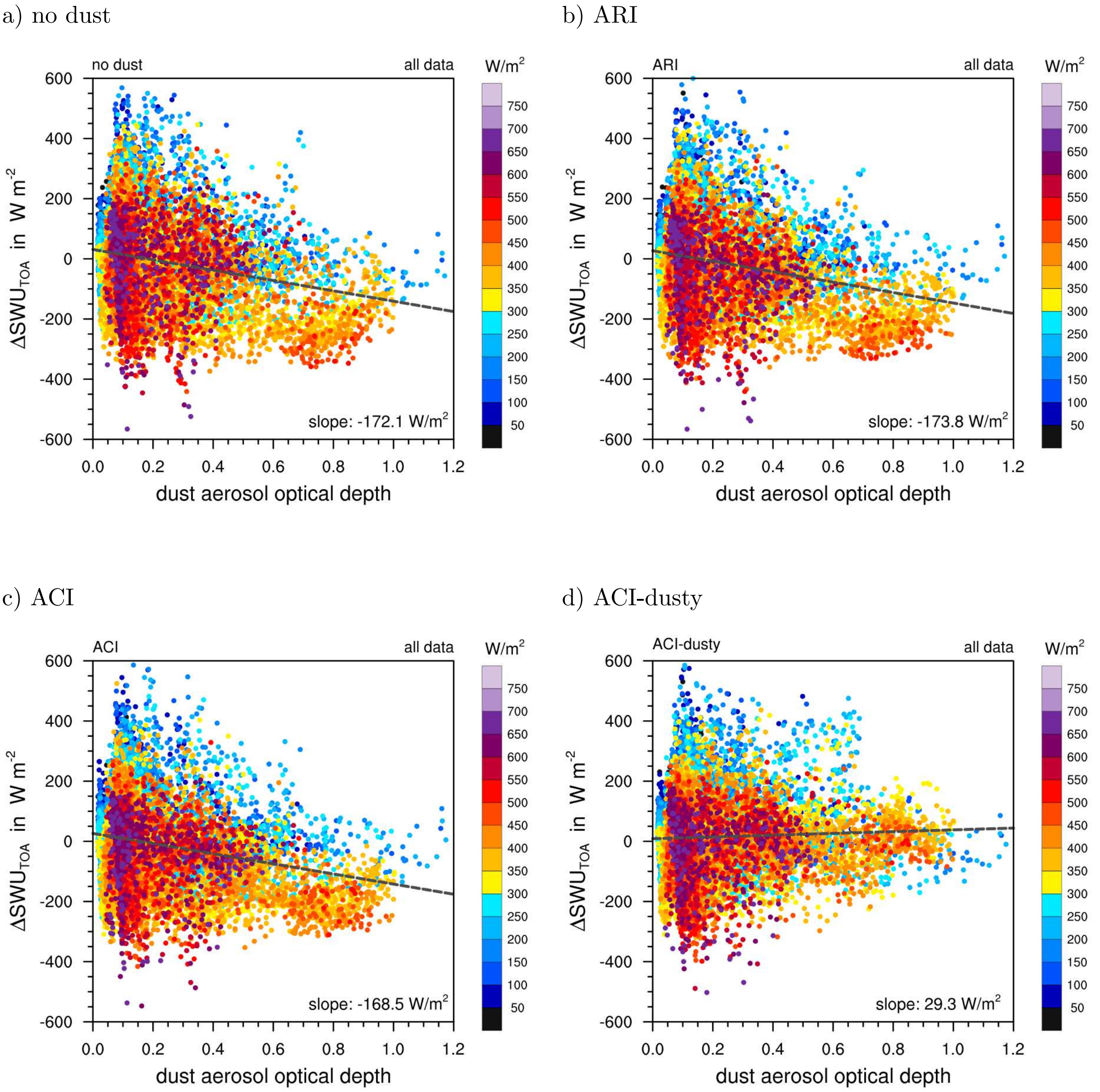

Figure S17. Scatter plots of errors in reflected shortwave radiation at top of atmosphers as function of mineral dust AOD predicted by ICON-ART. Shown is (model-obs) for individual CERES footprints with a diameter of 25 km.

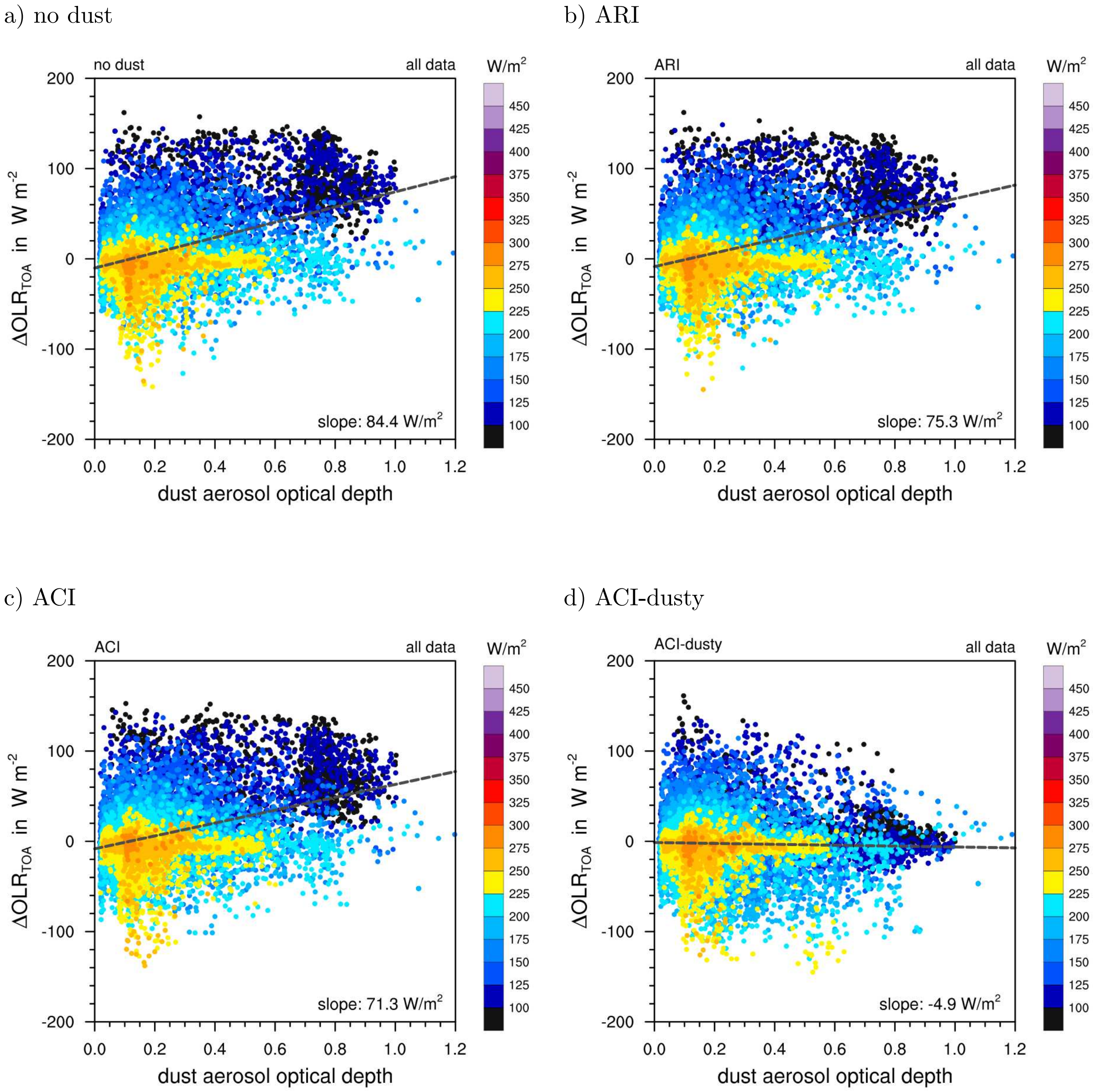

Figure S18. Scatter plots of errors in outgoing longwave radiation at top of atmosphers as function of mineral dust AOD predicted by ICON-ART. Shown is (model-obs) for individual CERES footprints with a diameter of 25 km.

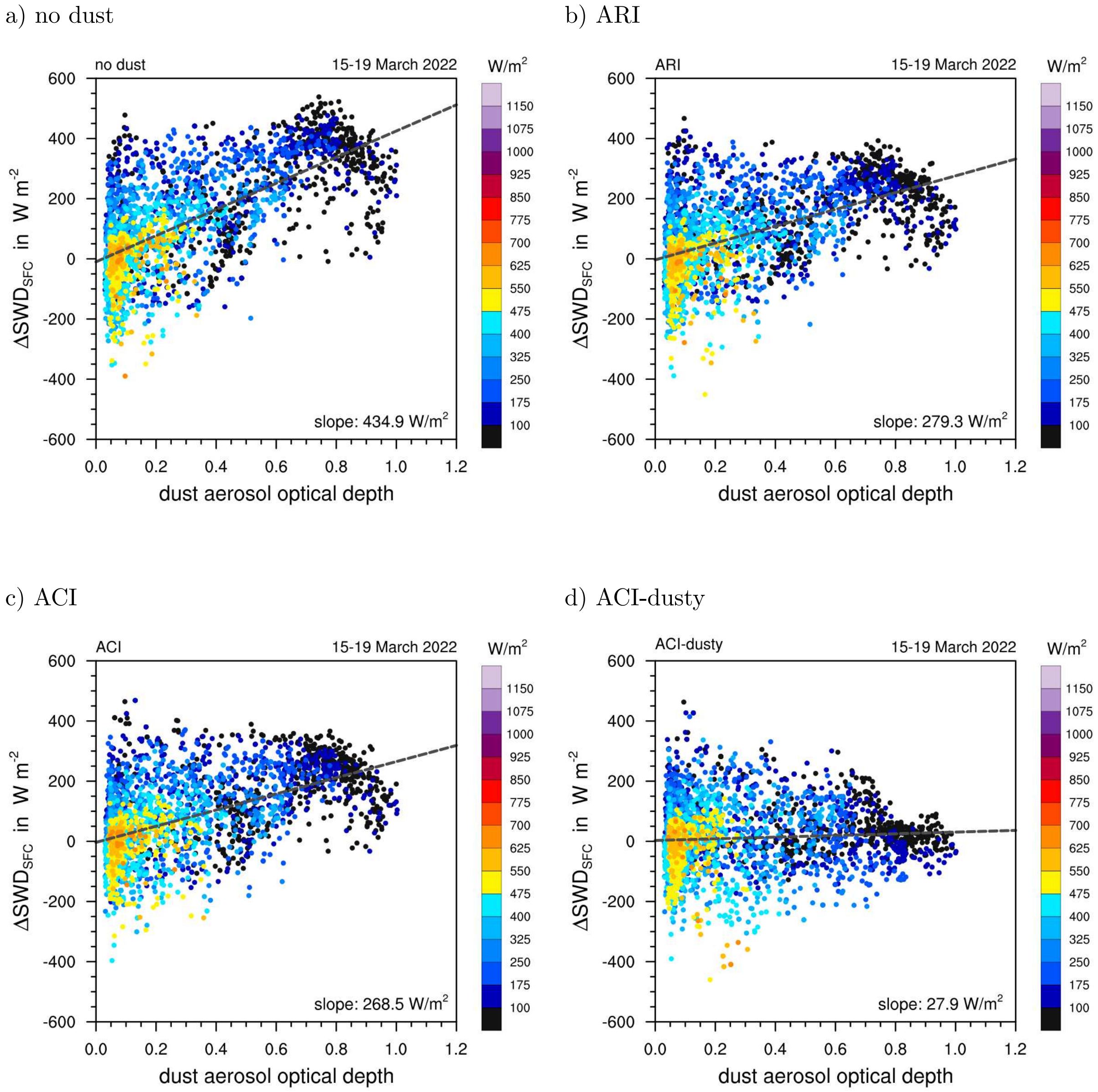

Figure S19. Scatter plots of errors in solar irradiance at the surface as function of mineral dust AOD predicted by ICON-ART for 15-18 March 2022. Shown is (model-obs) for individual CERES footprints with a diameter of 25 km.

a) no dust b) ARI c) ACI d) ACI-dusty

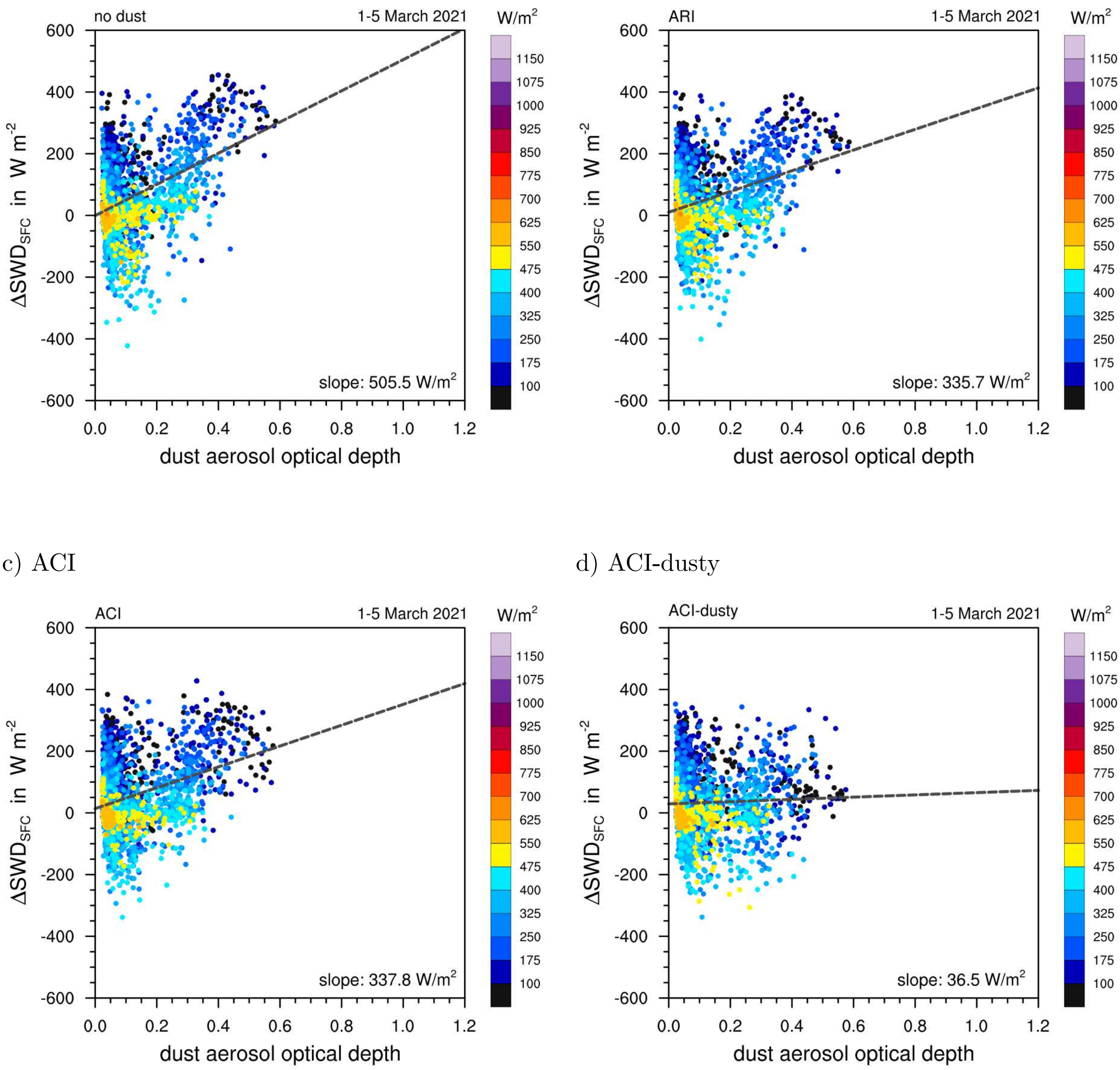

Figure S20. Scatter plots of errors in solar irradiance at the surface as function of mineral dust AOD predicted by ICON-ART for 1-5 March 2021. Shown is (model-obs) for individual CERES footprints with a diameter of 25 km.

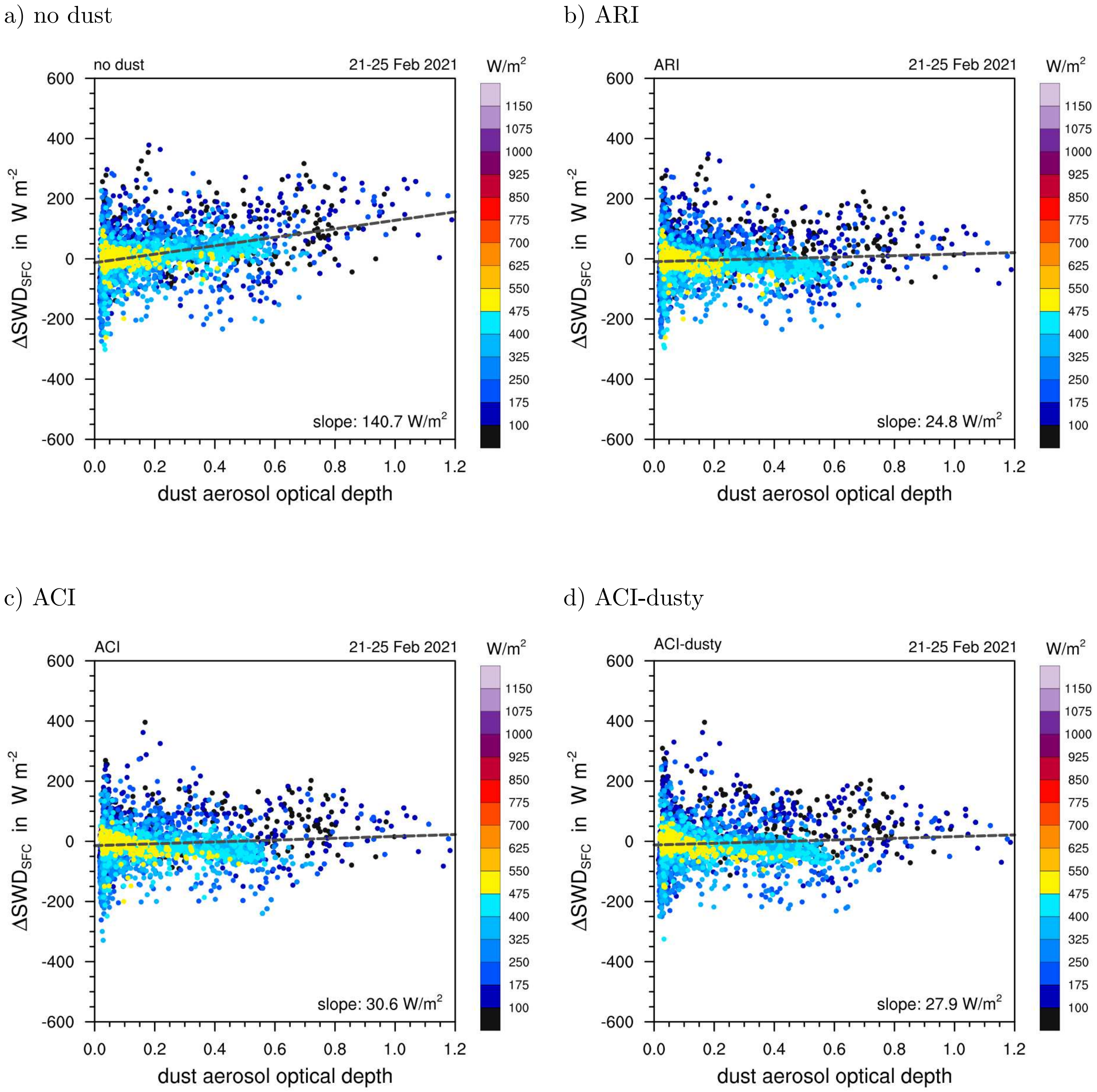

Figure S21. Scatter plots of errors in solar irradiance at the surface as function of mineral dust AOD predicted by ICON-ART for 21-25 Feb 2021. Shown is (model-obs) for individual CERES footprints with a diameter of 25 km.

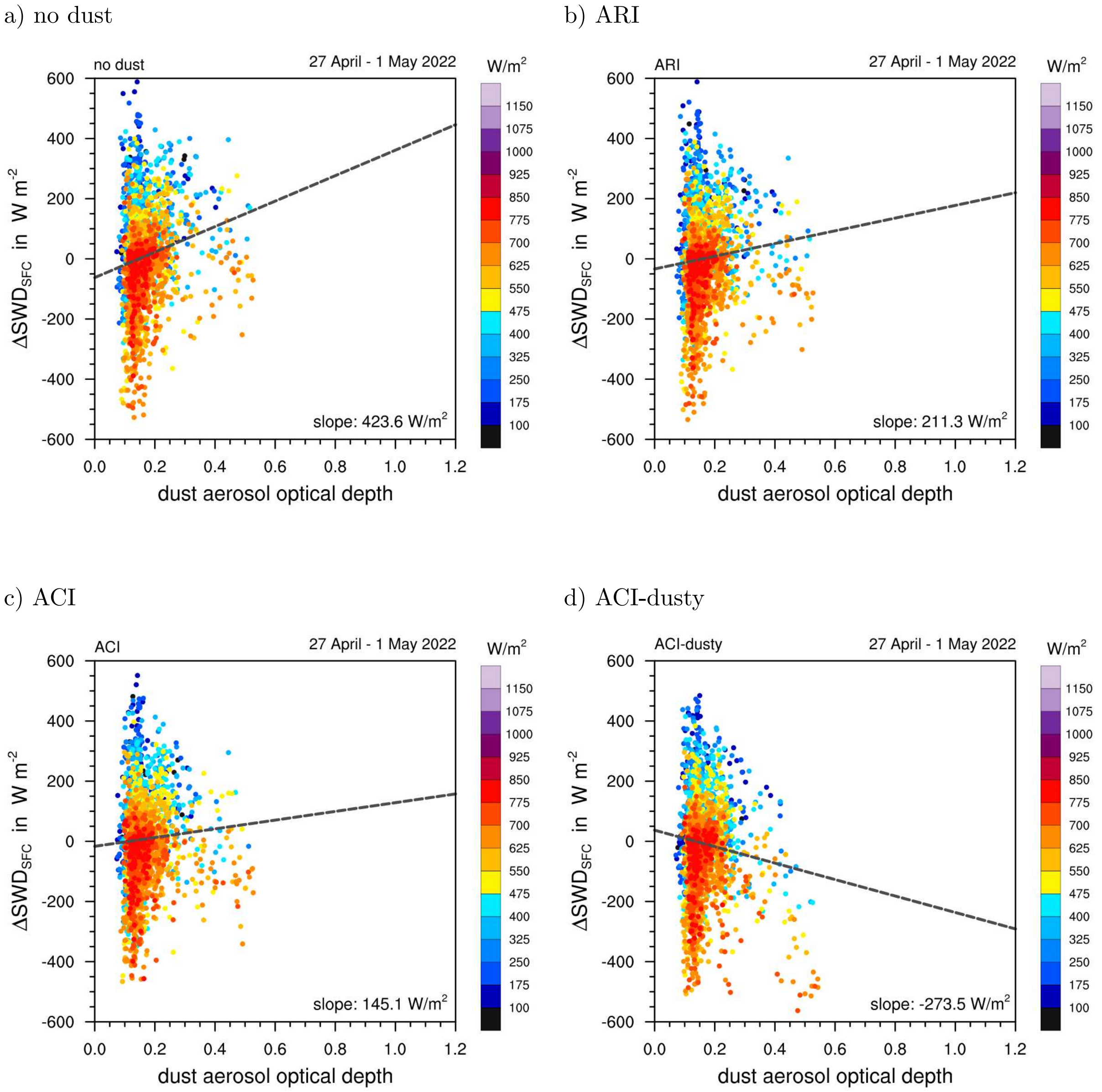

Figure S22. Scatter plots of errors in solar irradiance at the surface as function of mineral dust AOD predicted by ICON-ART for 27-31 Apr 2022. Shown is (model-obs) for individual CERES footprints with a diameter of 25 km.

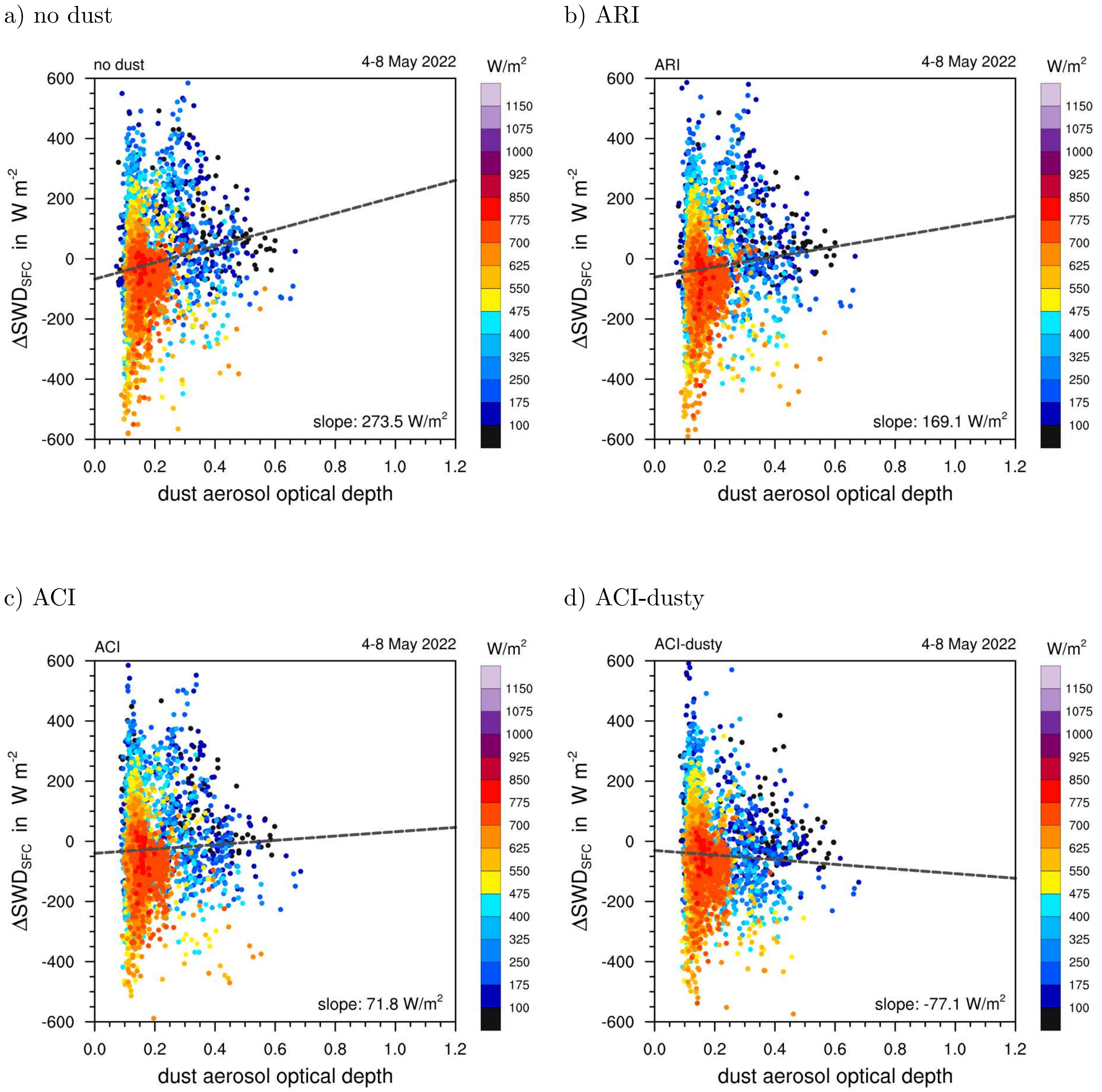

Figure S23. Scatter plots of errors in solar irradiance at the surface as function of mineral dust AOD predicted by ICON-ART for 18-22 June 2021. Shown is (model-obs) for individual CERES footprints with a diameter of 25 km.

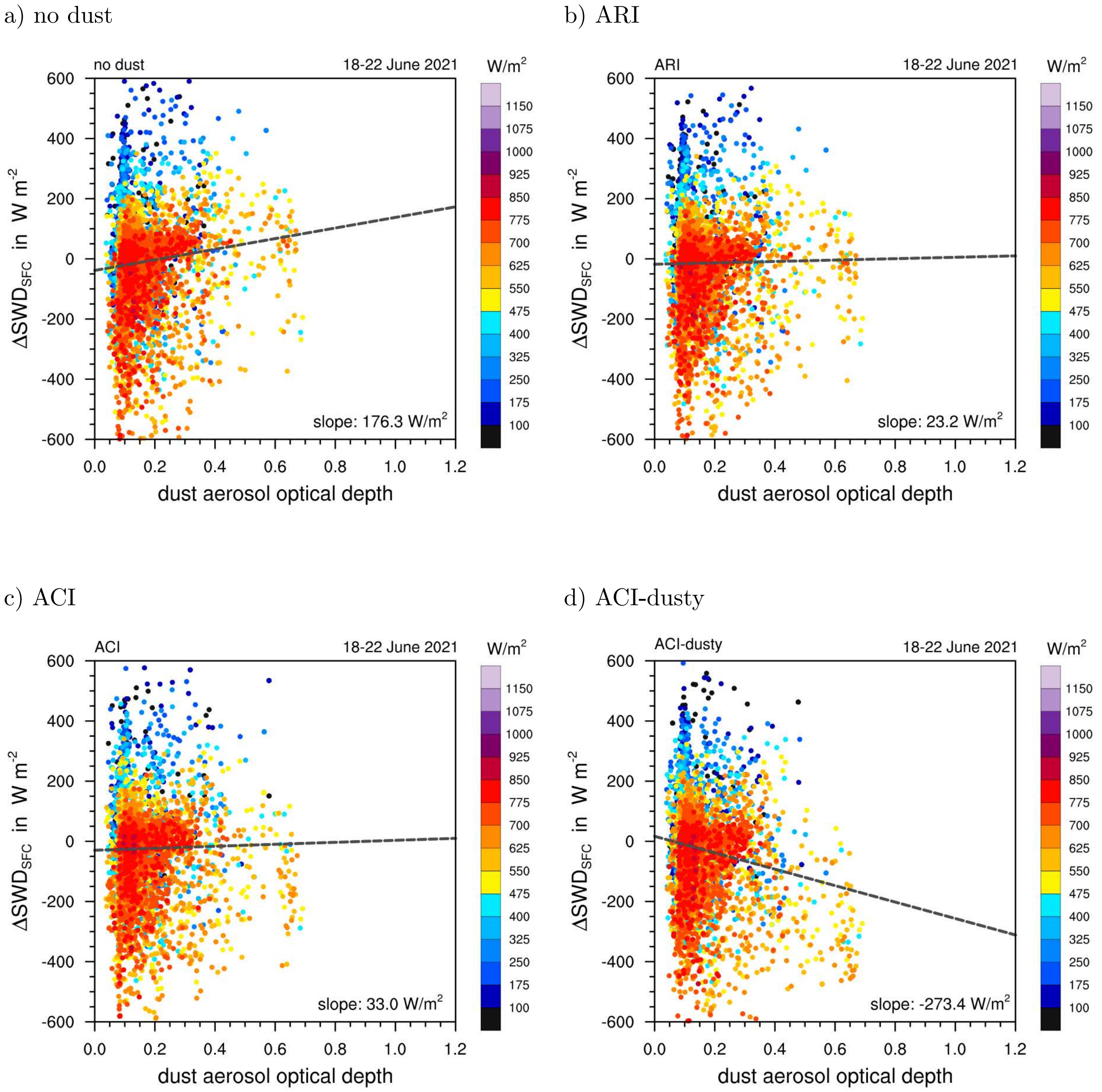

Figure S24. Scatter plots of errors in solar irradiance at the surface as function of mineral dust AOD predicted by ICON-ART for 18-22 June 2021. Shown is (model-obs) for individual CERES footprints with a diameter of 25 km.

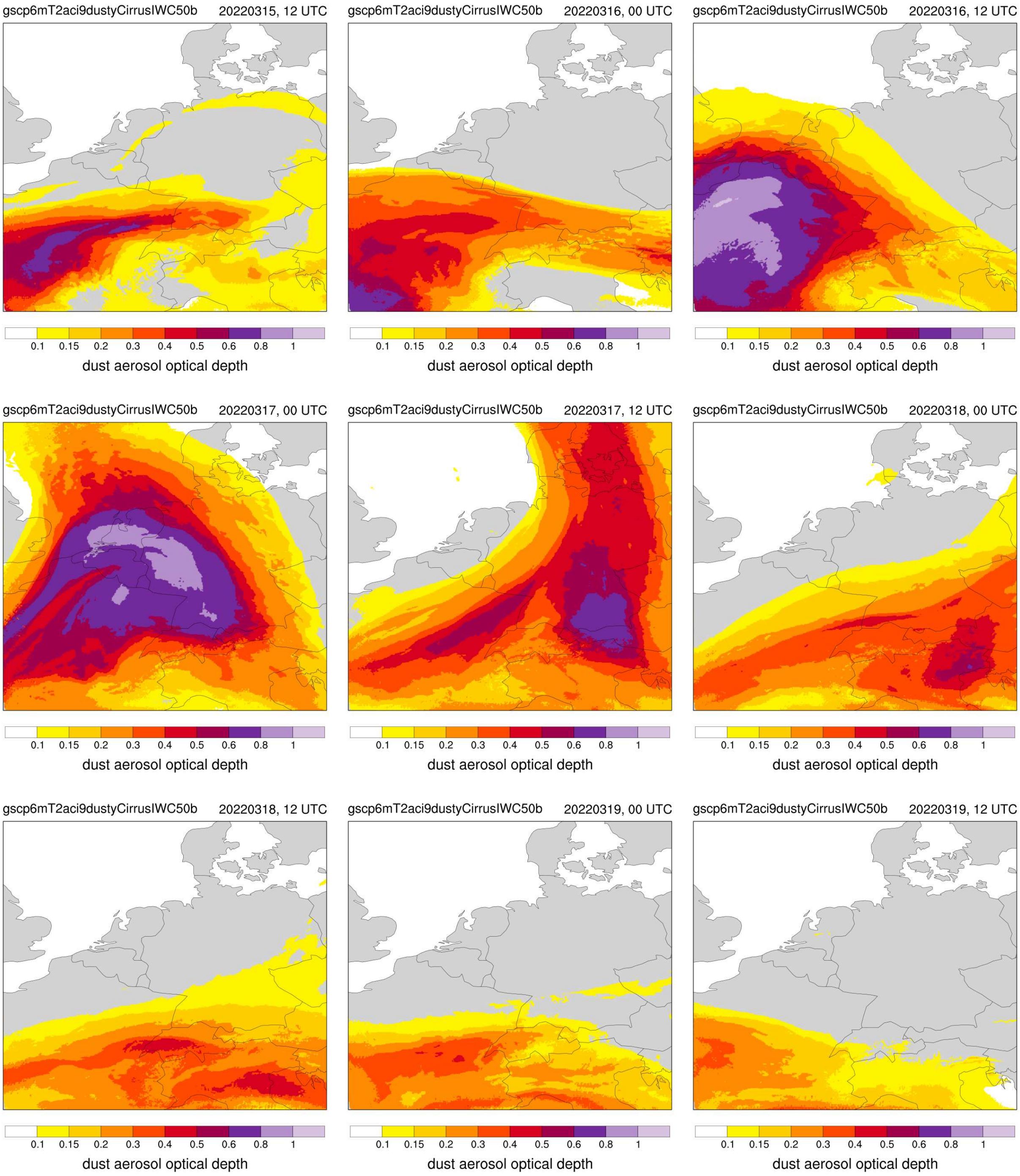

Figure S25. ICON-ART mineral dust AOD for 15-19 March 2022.

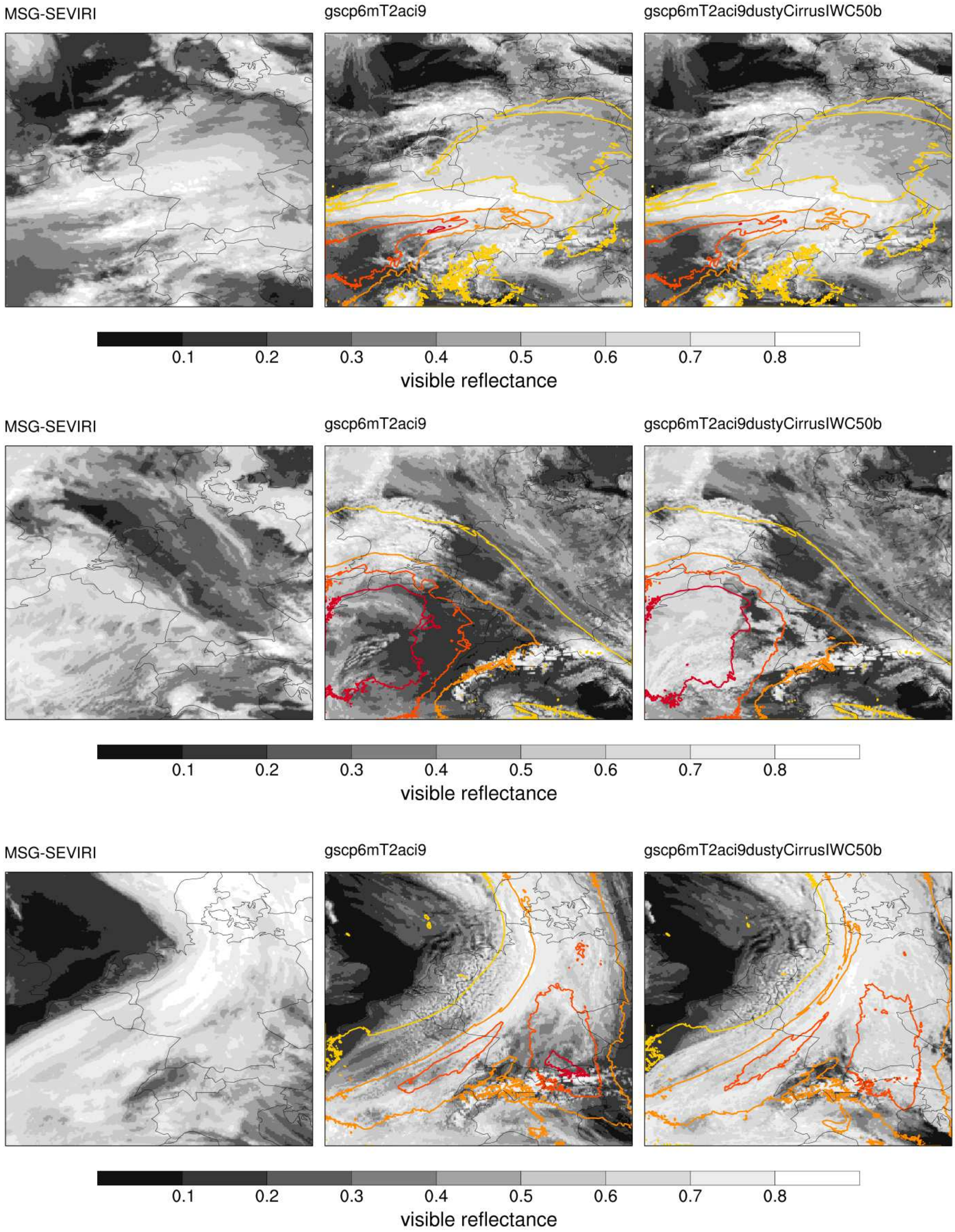

Figure S26. MSG SEVIRI visible reflectance vs ICON-ART for or 15 March 2022 12 UTC, 16 March 12 UTC and 17 March 12 UTC (top to bottom). For ICON-ART the mineral dust AOD is shown with isolines from 0.1 to 0.7 (yellow-orange-red) with intervals of 0.2.

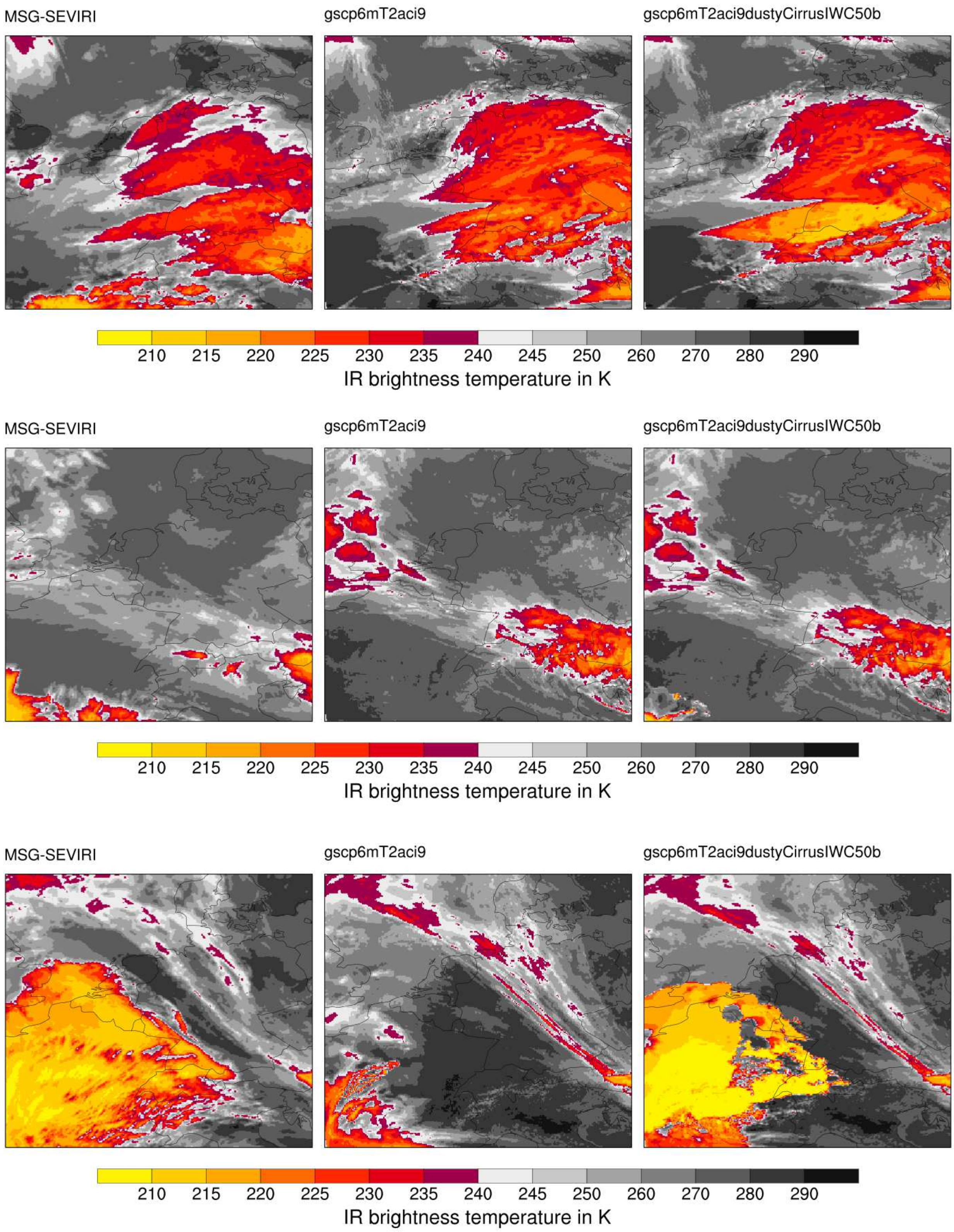

Figure S27. MSG SEVIRI infrared at 10.8 μm vs ICON-ART for 15 March 2022 12 UTC, 16 March 00 UTC and 16 March 12 UTC (top to bottom).

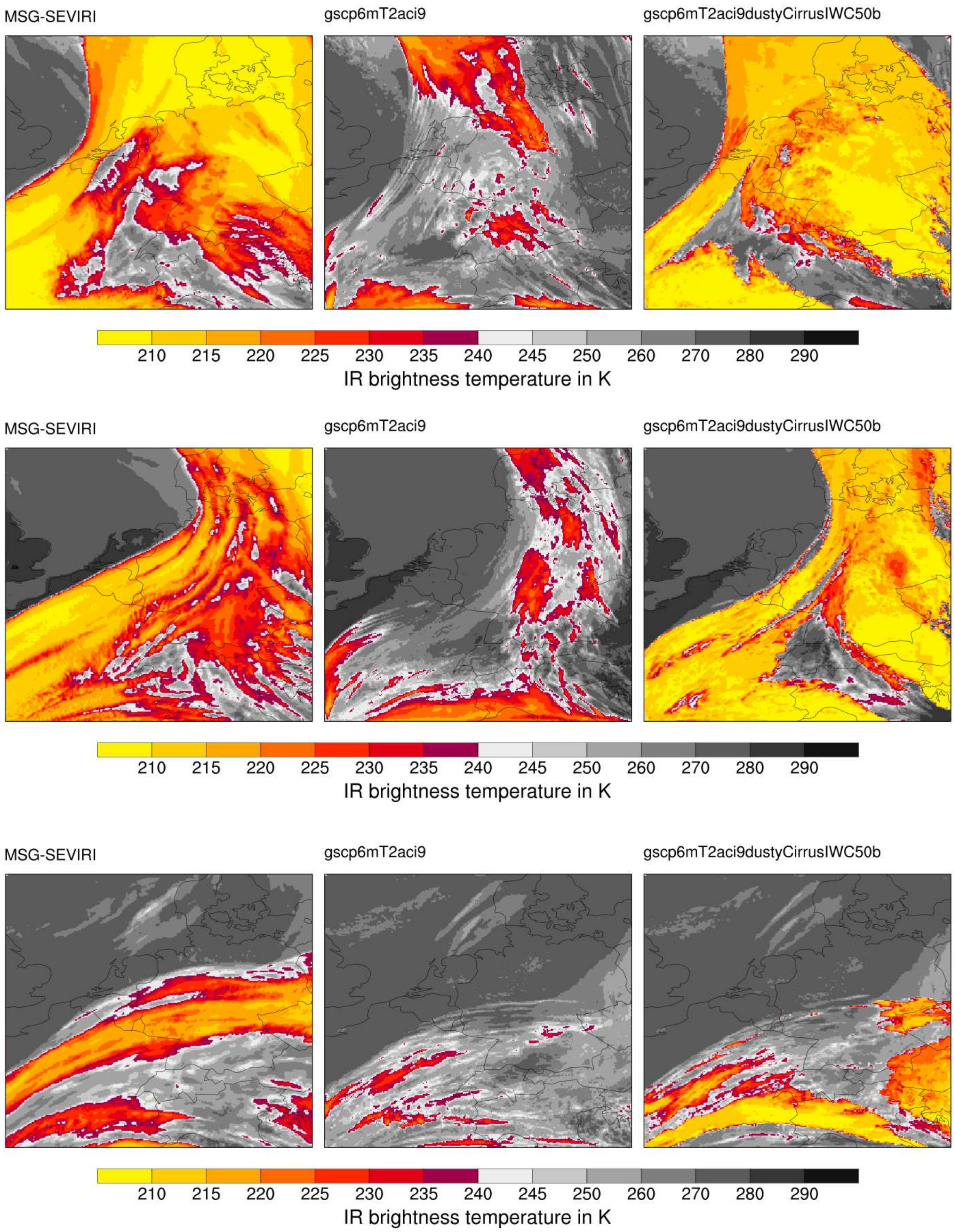

Figure S28. MSG SEVIRI infrared at 10.8 μm vs ICON-ART for 17 March 2022 05 UTC, 17 March 12 UTC and 18 March 00 UTC (top to bottom).

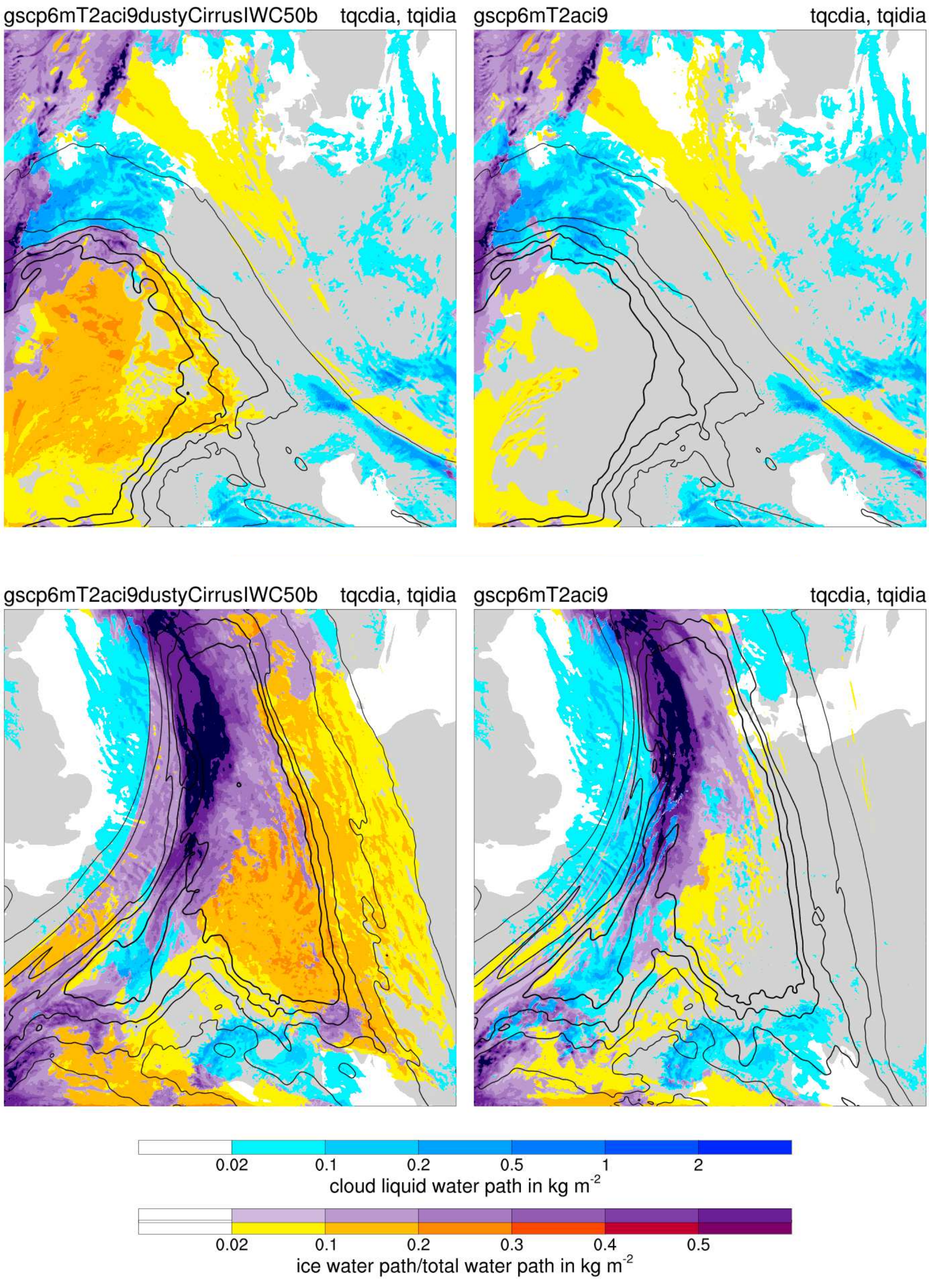

Figure S29. Cloud ice water path (orange-red), cloud water path (blue), and total cloud water path (magenta) for 16 March 2022 12 UTC and 17 March 2022 06 UTC. IWP is shown for column with only ice, LWP for columuns with liquid only, and TWP for column with mixed-phase or multi-layer clouds that contain ice and liquid. The IWP and TWP do include the sub-grid diagnostic contribution, e.g., from the dusty cirrus parameterization. Shown are the ACI (right) and the ACI-dusty (left) simulations of ICON-ART. Isolines are the mineral dust AOD from 0.1 to 0.5 with intervals of 0.1.

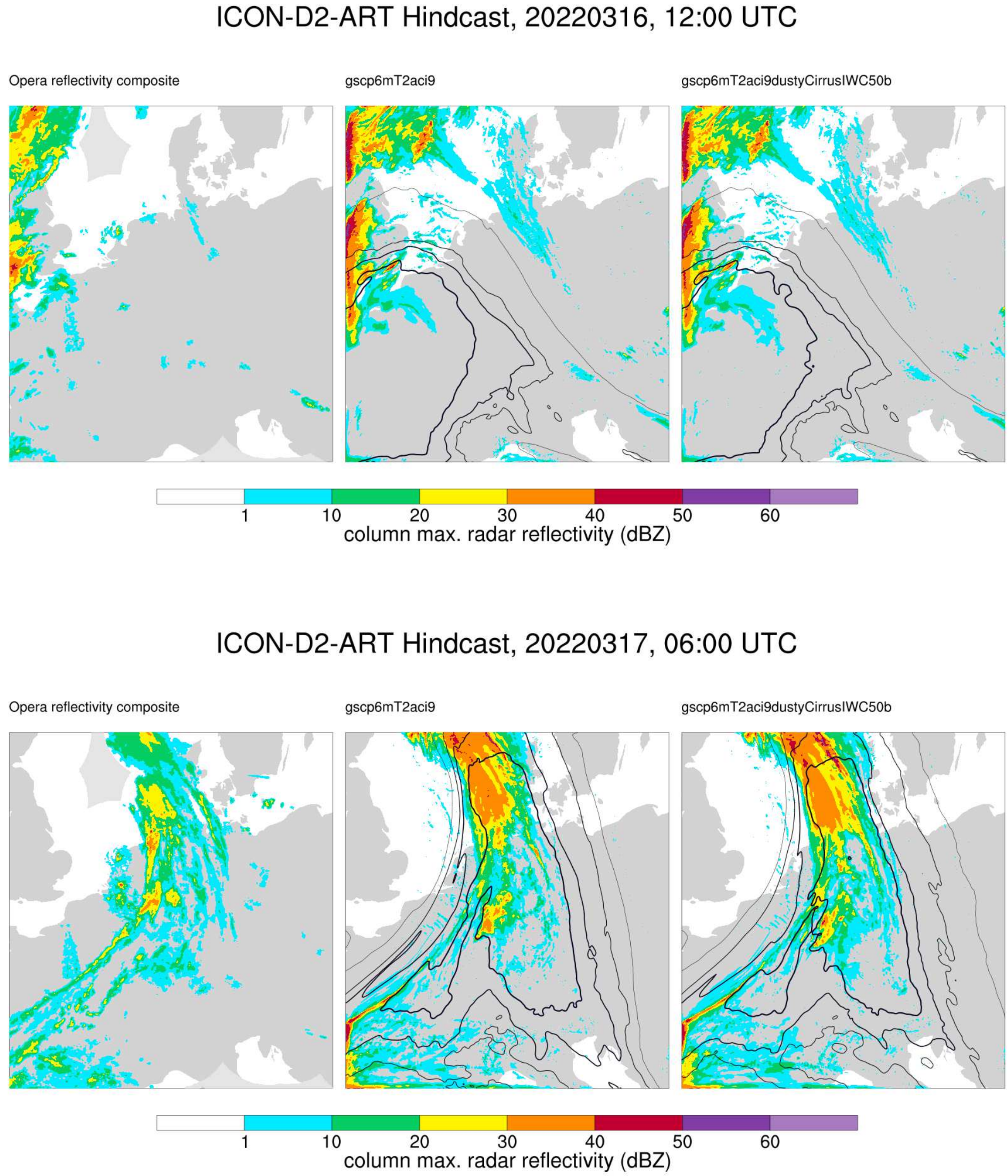

Figure S30. Column-maximum radar reflectivity factor in dBZ for 16 March 2022 12 UTC and 17 March 2022 06 UTC. Shown is the Opera composit (left), the ACI simulation (center), and the ACI-dusty simulation (right). Isolines are the mineral dust AOD at 0.1, 0.2, 0.3 and 0.5

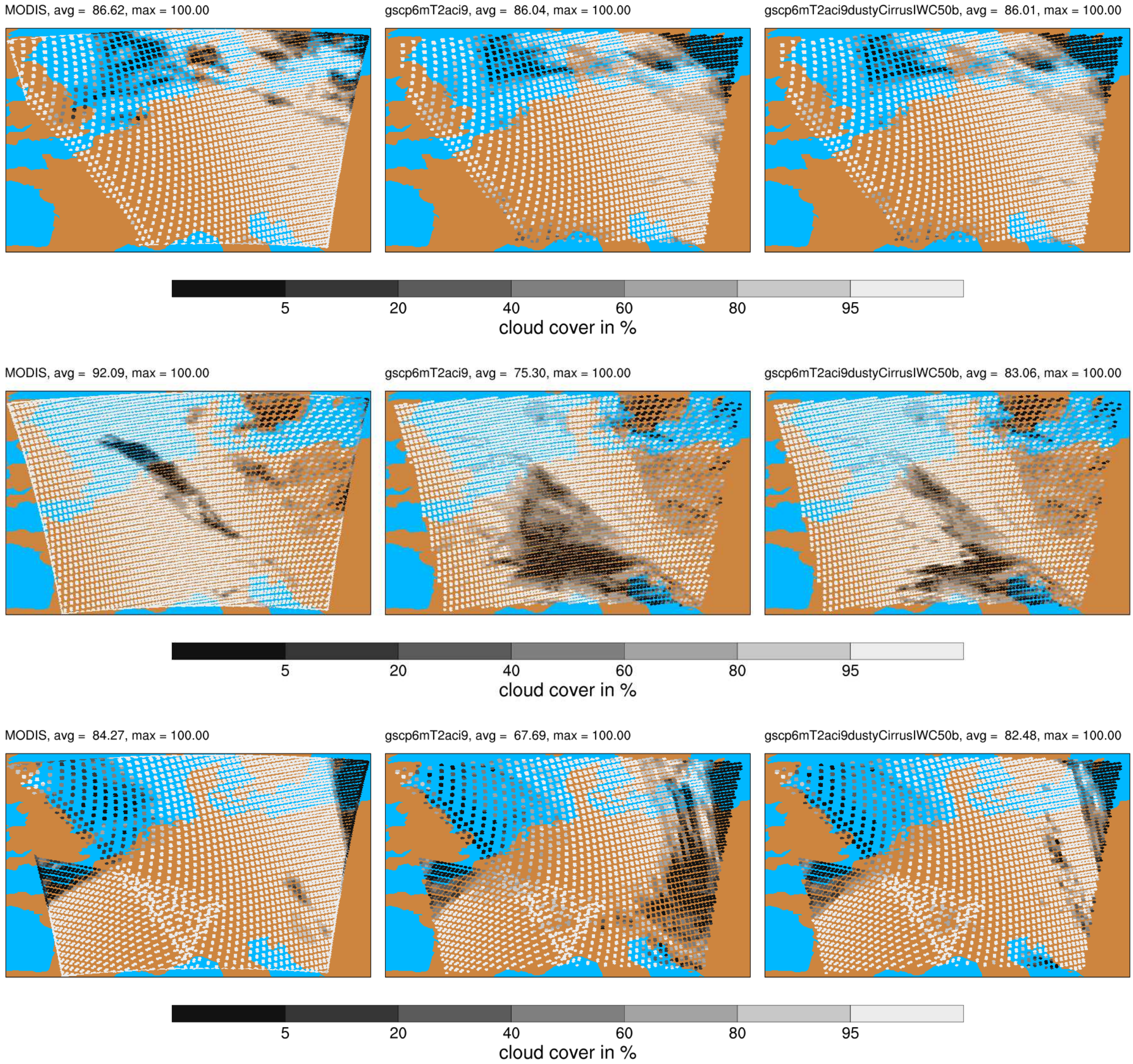

Figure S31. MODIS cloud cover vs ICON-ART for 15 March 2022 11:47 UTC, 16 March 2022 12:30 UTC, and 17 March 11:32 UTC

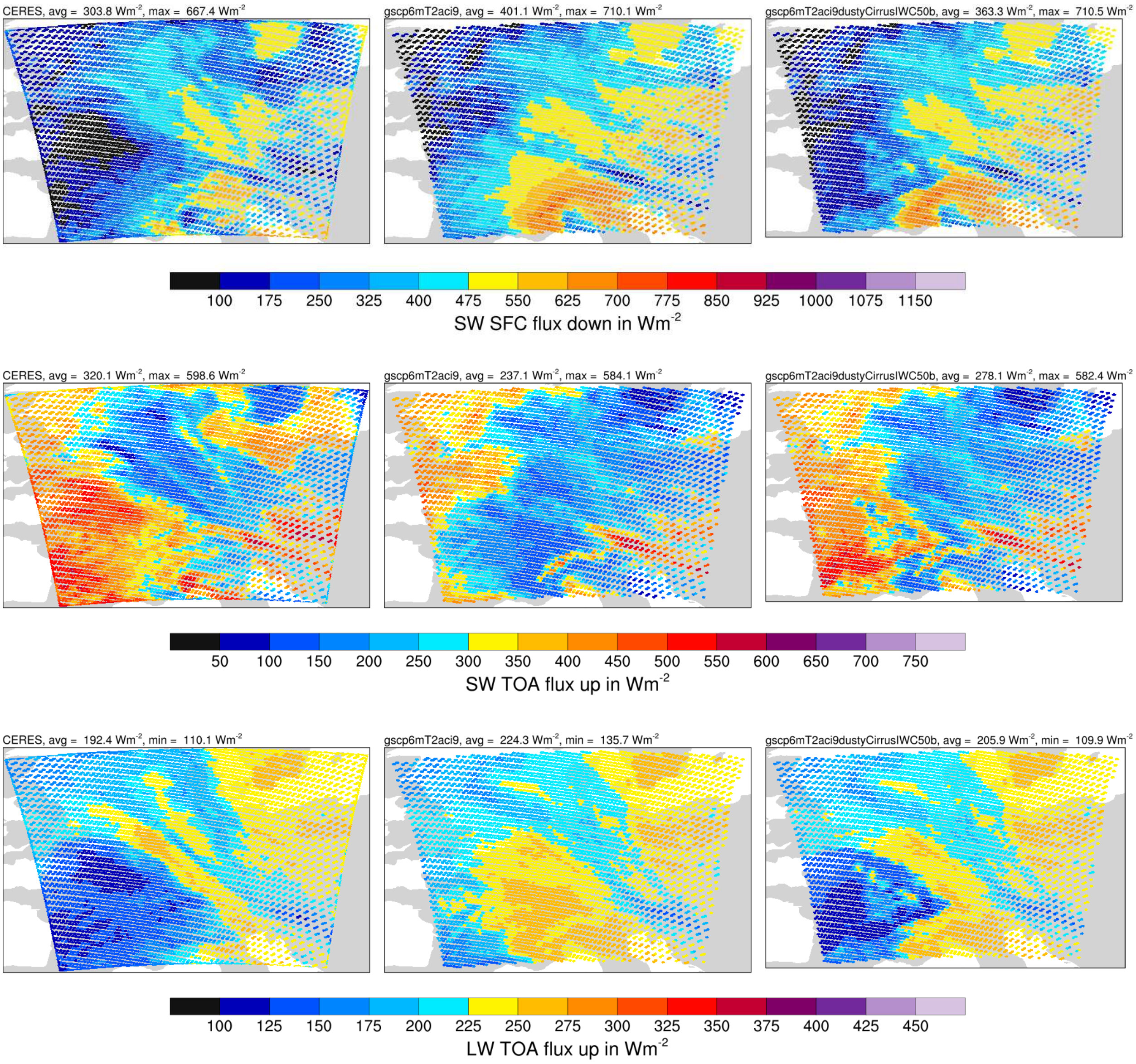

Figure S32. CERES SSF vs ICON-ART for 16 March 2022, 10:30 UTC.

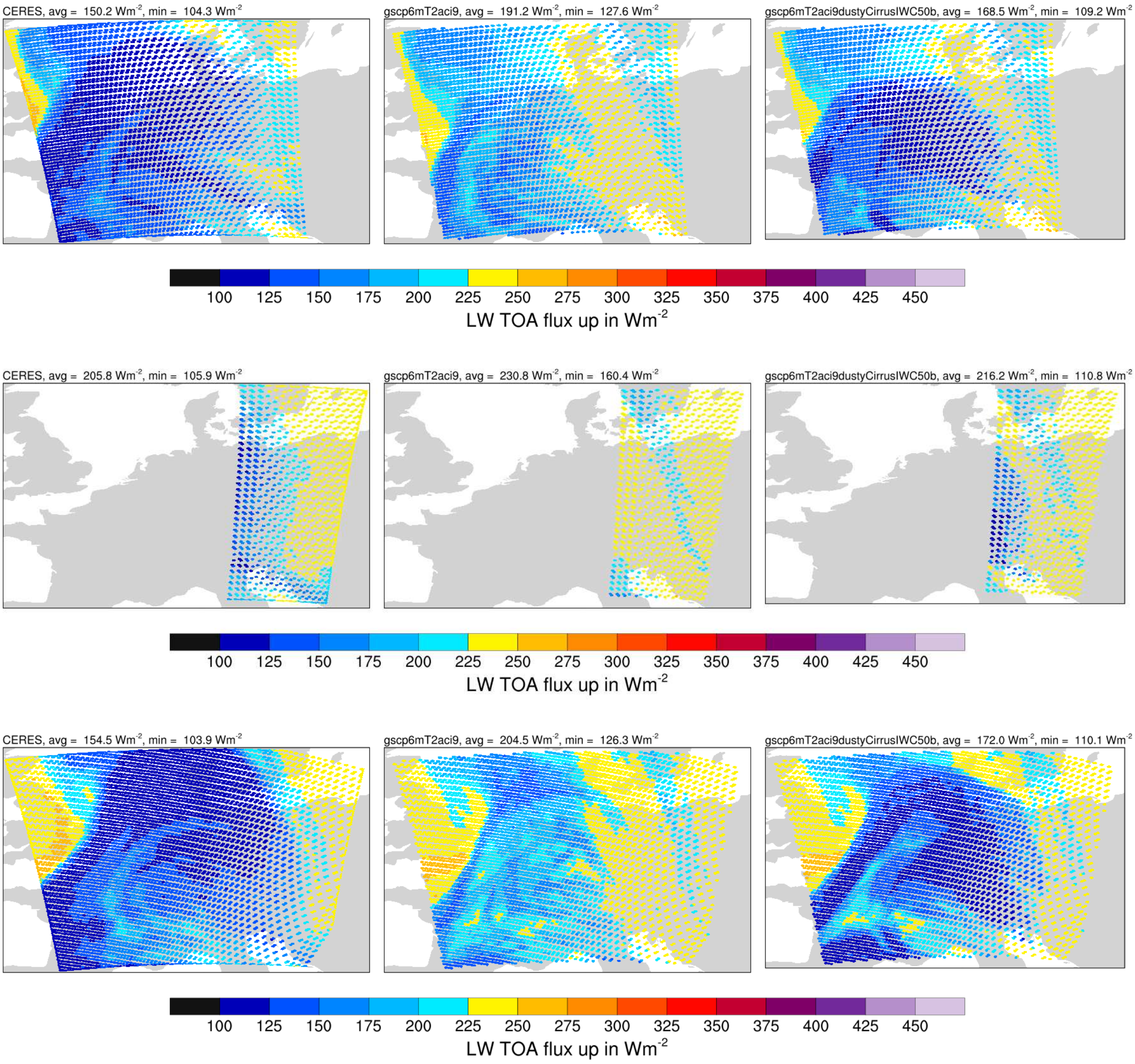

Figure S33. CERES SSF outgoing longwave radaition vs ICON-ART for 16 March 2022 21:47 UTC (top), 17 March 2022 00:23 UTC (middle), and 17 March 2022 02:01 UTC (bottom).

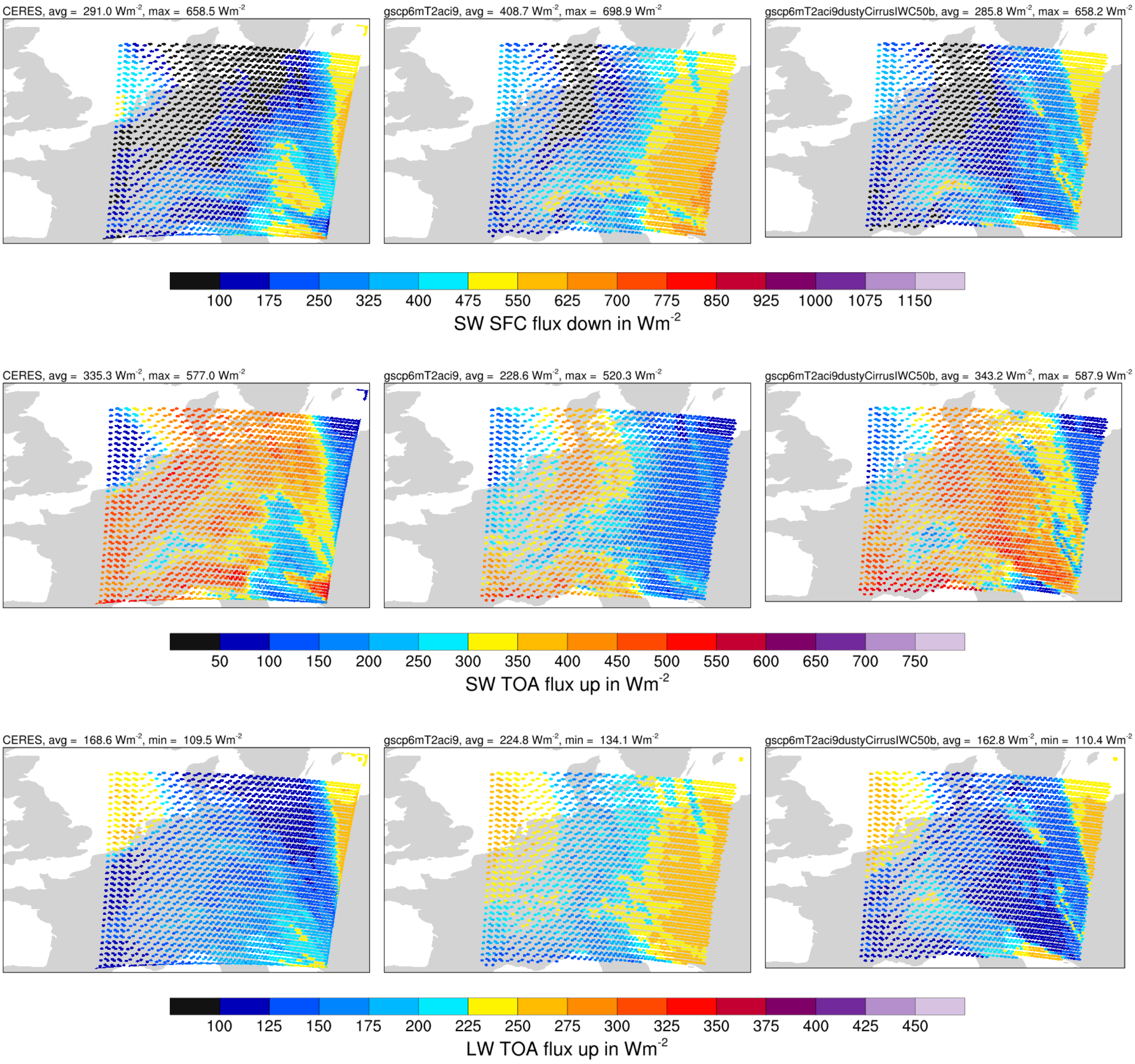

Figure S34. CERES SSF vs ICON-ART for 17 March 2022, 9:40 UTC.

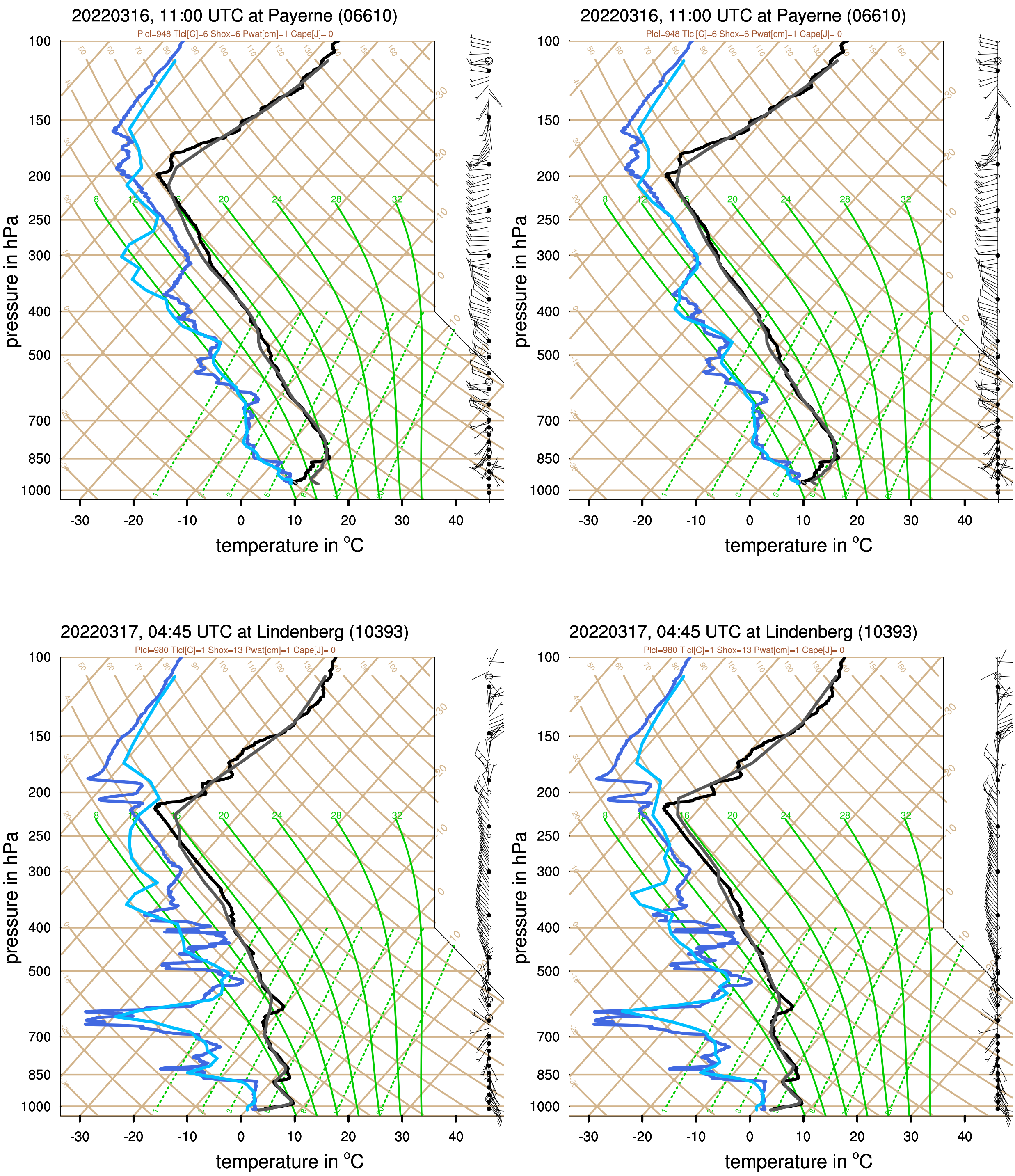

Figure S35. Vertical profiles from radiosonde measurements at Payerne (Switzerland) on 16 March 2022 12 UTC and at Lindenberg (Germany) on 17 March 2022 5 UTC and the corresponding ICON-ART profiles. Shown are skew-T diagrams for ACI (left) and ACI-dusty (right).

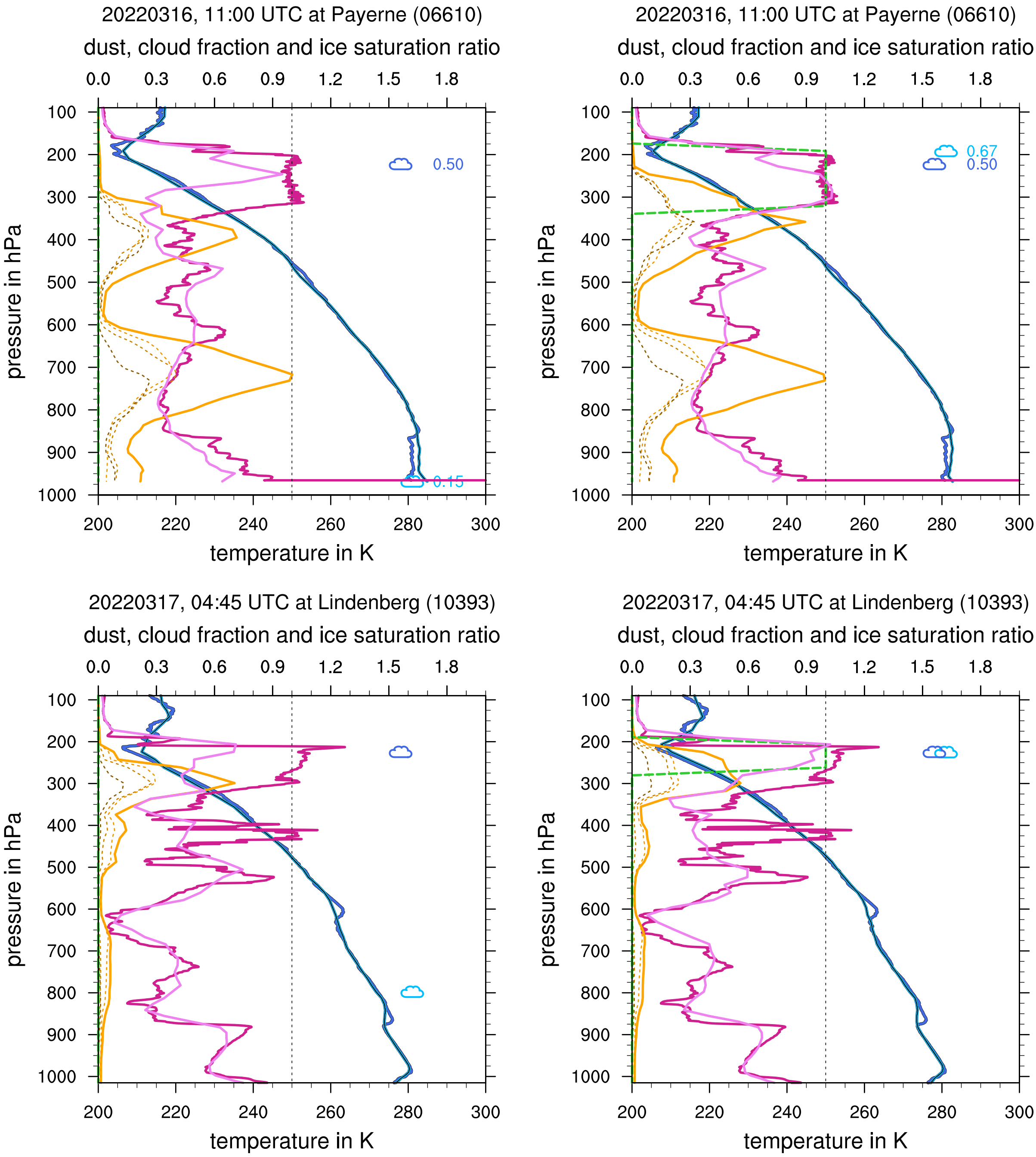

Figure S36. Vertical profiles from radiosonde measurements at Payerne (Switzerland) on 16 March 2022 12 UTC and at Lindenberg (Germany) on 17 March 2022 5 UTC and the corresponding ICON-ART profiles. Observed temperature (black), ICON-ART temperature (blue), observed saturation ratio for ice (dark pink), ICON-ART saturation ratio (lighter pink), normalized total dust concentration of ICON-ART (thick orange), dust modes (other orange and browns), and ICON-ART cloud fraction (green). Cloud symbols indicate the SEVIRI BT (dark blue) and ICON-ART RTTOV BT (light blue) at 10.8 μm for this grid point. Numbers next to the cloud symbol give the visible reflectance (only daytime). Shown are ACI (left) and ACI-dusty (right).

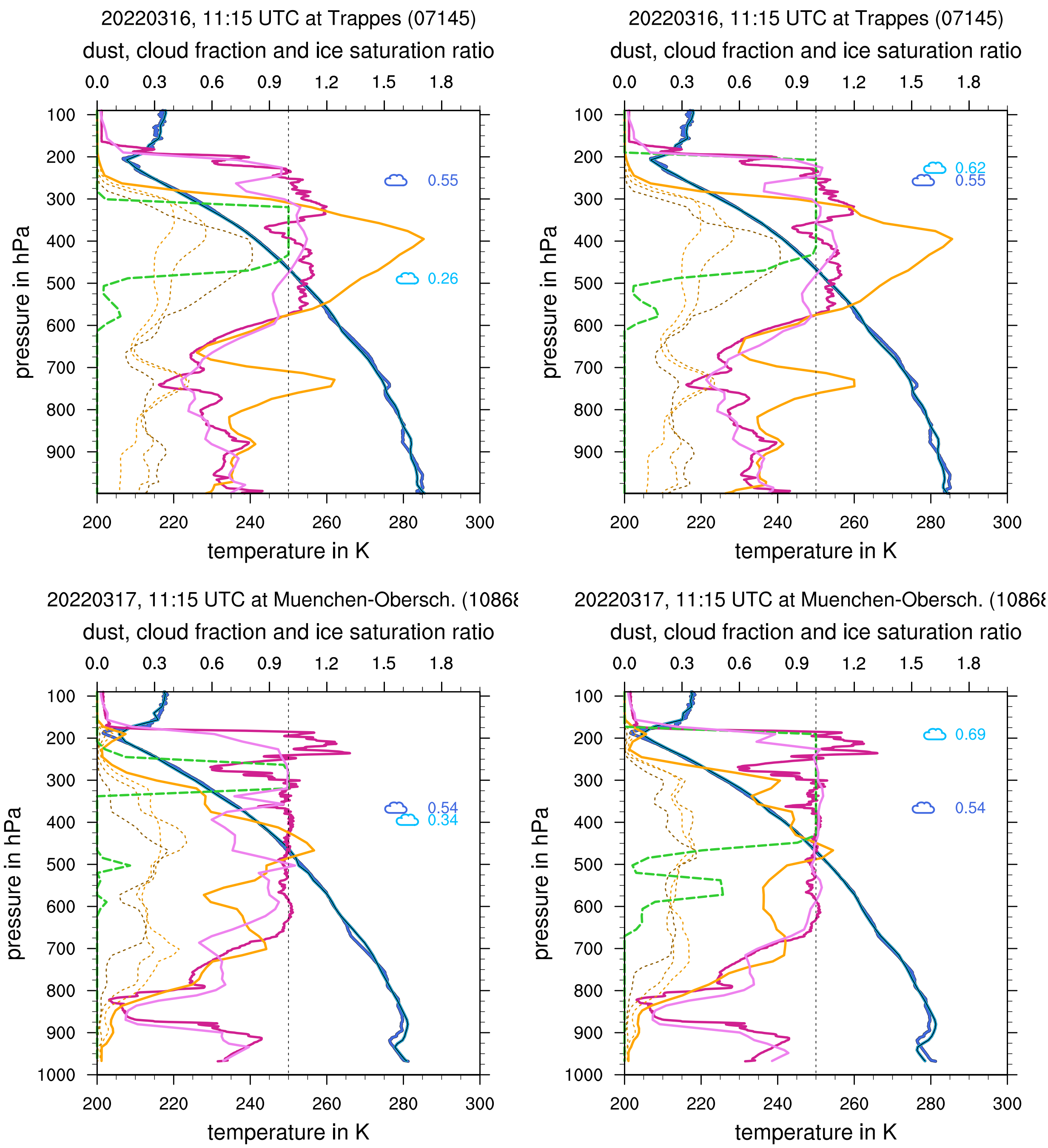

Figure S37. Vertical profiles from radiosonde measurements at Trappes (France) on 16 March 2022 12 UTC and at Munich (Germany) on 17 March 2022 11 UTC and the corresponding ICON-ART profiles. Shown are ACI (left) and ACI-dusty (right).

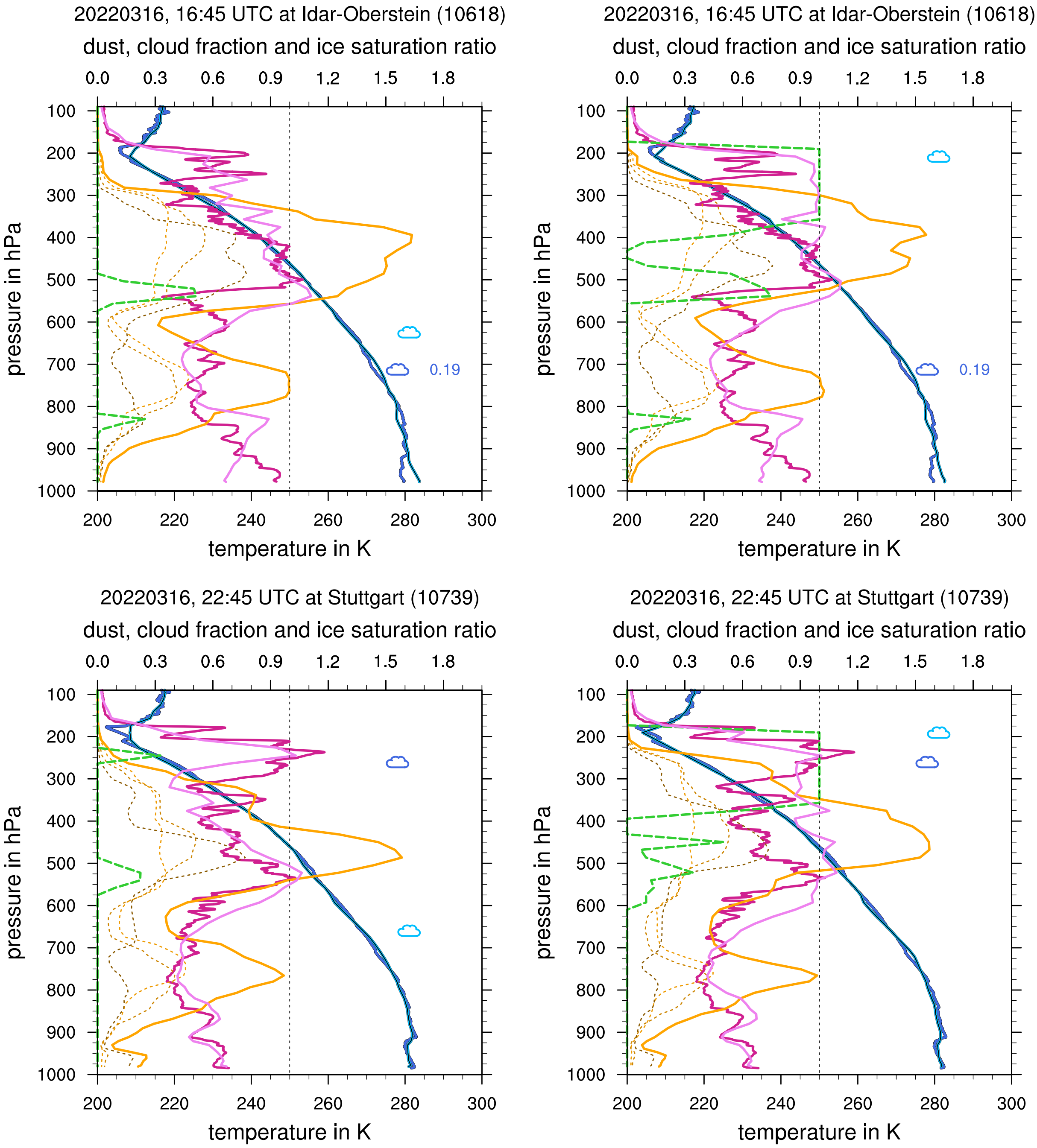

Figure S38. Vertical profiles from radiosonde measurements at Idar-Oberstein (Germany) on 16 March 2022 17 UTC and at Stuttgart (Germany) on 16 March 2022 23 UTC and the corresponding ICON-ART profiles. Shown are ACI (left) and ACI-dusty (right).

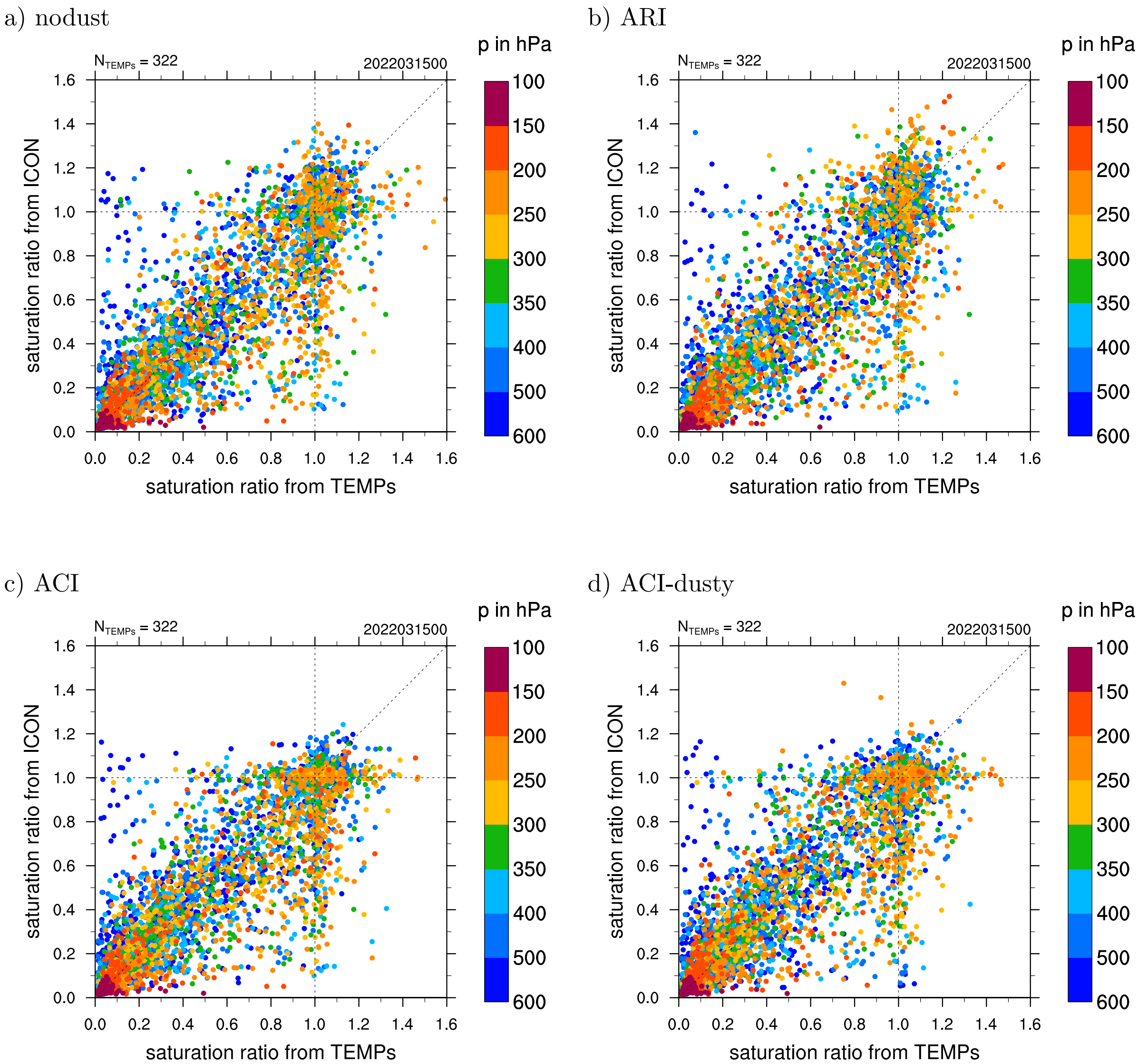

Figure S39. Scatter plots of ice saturation ratio of radiosonde data vs ICON-ART.

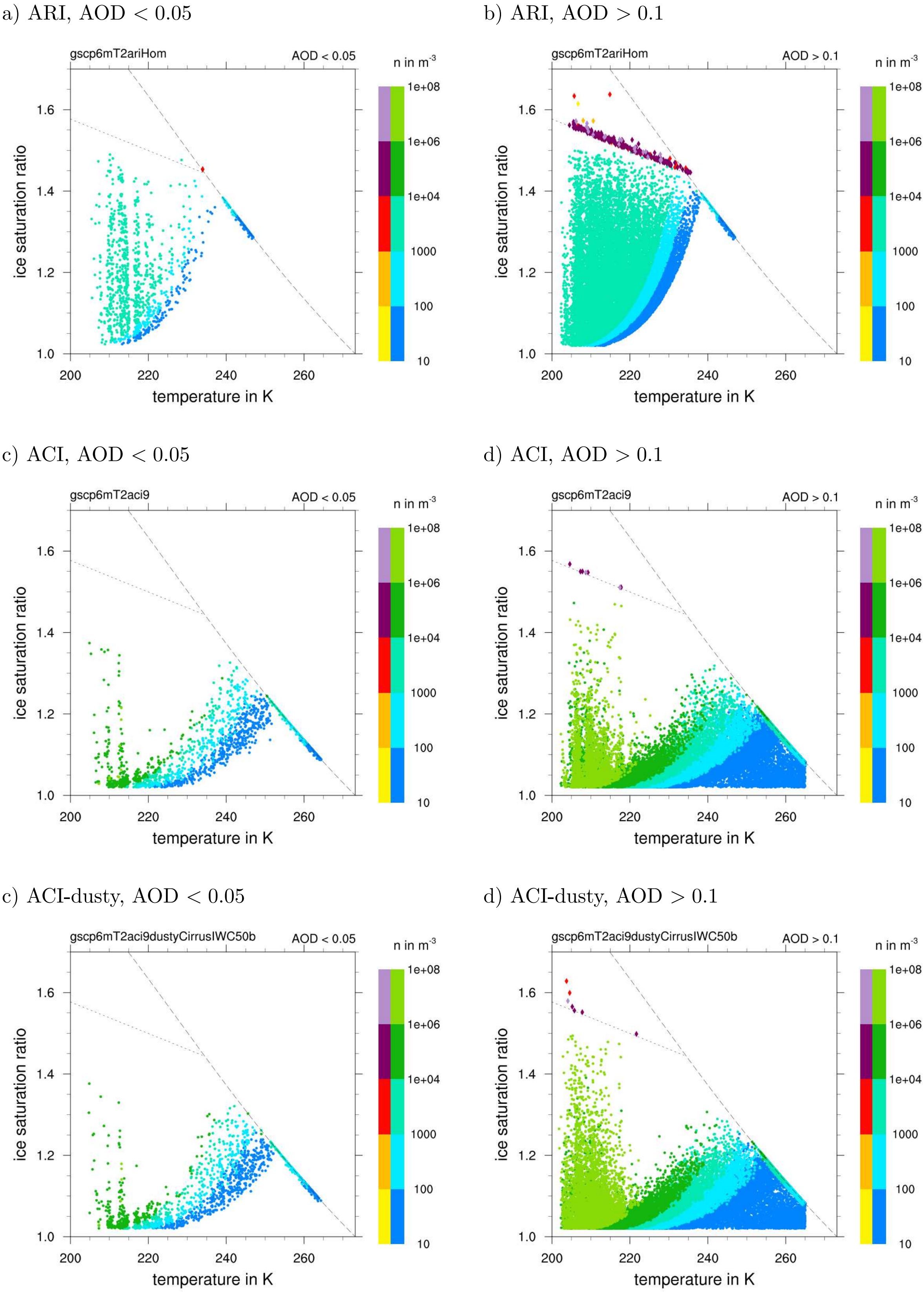

Figure S40. Scatter plots of INP concentration as function of temperature and supersaturation.

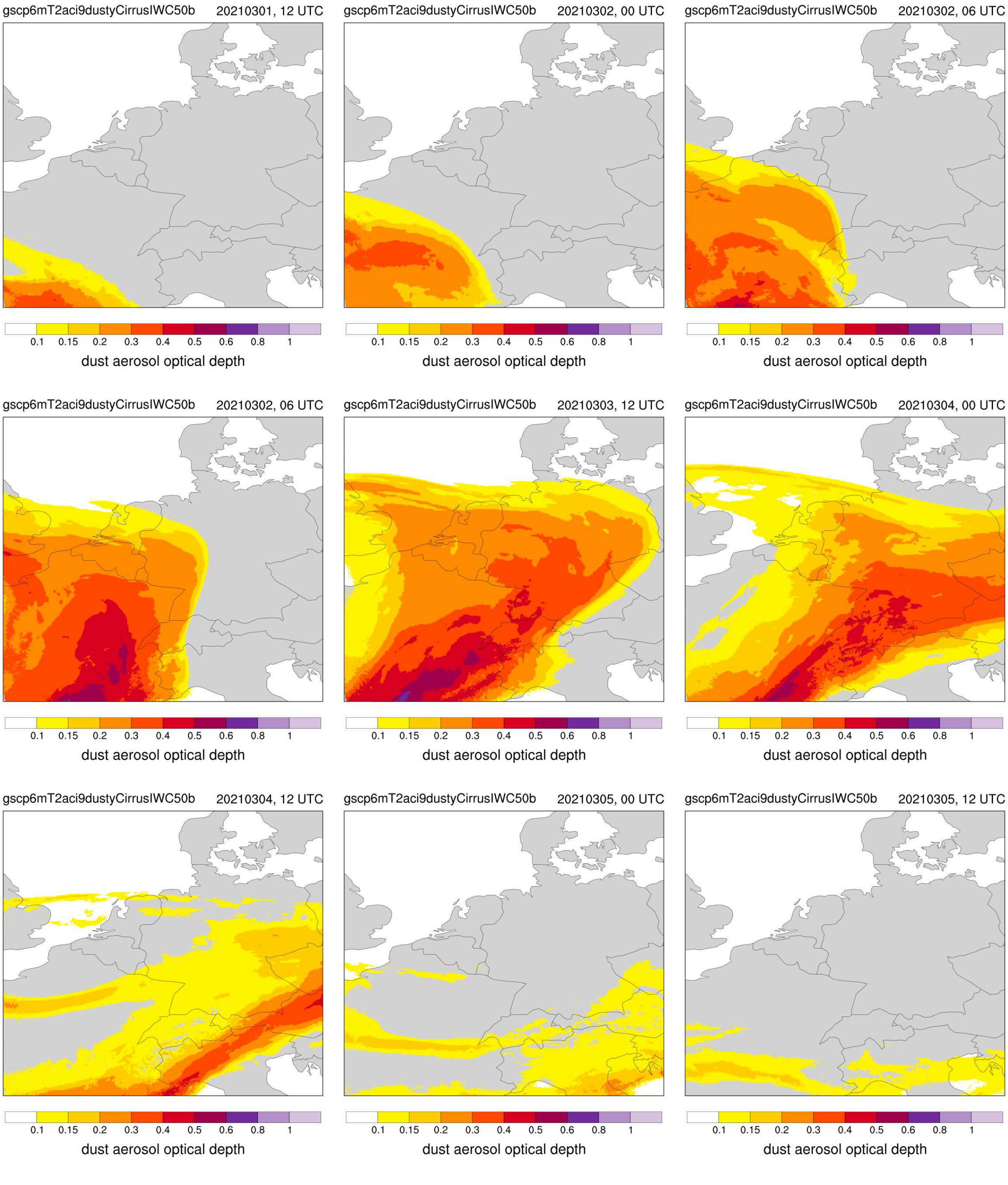

Figure S41. ICON-ART mineral dust AOD for 1-5 March 2022.

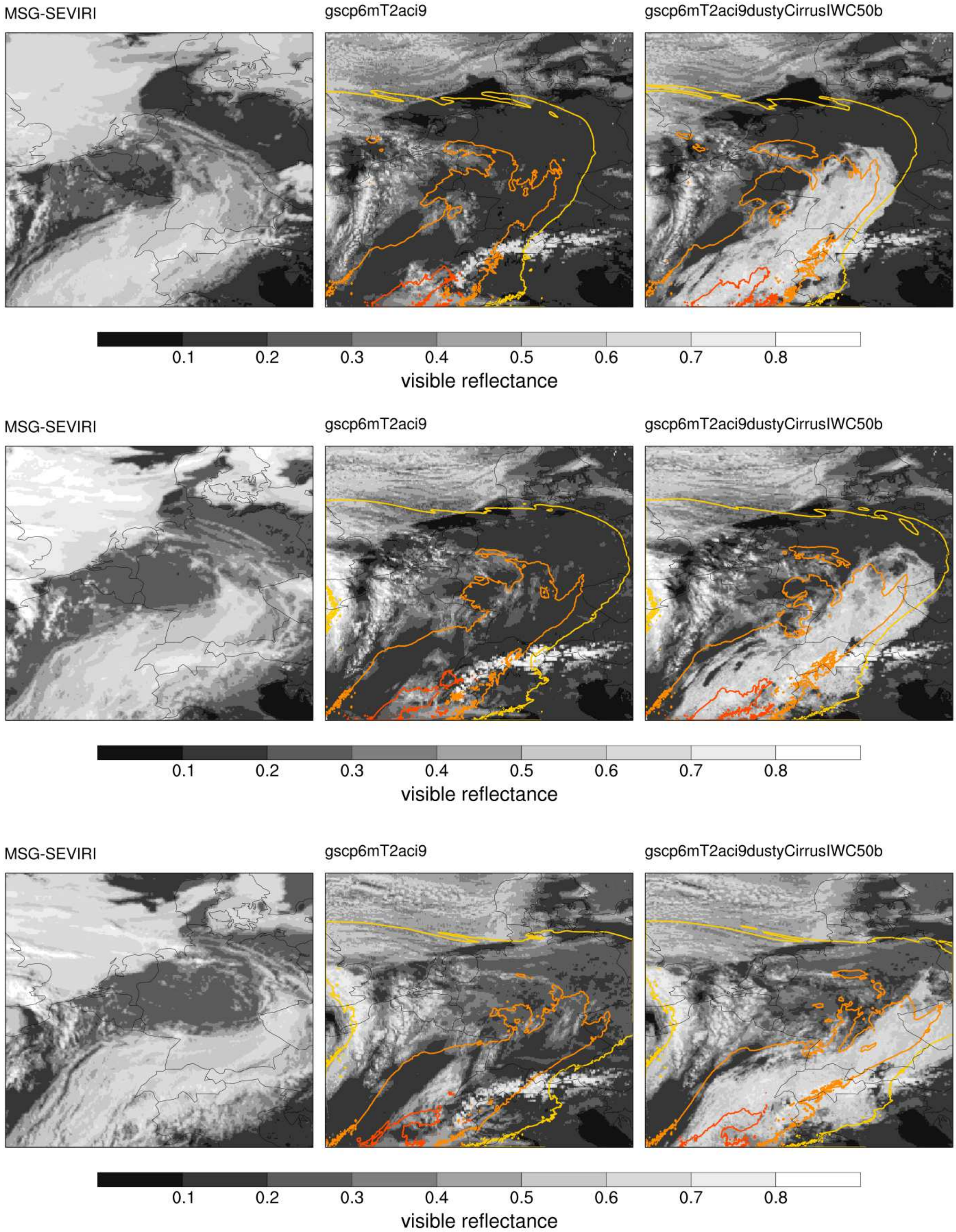

Figure S42. MSG SEVIRI visible reflectance vs ICON-ART for 3-5 March 12 UTC (top to bottom). For ICON-ART the mineral dust AOD is shown with isolines from 0.1 to 0.5 (yellow-orange-red) with intervals of 0.2.

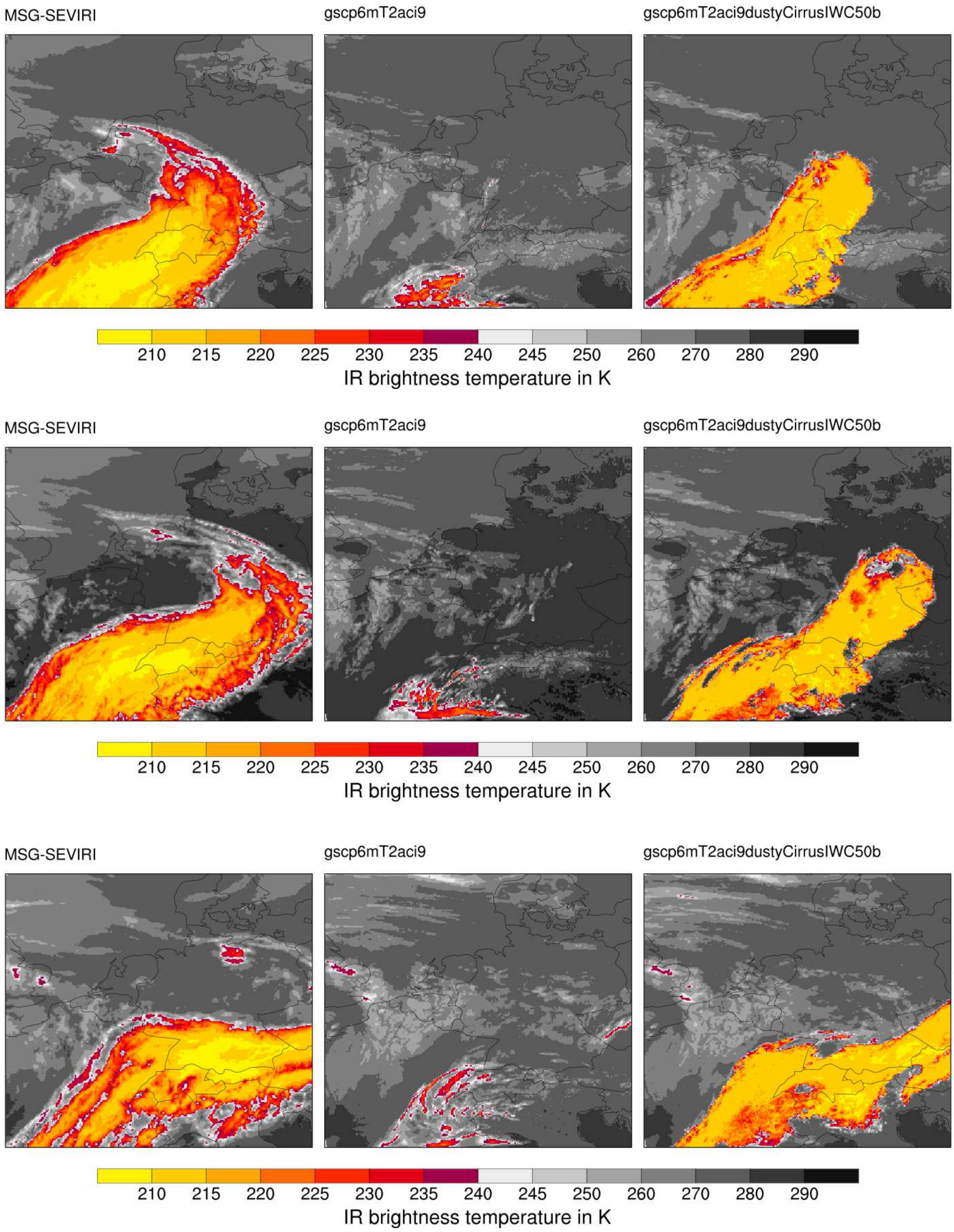

Figure S43. MSG SEVIRI infrared at 10.8 μm vs ICON-ART for 15 March 2022 12 UTC, 16 March 00 UTC and 16 March 12 UTC (top to bottom).

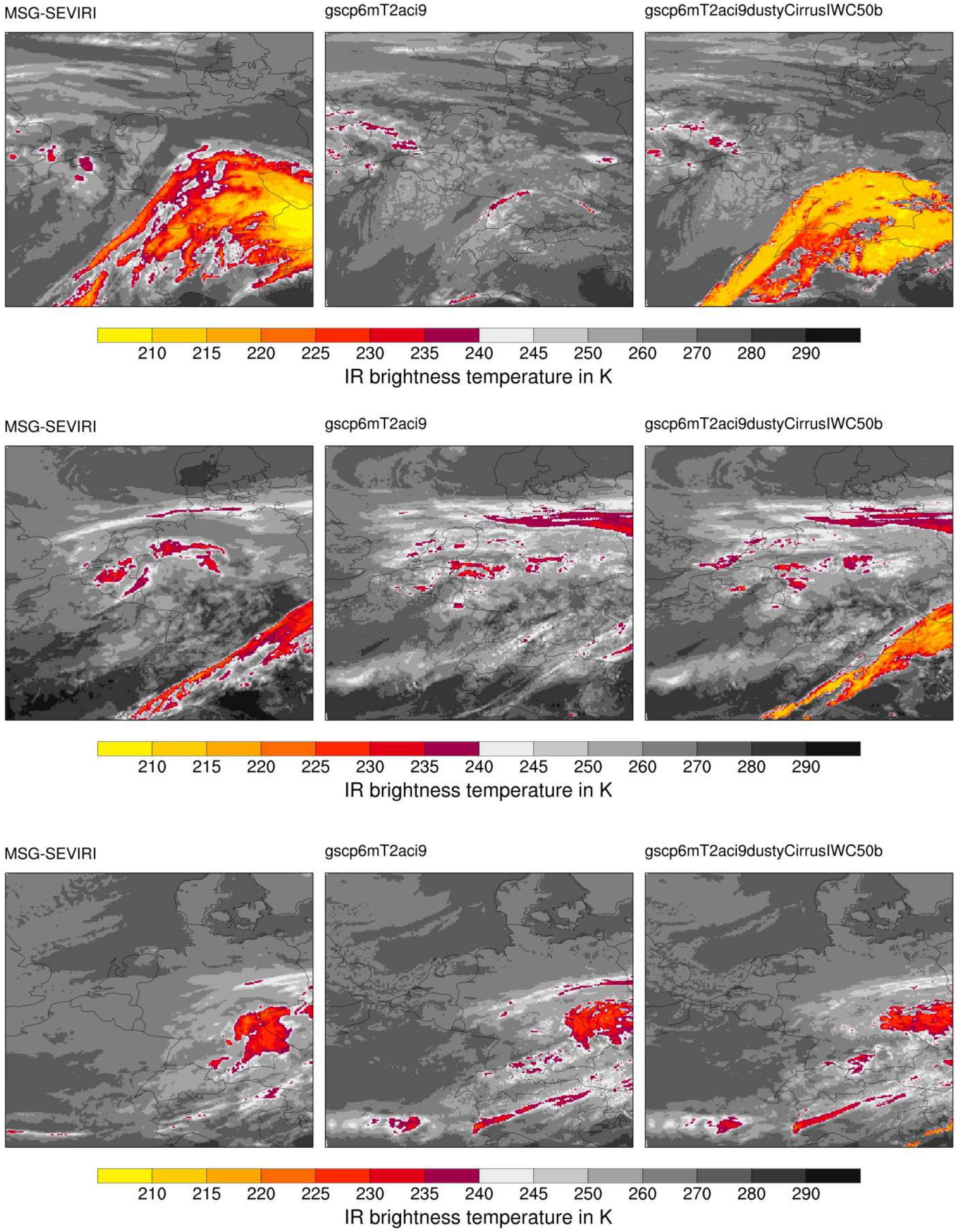

Figure S44. MSG SEVIRI infrared at 10.8 μm vs ICON-ART for 3-4 March 2022 (top to bottom).

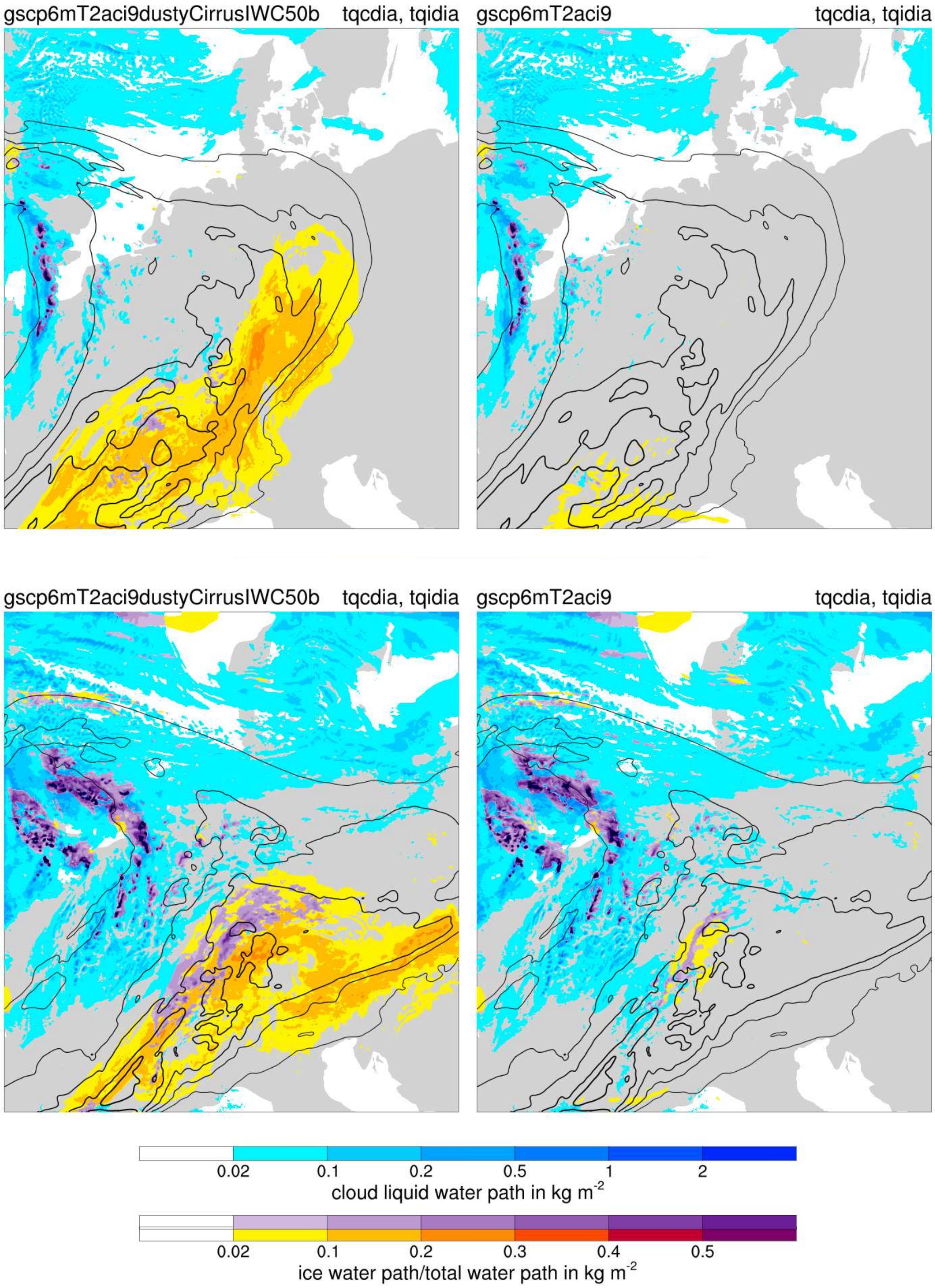

Figure S45. Ice water path (orange-red), cloud water path (blue), and total water path (magenta) for 3 March 2021 12 UTC and 4 March 2021 00 UTC. IWP is shown for column with only ice, LWP for columuns with liquid only, and TWP for column with mixed-phase or multi-layer clouds that contain ice and liquid. The IWP and TWP do include the sub-grid diagnostic contribution, e.g., from the dusty cirrus parameterization. Shown are the ACI (right) and the ACI-dusty (left) simulations of ICON-ART. Isolines are the mineral dust AOD with intervals of 0.1.

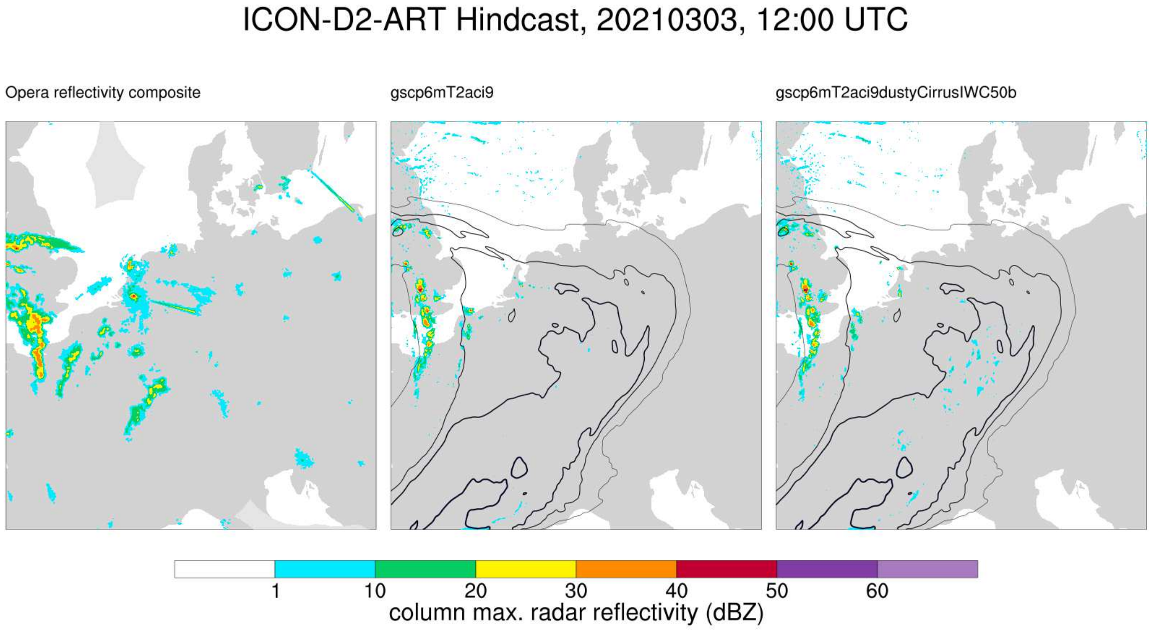

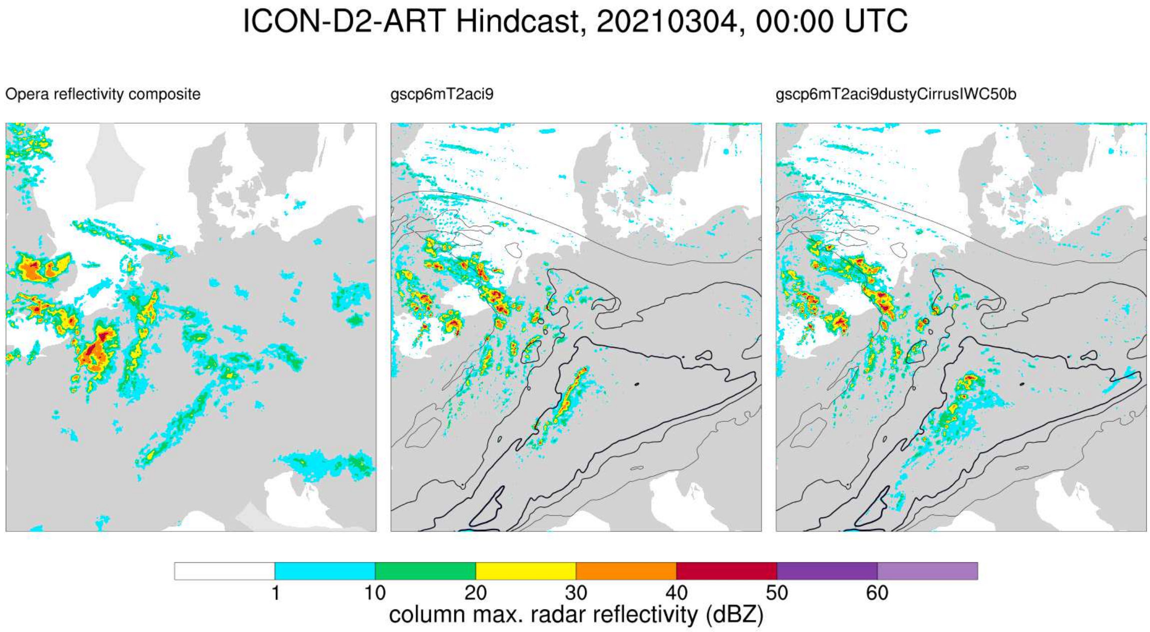

Figure S46. Column-maximum radar reflectivity factor in dBZ for 3 March 2021 12 UTC and 4 March 2022 00 UTC. Shown is the Opera composit (left), the ACI simulation (center), and the ACI-dusty simulation (right). Isolines are the mineral dust AOD at 0.1, 0.2, 0.3 and 0.5

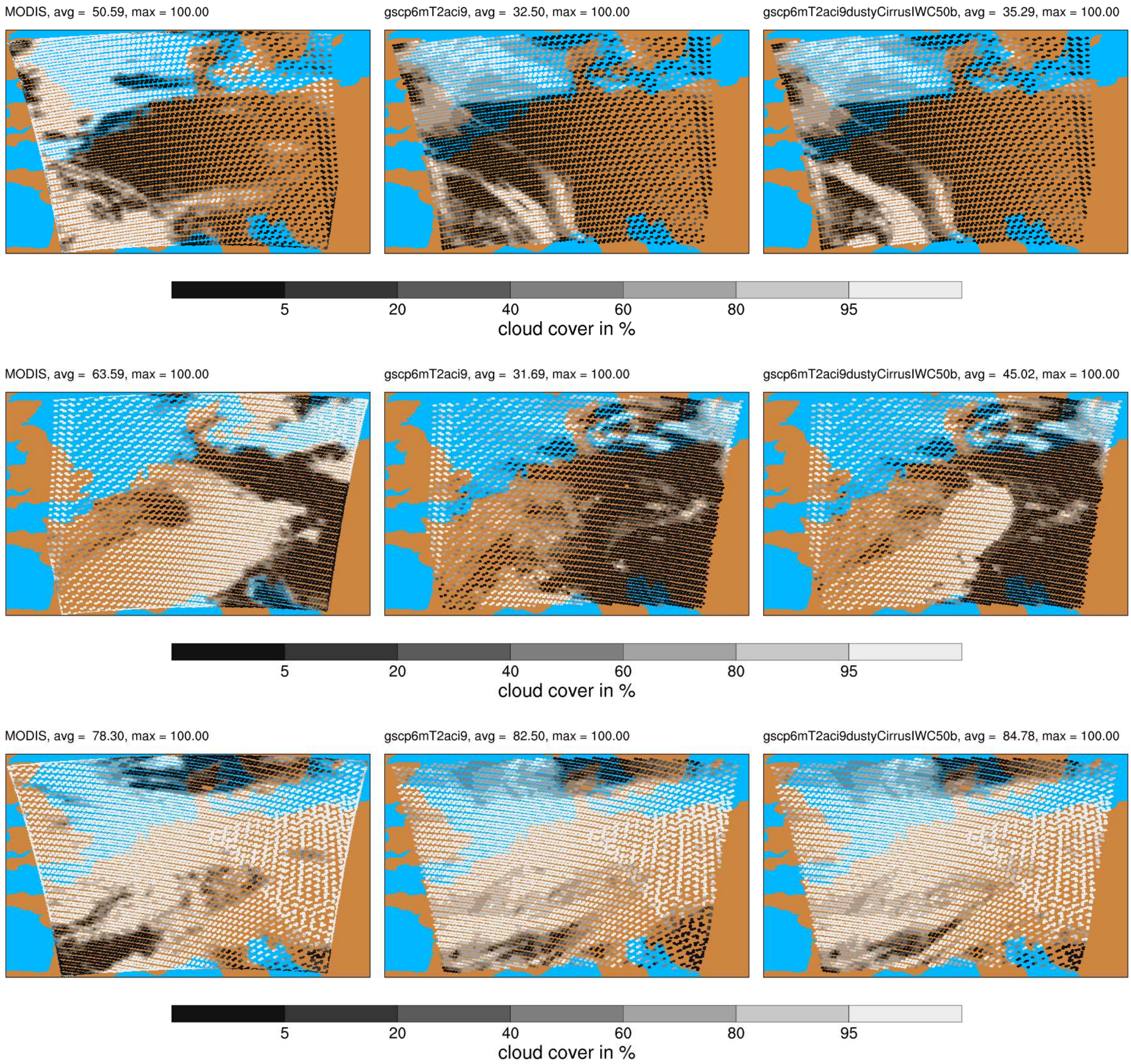

Figure S47. MODIS cloud cover vs ICON-ART for 2 March 2021 12:50 UTC, 3 March 2021 10:05 UTC, and 4 March 10:50 UTC

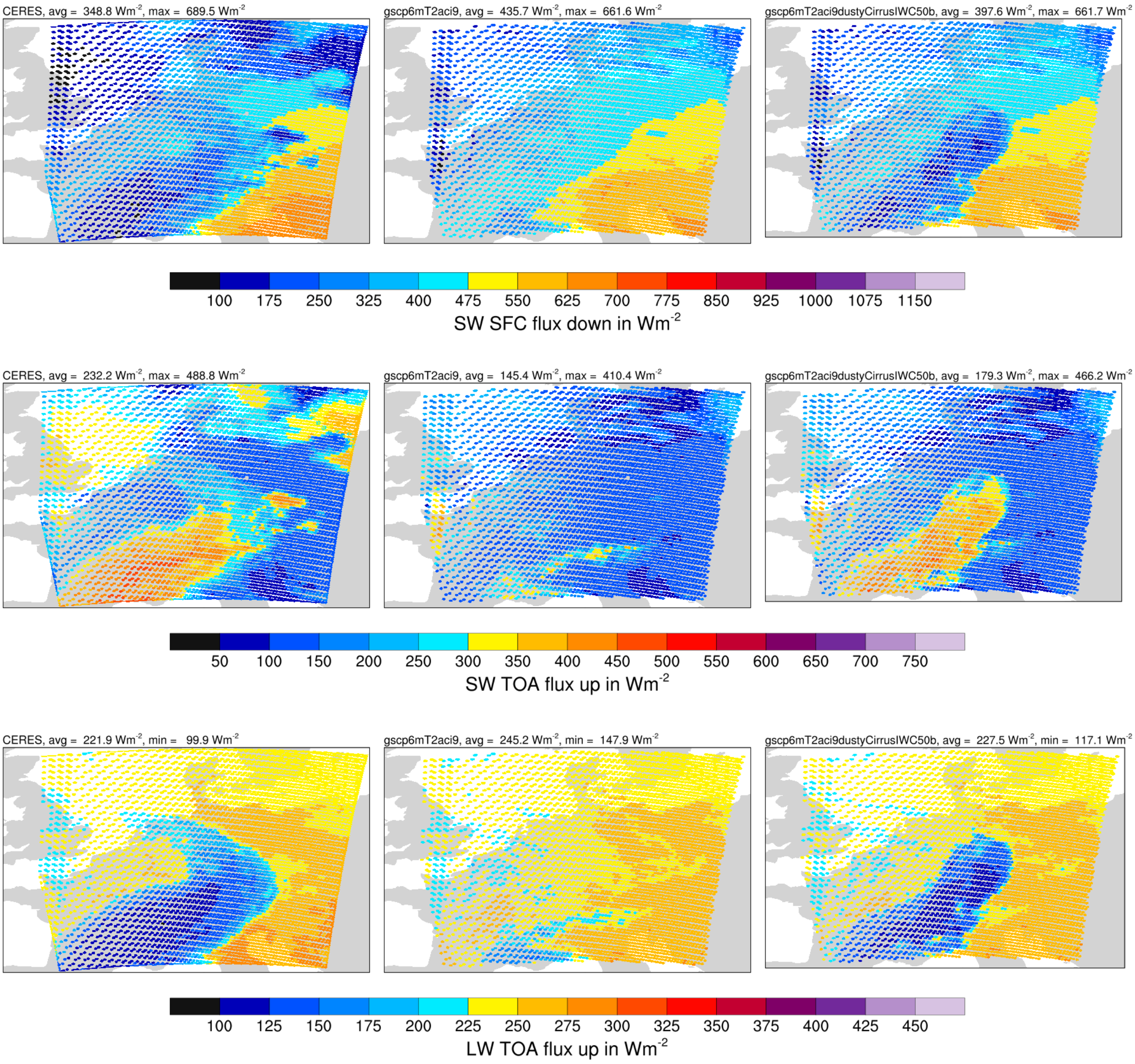

Figure S48. CERES SSF vs ICON-ART for 3 March 2021, 10:10 UTC.

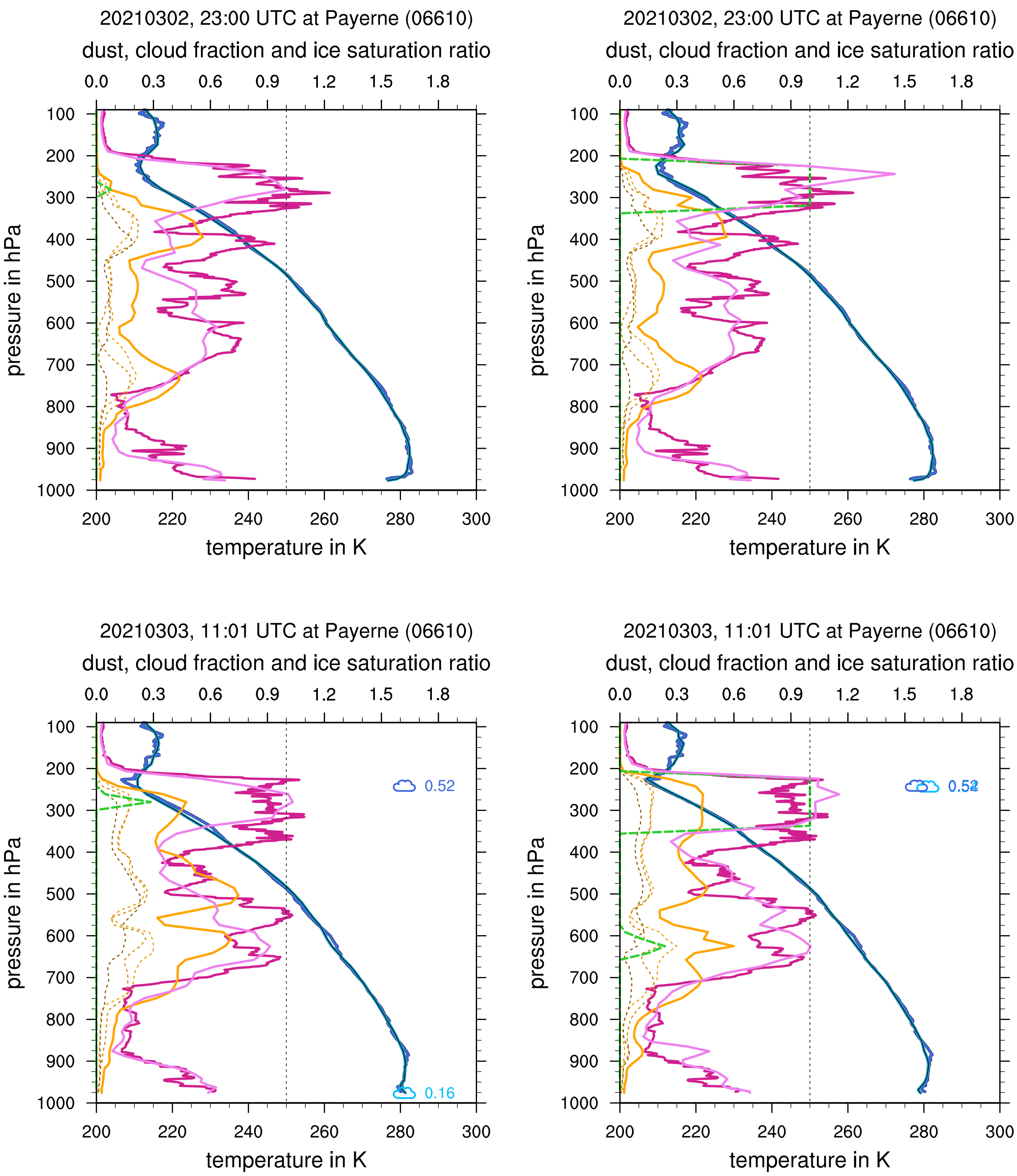

Figure S49. Vertical profiles from radiosonde measurements at Payerne (Switzerland) 2 March 2021 23 UTC and 3 March 11 UTC and the corresponding ICON-ART profiles. Note that the SEVIRI data is missing for 2 March 23 UTC. Shown are ACI (left) and ACI-dusty (right).

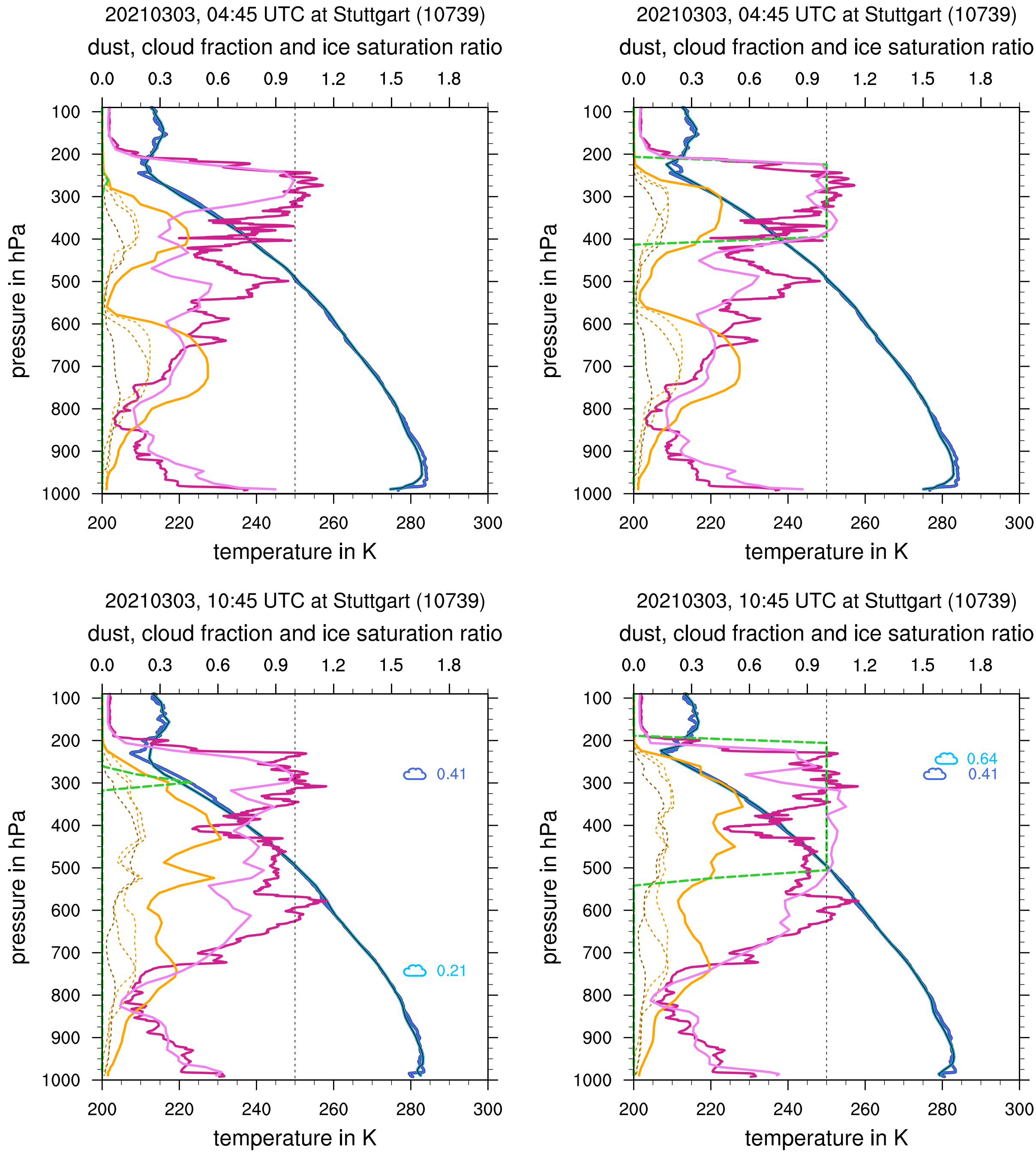

Figure S50. Vertical profiles from radiosonde measurements at Stuttgart (Germany) on 3 March 2021 5 UTC and 11 UTC and the corresponding ICON-ART profiles. Observed temperature (black), ICON-ART temperature (blue), observed saturation ratio for ice (dark pink), ICON-ART saturation ratio (lighter pink), normalized total dust concentration of ICON-ART (thick orange), dust modes (other orange and browns), and ICON-ART cloud fraction (green). Cloud symbols indicate the SEVIRI BT (dark blue) and ICON-ART RTTOV BT (light blue) at 10.8 μm for this grid point. Numbers next to the cloud symbol give the visible reflectance (only daytime). Note that the SEVIRI data is missing for 3 March 5 UTC. Shown are ACI (left) and ACI-dusty (right).

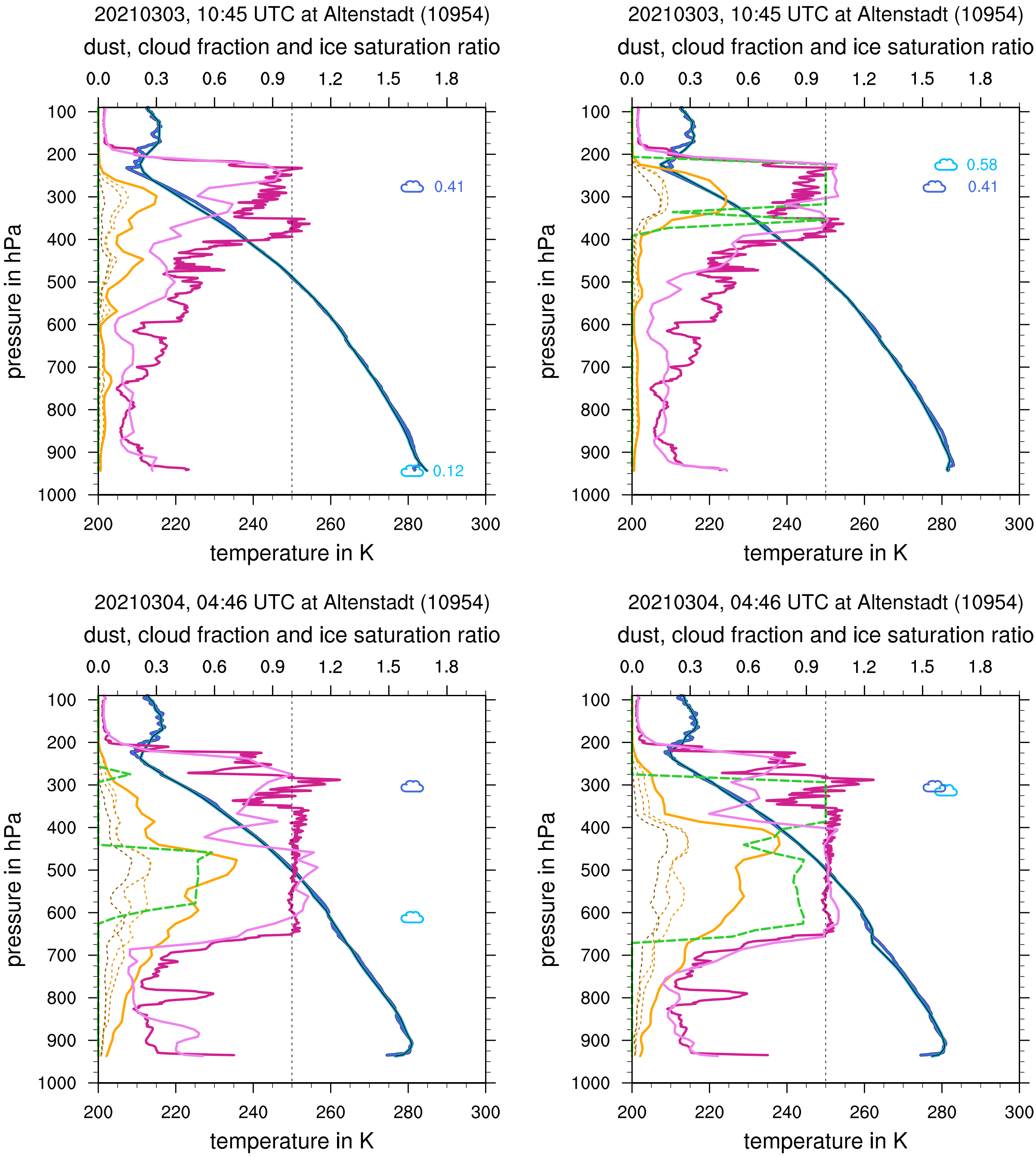

Figure S51. Vertical profiles from radiosonde measurements at Altenstadt (Germany) on 3 March 2021 11 UTC and 4 March 2021 5 UTC and the corresponding ICON-ART profiles. Shown are ACI (left) and ACI-dusty (right).

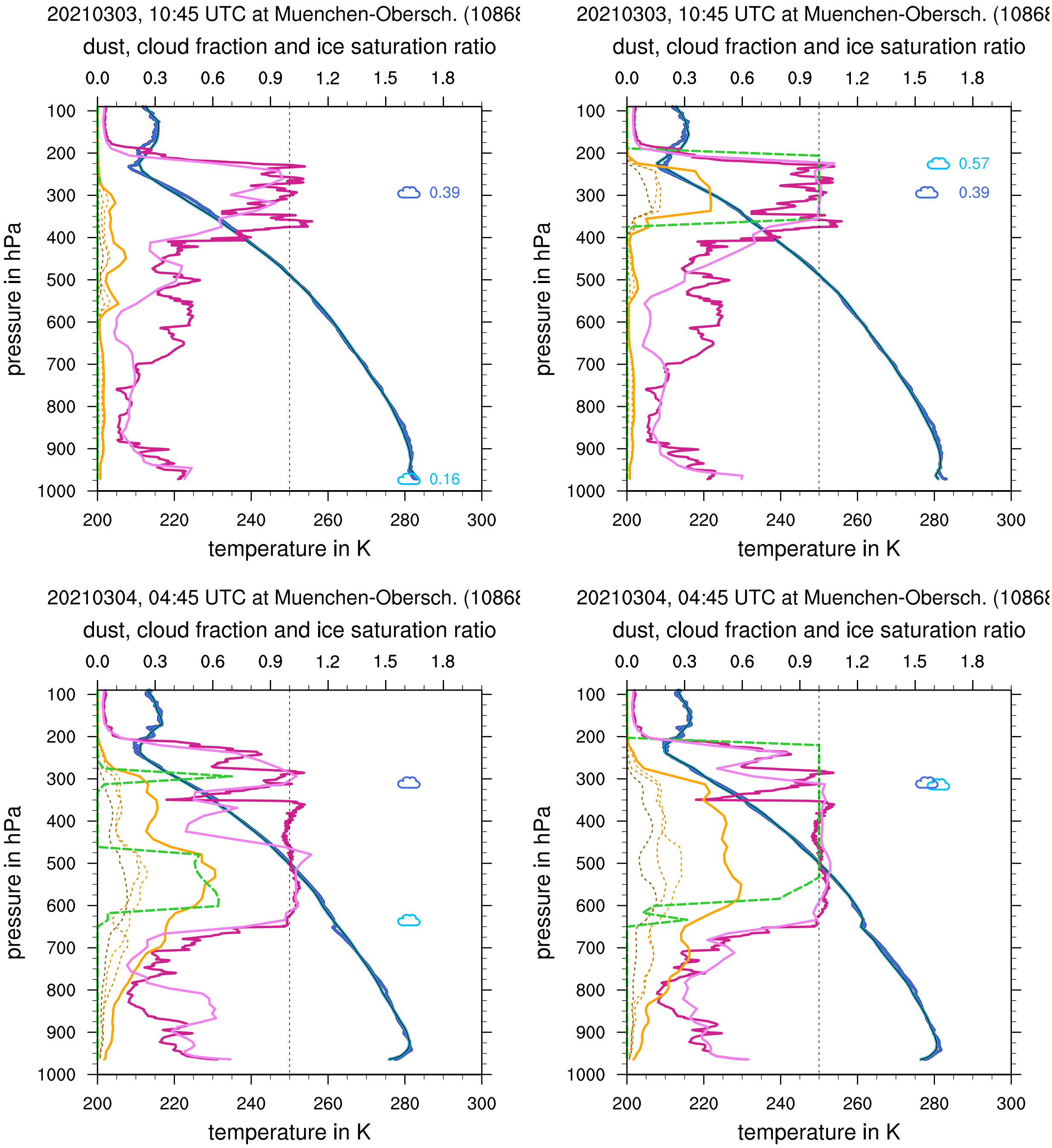

Figure S52. Vertical profiles from radiosonde measurements at Munich (Germany) on 3 March 2021 11 UTC and 4 March 2021 5 UTC and the corresponding ICON-ART profiles. Shown are ACI (left) and ACI-dusty (right).

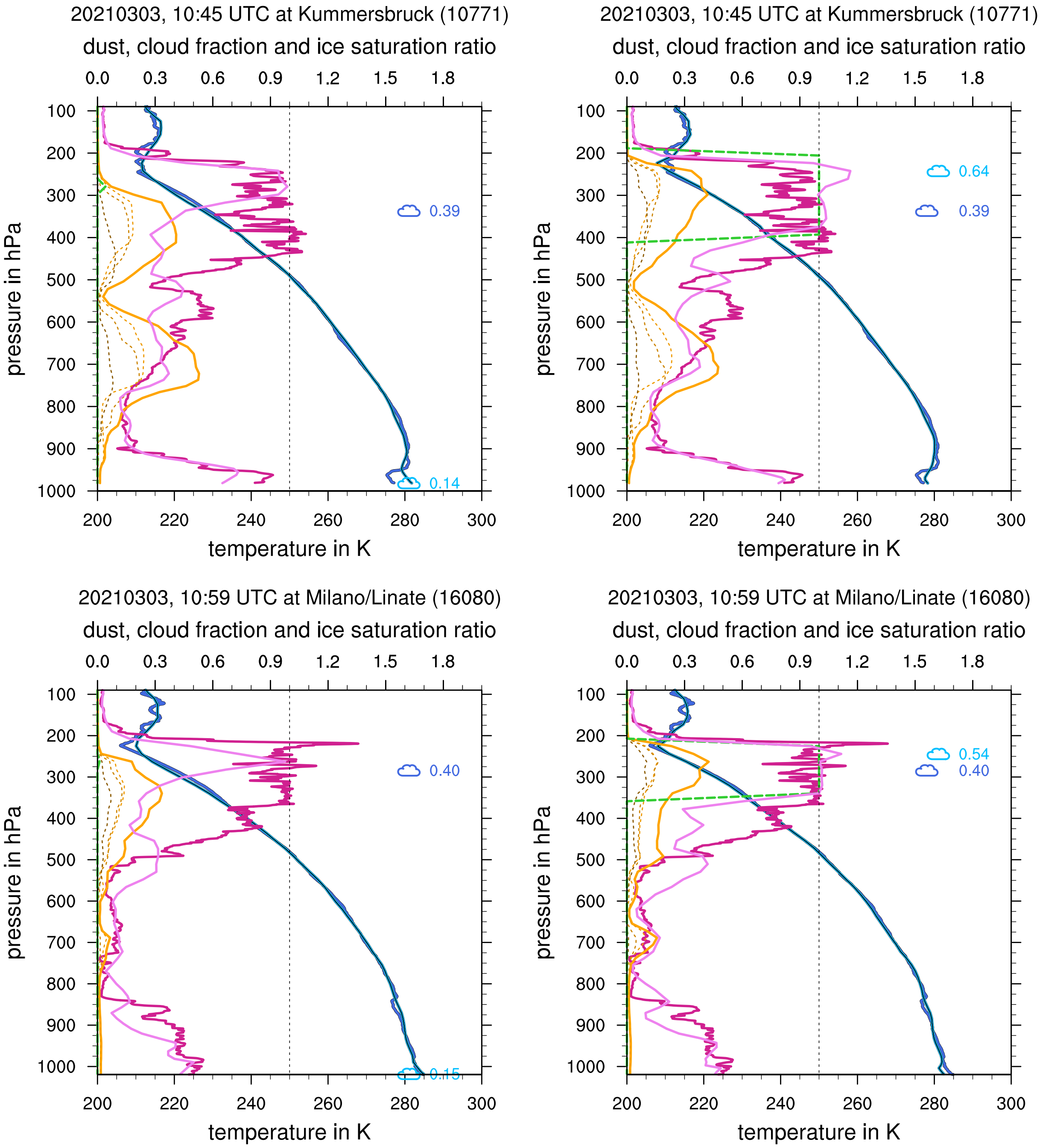

Figure S53. Vertical profiles from radiosonde measurements at Kümmersbruck (Germany) on 3 March 2021 11 UTC and at Milano (Italy) on 3 March 2021 11 UTC and the corresponding ICON-ART profiles. Shown are ACI (left) and ACI-dusty (right).

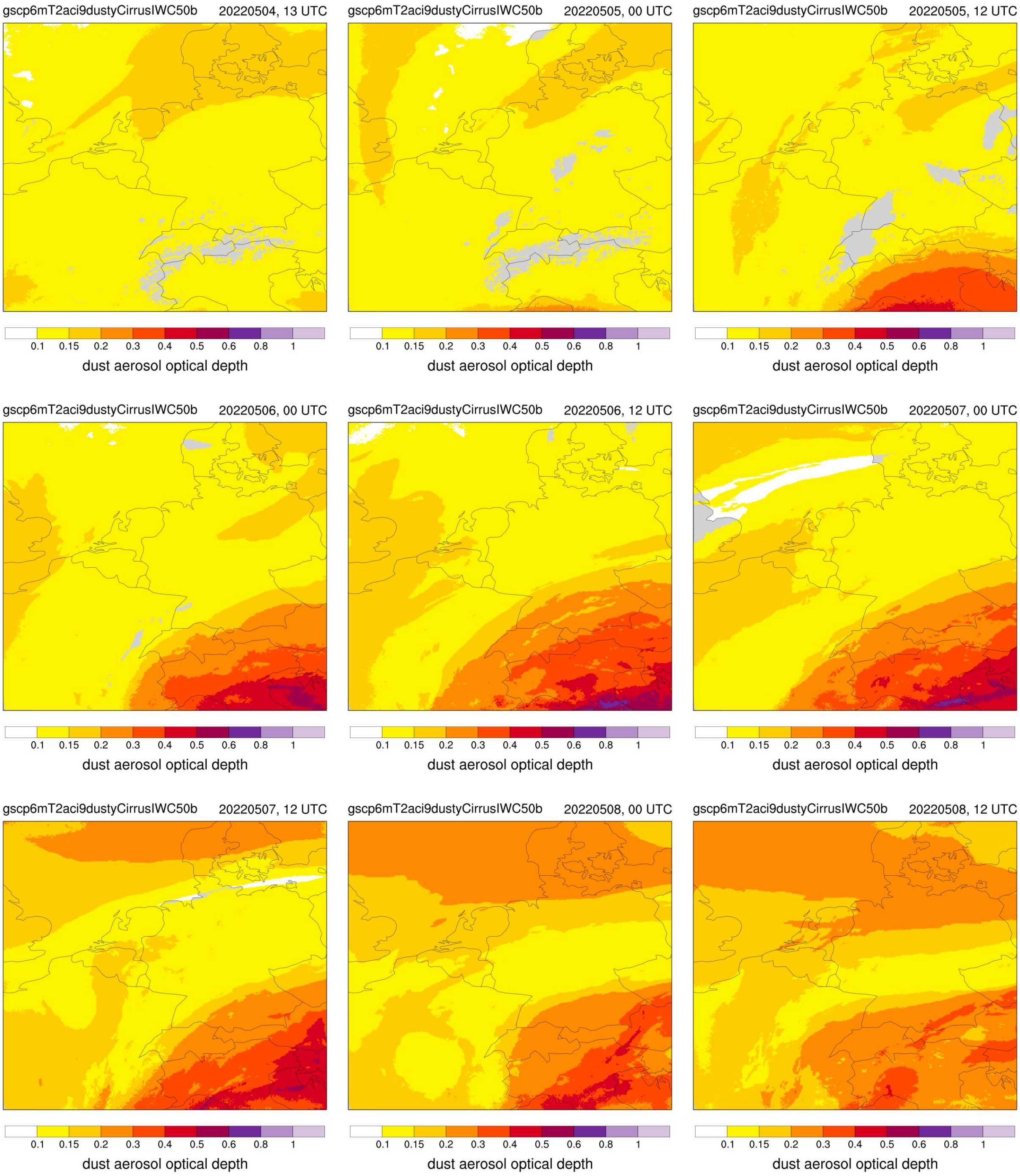

Figure S54. ICON-ART mineral dust AOD for 4-8 May 2022.

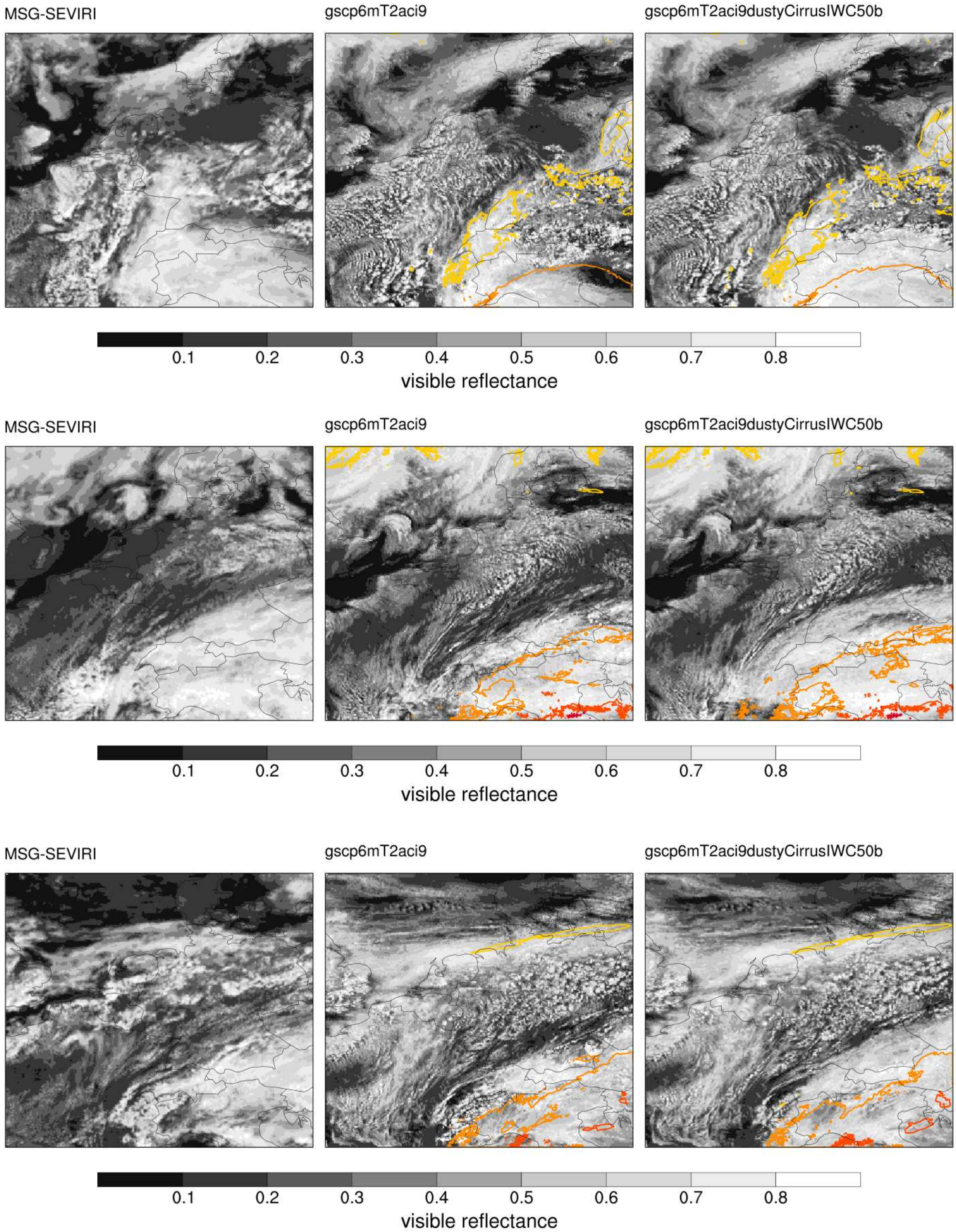

Figure S55. MSG SEVIRI visible reflectance vs ICON-ART for or 5 May 2022 12 UTC, 6 May 12 UTC and 7 May 12 UTC (top to bottom). For ICON-ART the mineral dust AOD is shown with isolines from 0.1 to 0.7 (yellow-orange-red) with intervals of 0.2.

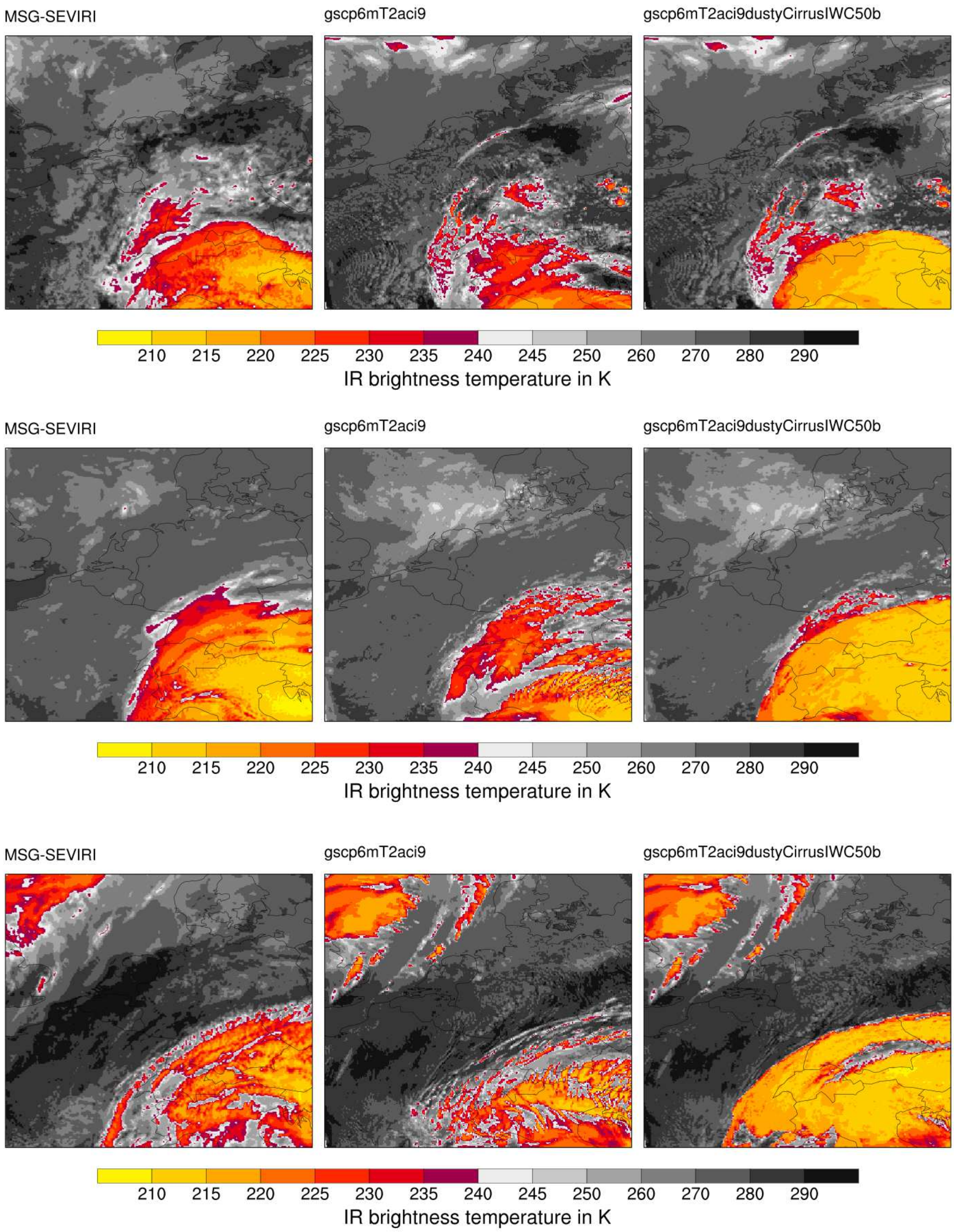

Figure S56. MSG SEVIRI infrared at 10.8 μm vs ICON-ART for 5 May 2022 12 UTC, 6 May 00 UTC and 6 May 12 UTC (top to bottom).

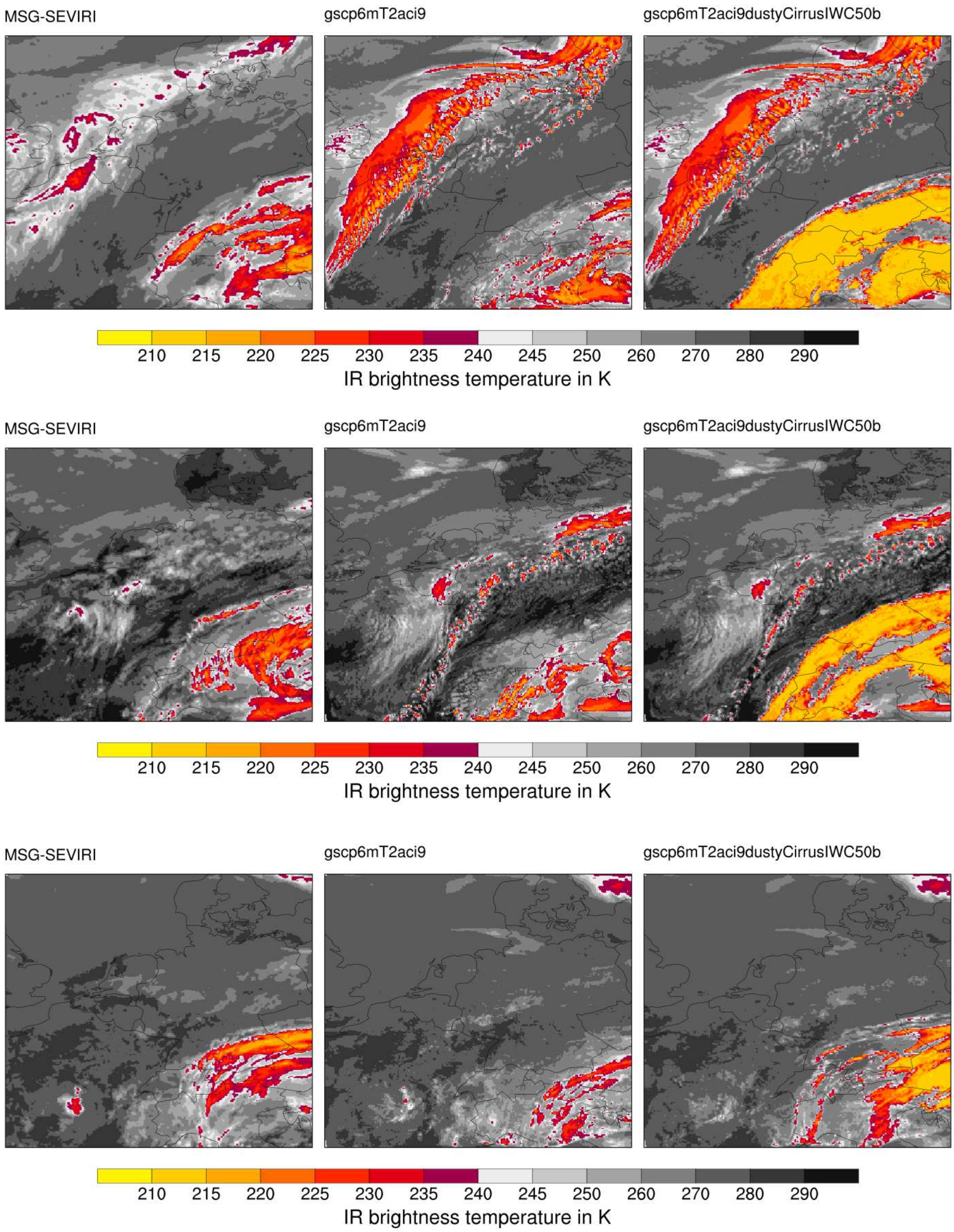

Figure S57. MSG SEVIRI infrared at 10.8 μm vs ICON-ART for 7 May 2022 00 UTC, 7 May 12 UTC and 8 May 00 UTC (top to bottom).

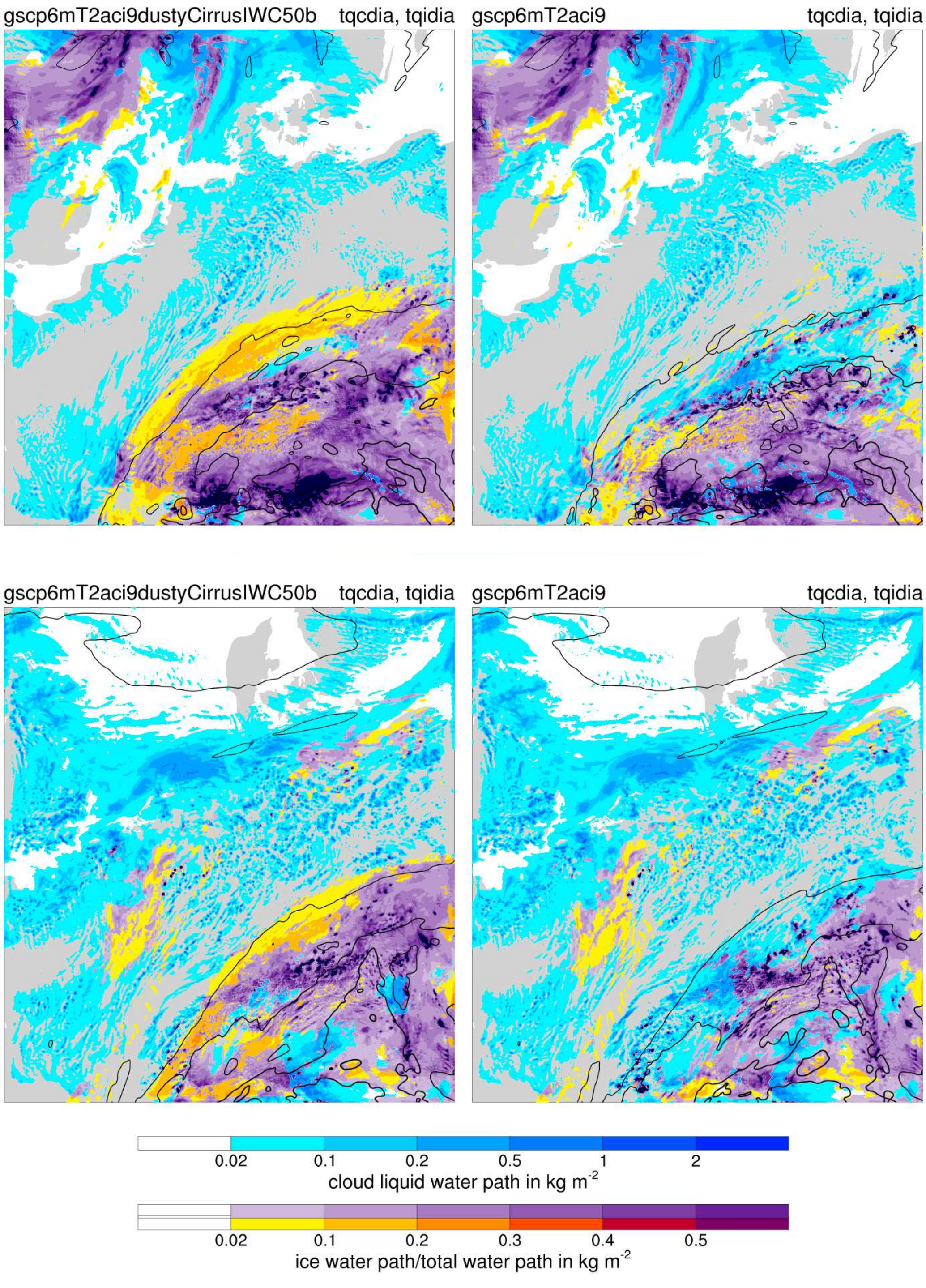

Figure S58. Cloud ice water path (orange-red), cloud water path (blue), and total cloud water path (magenta) for 6 May 2022 12 UTC and 7 May 2022 12 UTC. IWP is shown for column with only ice, LWP for columuns with liquid only, and TWP for column with mixed-phase or multi-layer clouds that contain ice and liquid. The IWP and TWP do include the sub-grid diagnostic contribution, e.g., from the dusty cirrus parameterization. Shown are the ACI (right) and the ACI-dusty (left) simulations of ICON-ART. Isolines are the mineral dust AOD from 0.1 to 0.5 with intervals of 0.1.

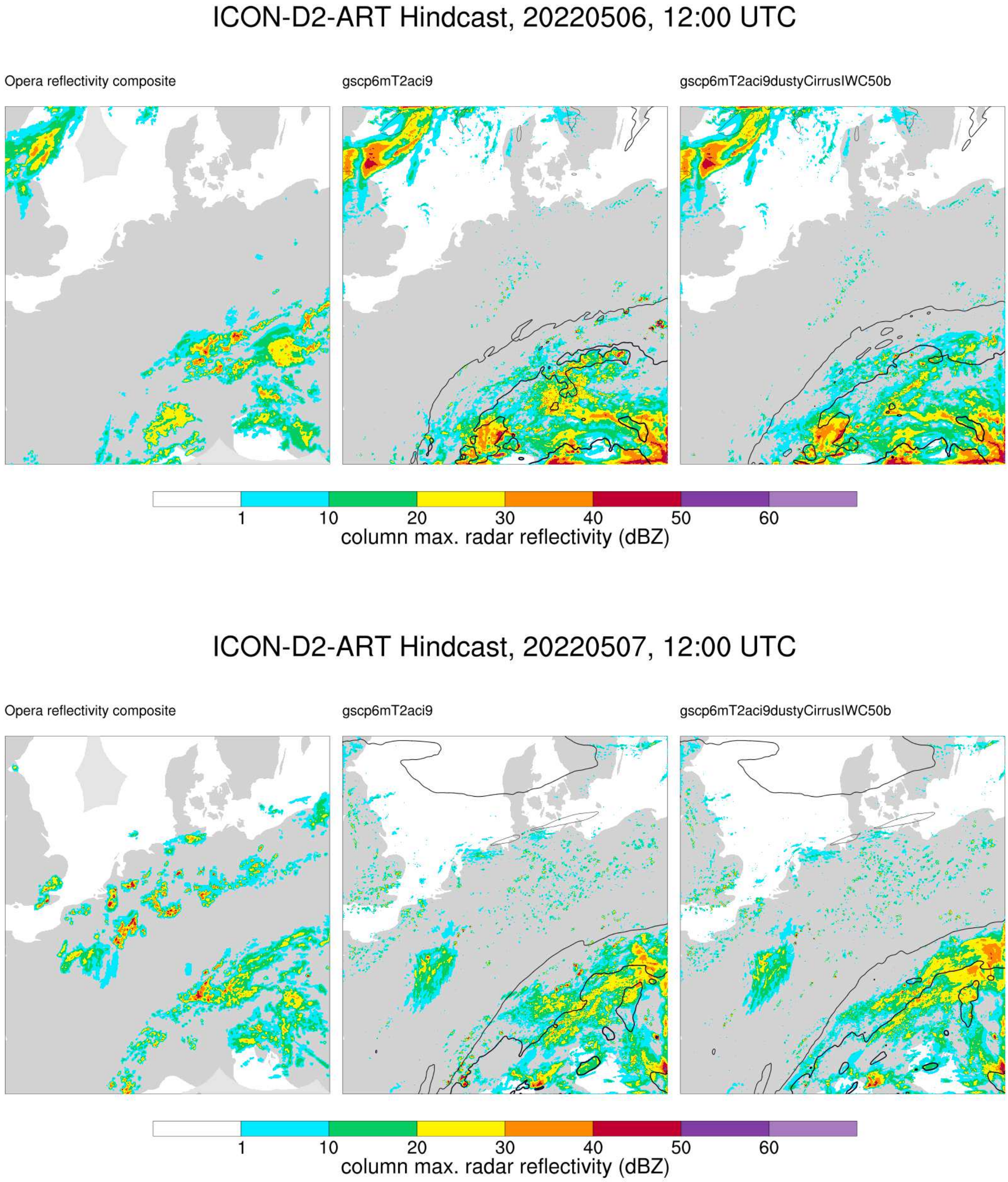

Figure S59. Column-maximum radar reflectivity factor in dBZ for 6 May 2022 12 UTC and 7 May 2022 12 UTC. Shown is the Opera composit (left), the ACI simulation (center), and the ACI-dusty simulation (right). Isolines are the mineral dust AOD at 0.1, 0.2, 0.3 and 0.5

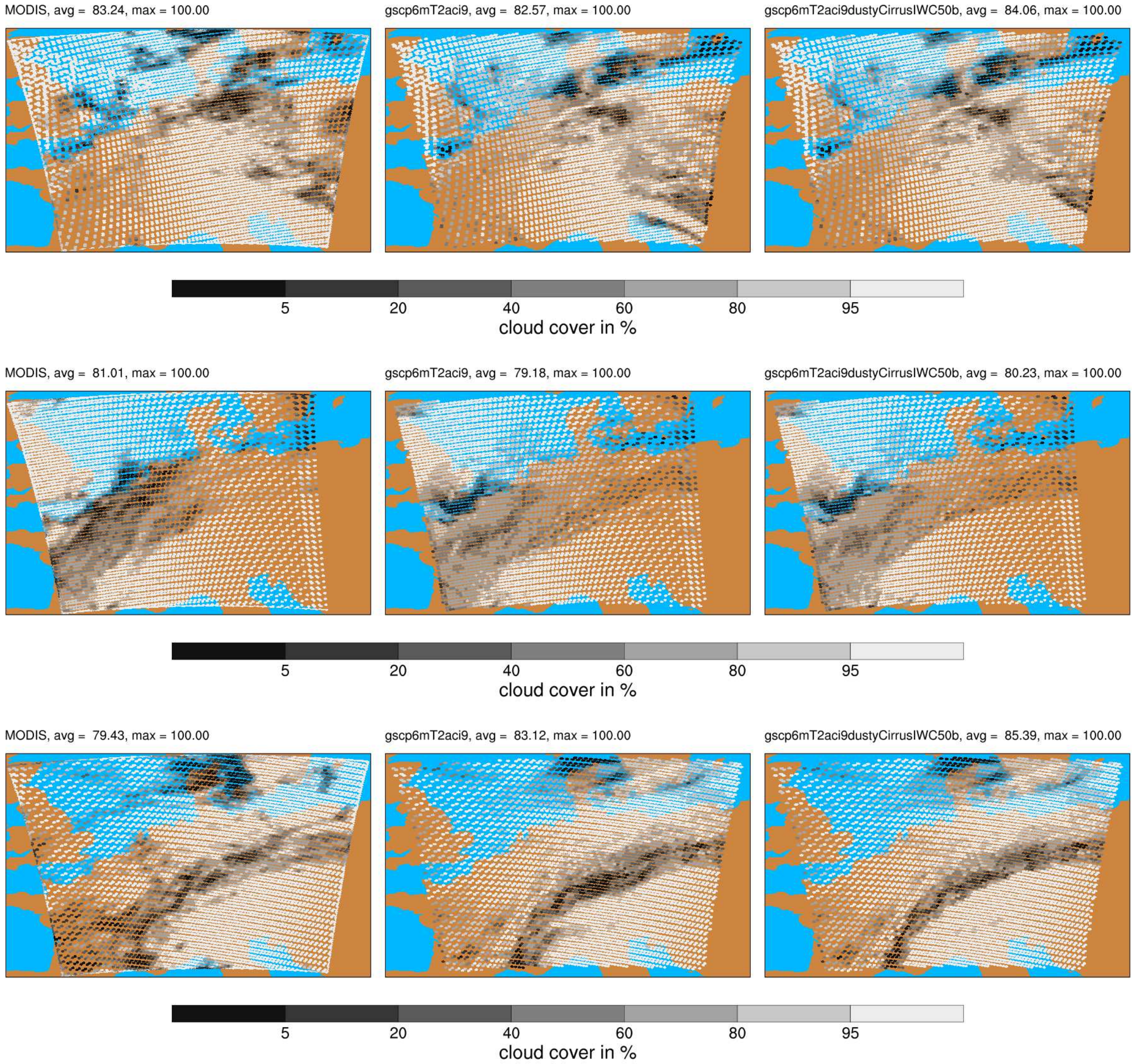

Figure S60. MODIS cloud cover vs ICON-ART for 5 May 2022 12:10 UTC, 6 May 2022 12:50 UTC, and 7 May 10:10 UTC

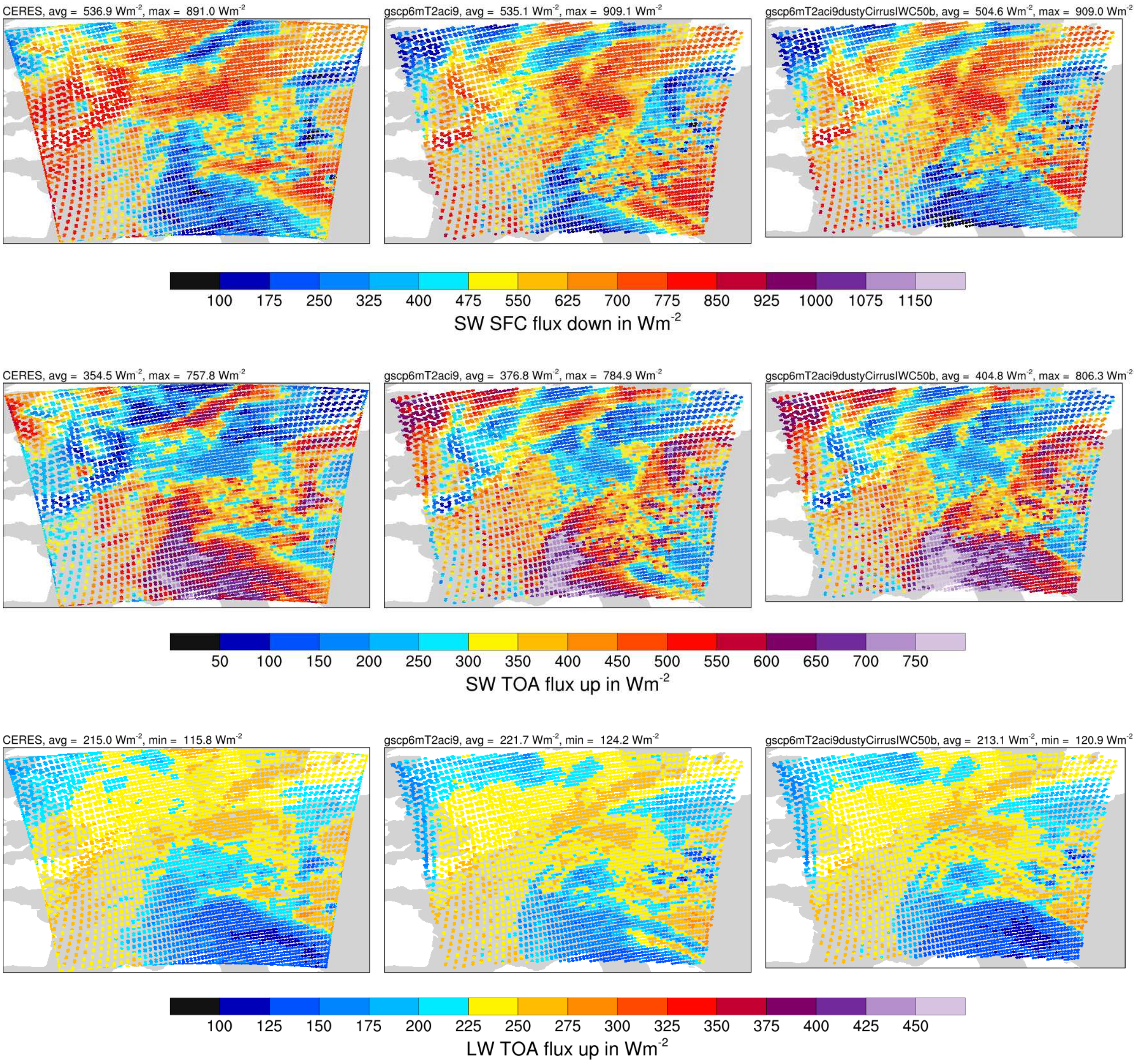

Figure S61. CERES SSF vs ICON-ART for 15 May 2022, 12:10 UTC.

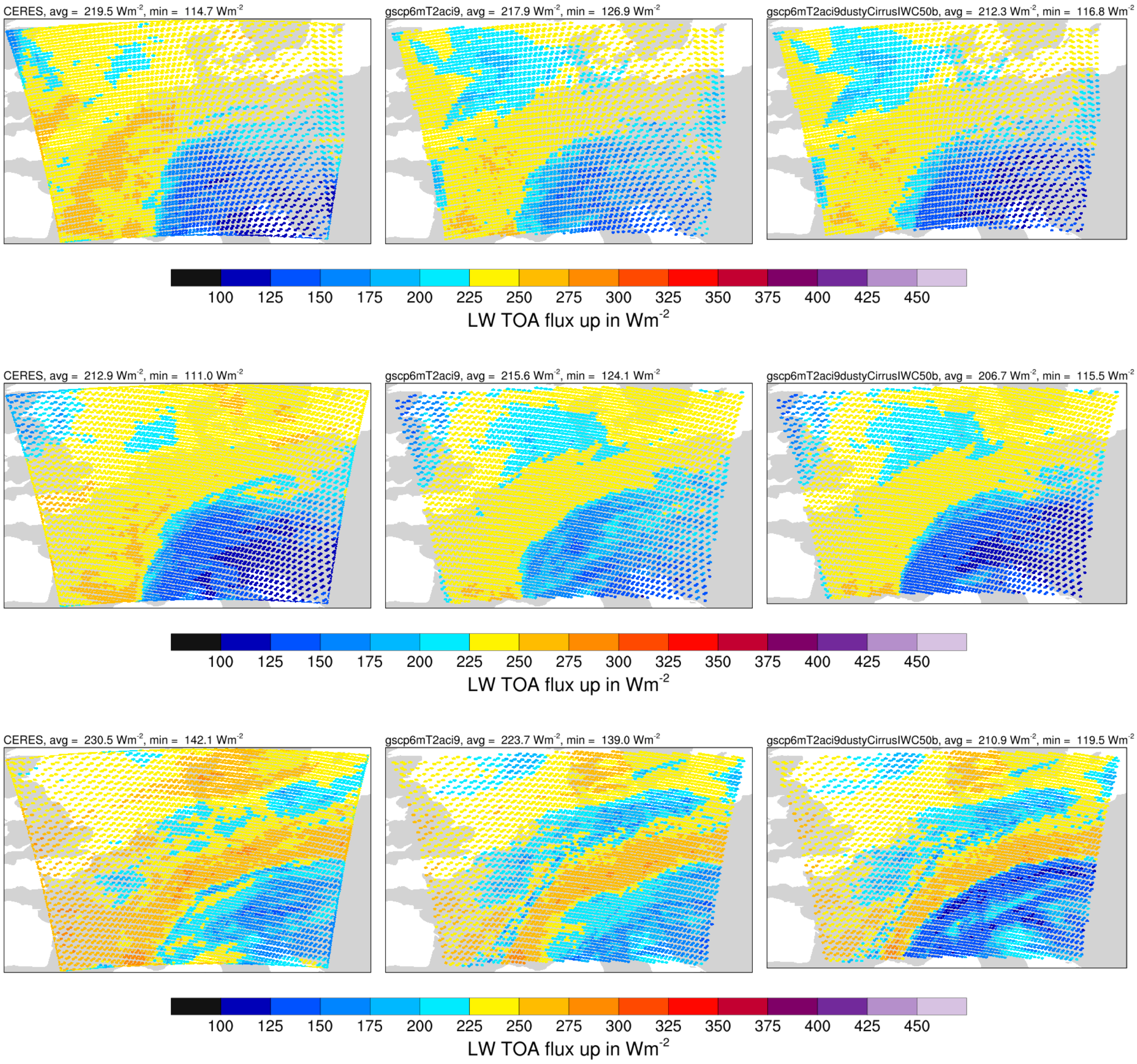

Figure S62. CERES SSF outgoing longwave radaition vs ICON-ART for 5 May 2022 21:35 UTC (top), 6 May 2022 01:45 UTC (middle), and 7 May 2022 10:10 UTC (bottom).

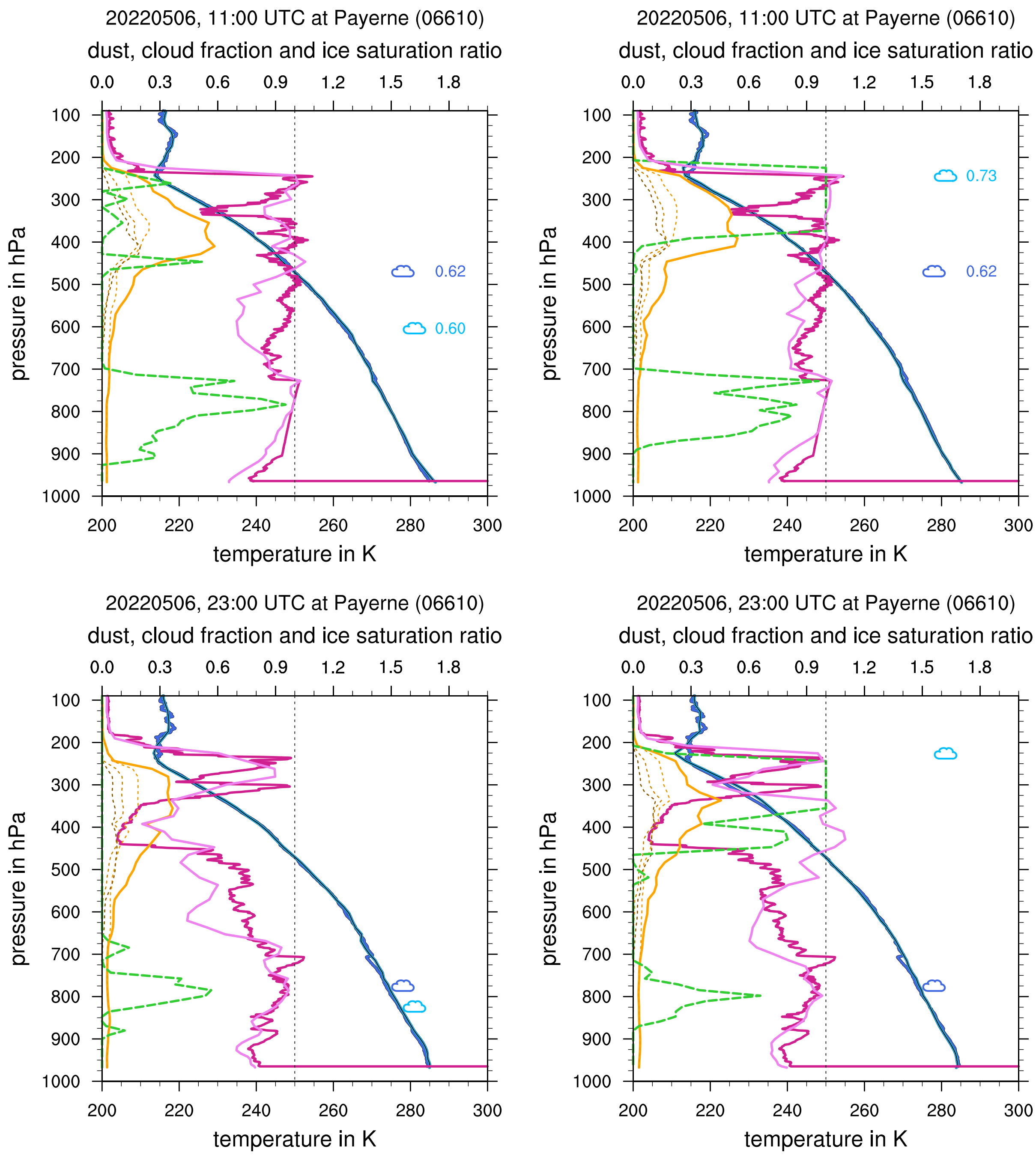

Figure S63. Vertical profiles from radiosonde measurements at Payerne (Switzerland) on 5 May 2022 11 UTC and on 6 May 2022 23 UTC and the corresponding ICON-ART profiles. Observed temperature (black), ICON-ART temperature (blue), observed saturation ratio for ice (dark pink), ICON-ART saturation ratio (lighter pink), normalized total dust concentration of ICON-ART (thick orange), dust modes (other orange and browns), and ICON-ART cloud fraction (green). Cloud symbols indicate the SEVIRI BT (dark blue) and ICON-ART RTTOV BT (light blue) at 10.8 μm for this grid point. Numbers next to the cloud symbol give the visible reflectance (only daytime). Shown are ACI (left) and ACI-dusty (right).

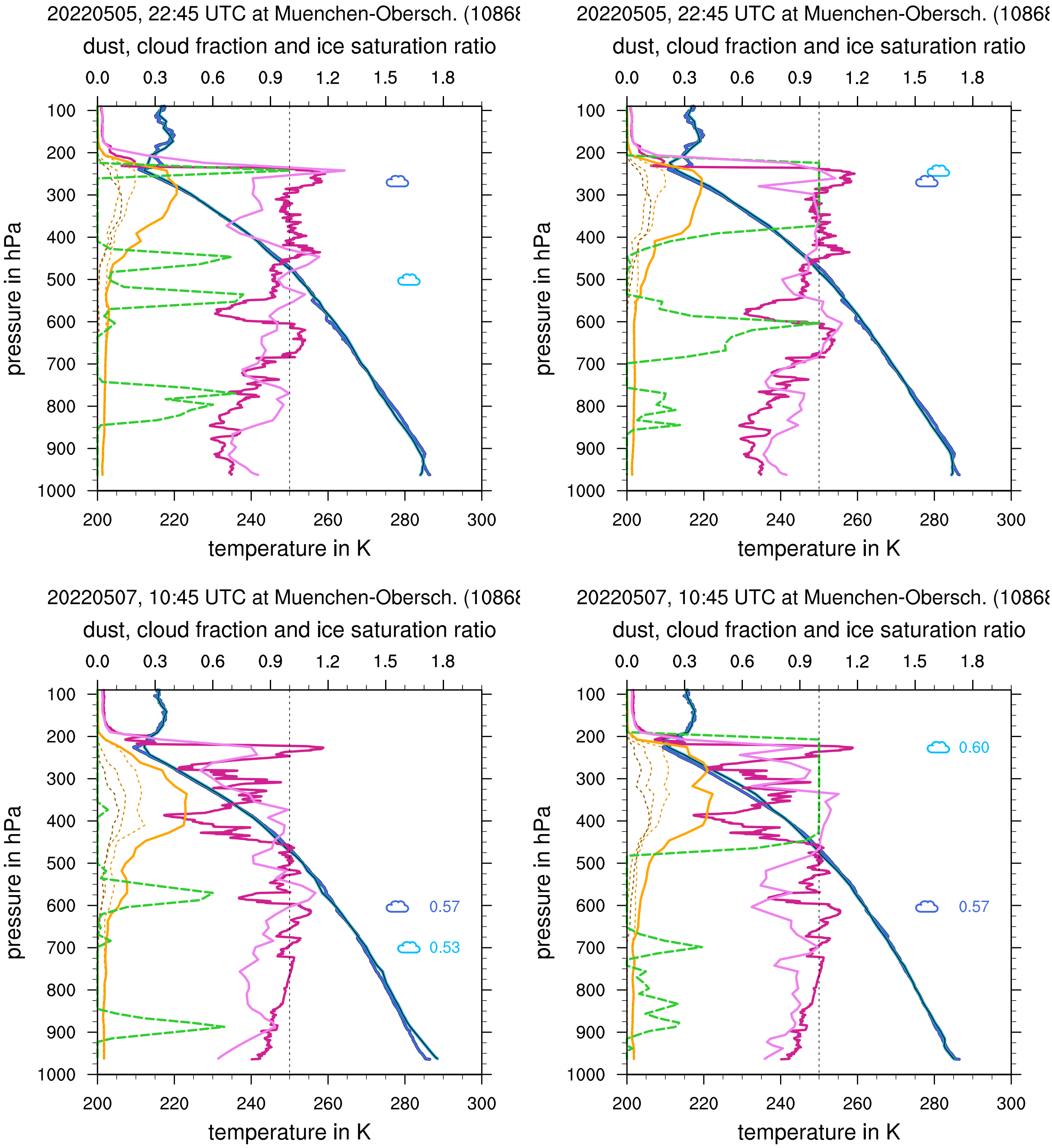

Figure S64. Vertical profiles from radiosonde measurements at Munich (Germany) on 5 May 2022 23 UTC and 7 May 2022 11 UTC the corresponding ICON-ART profiles. Observed temperature (black), ICON-ART temperature (blue), observed saturation ratio for ice (dark pink), ICON-ART saturation ratio (lighter pink), normalized total dust concentration of ICON-ART (thick orange), dust modes (other orange and browns), and ICON-ART cloud fraction (green). Cloud symbols indicate the SEVIRI BT (dark blue) and ICON-ART RTTOV BT (light blue) at 10.8 μm for this grid point. Numbers next to the cloud symbol give the visible reflectance (only daytime). Shown are ACI (left) and ACI-dusty (right).

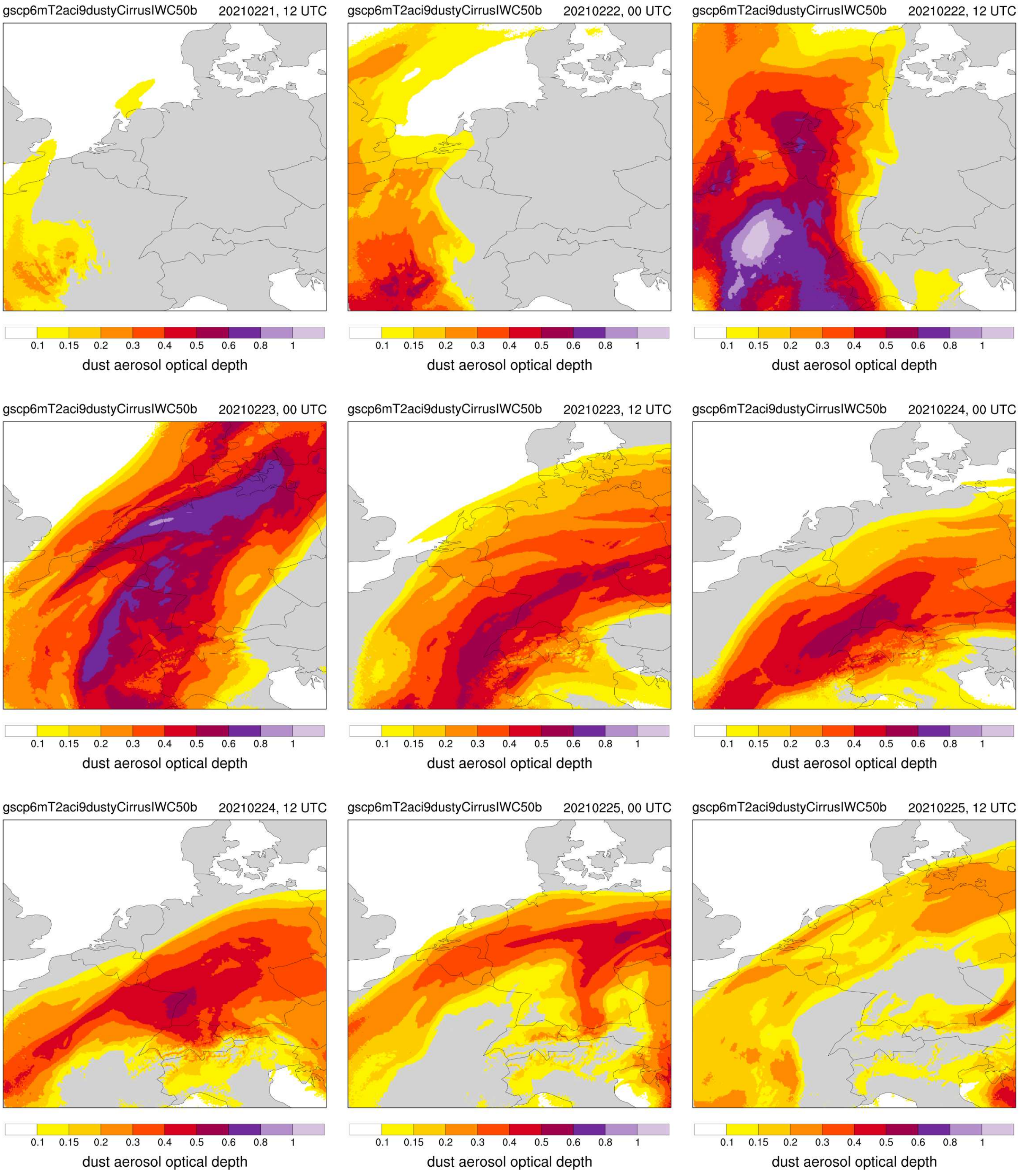

Figure S65. ICON-ART mineral dust AOD for 21-25 Feb 2022.

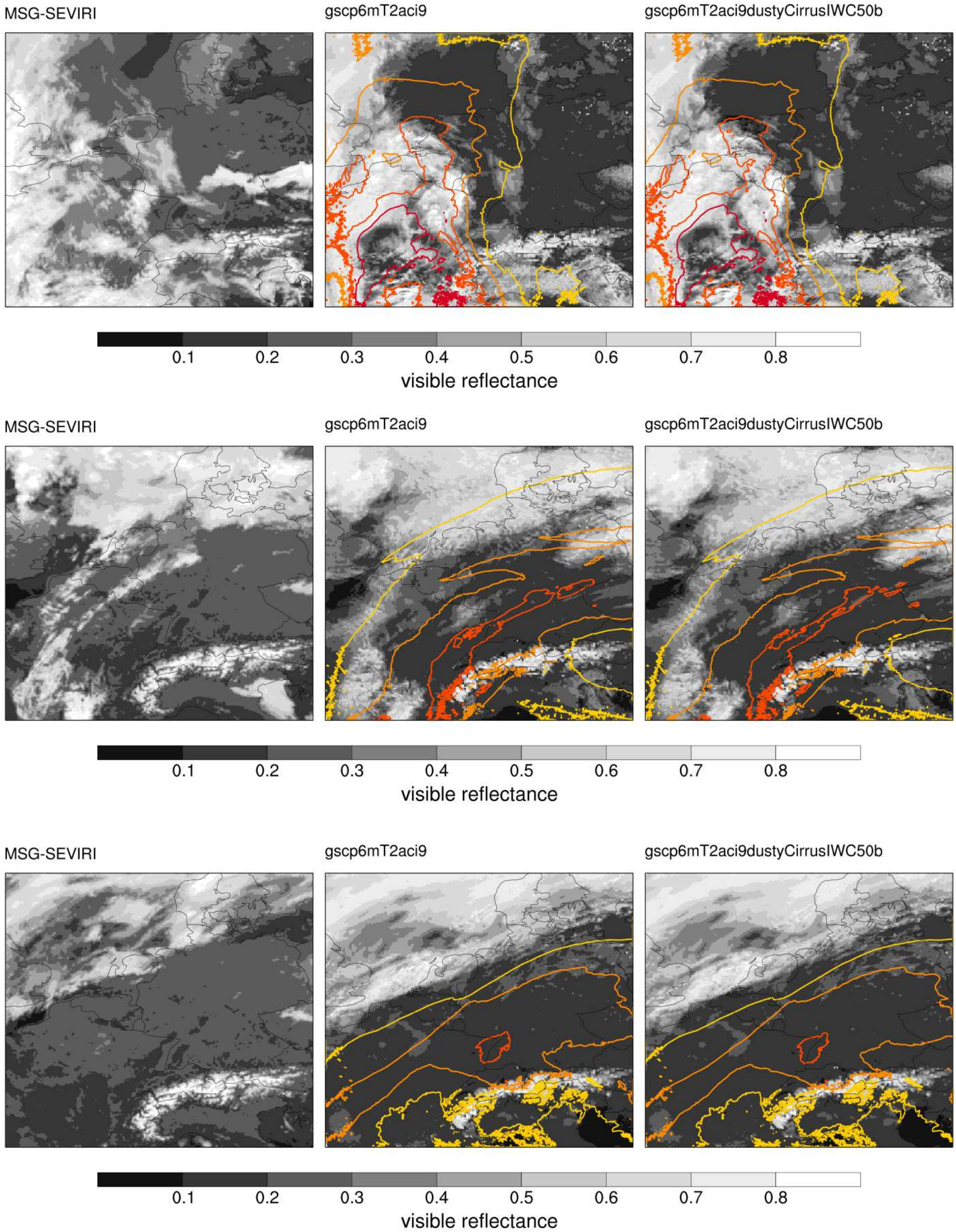

Figure S66. MSG SEVIRI visible reflectance vs ICON-ART for 22-24 Feb 12 UTC (top to bottom). For ICON-ART the mineral dust AOD is shown with isolines from 0.1 to 0.5 (yellow-orange-red) with intervals of 0.2.

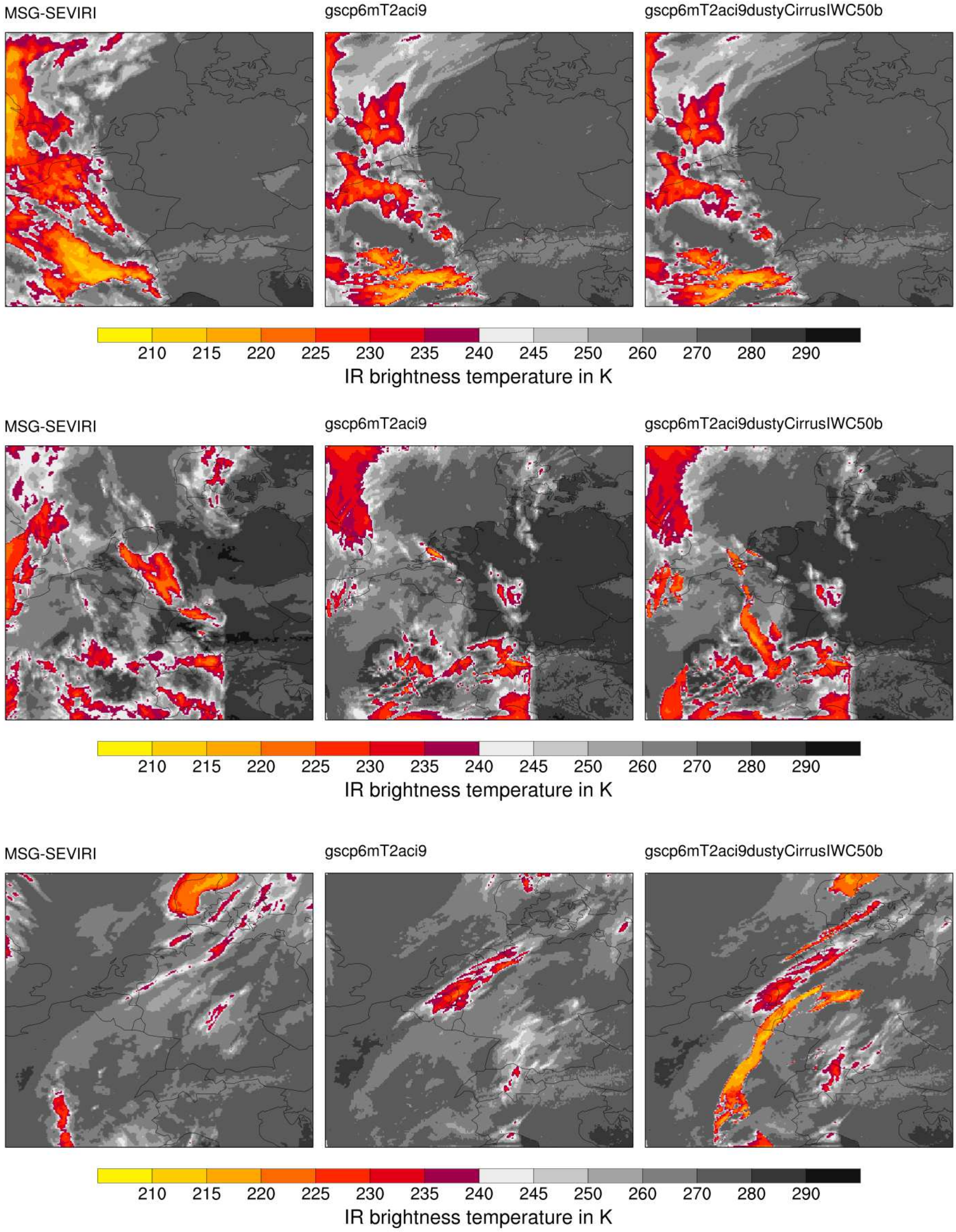

Figure S67. MSG SEVIRI infrared at 10.8 μm vs ICON-ART for 22 Feb 2022 00 UTC, 22 Feb 12 UTC and 23 Feb 00 UTC (top to bottom).

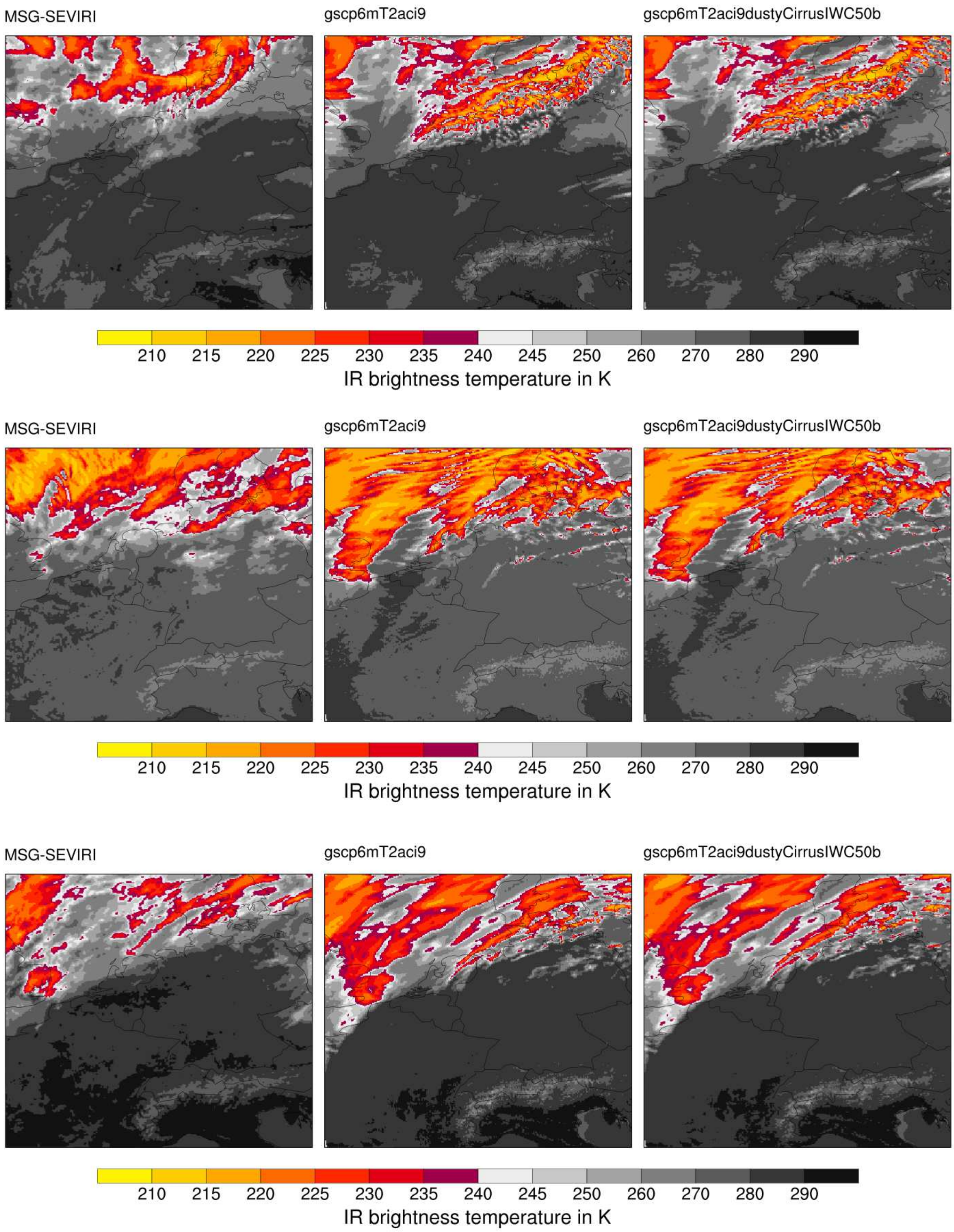

Figure S68. MSG SEVIRI infrared at 10.8 μm vs ICON-ART for 23 Feb 12 UTC, 24 Feb 00 UTC and 24 Feb 12 UTC 2022 (top to bottom).

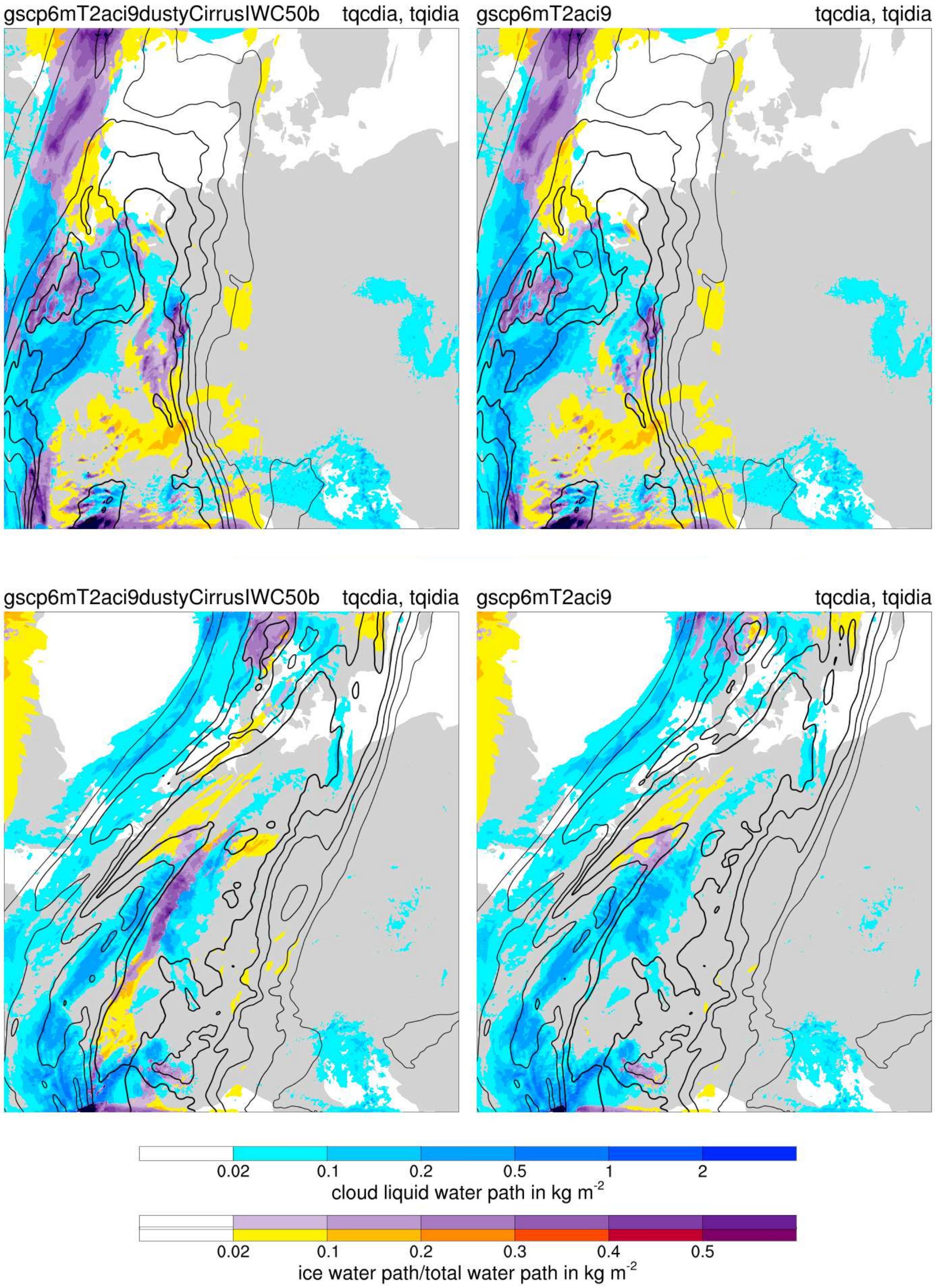

Figure S69. Ice water path (orange-red), cloud water path (blue), and total water path (magenta) for 22 Feb 2021 12 UTC and 23 Feb 2021 00 UTC. IWP is shown for column with only ice, LWP for columuns with liquid only, and TWP for column with mixed-phase or multi-layer clouds that contain ice and liquid. The IWP and TWP do include the sub-grid diagnostic contribution, e.g., from the dusty cirrus parameterization. Shown are the ACI (right) and the ACI-dusty (left) simulations of ICON-ART. Isolines are the mineral dust AOD with intervals of 0.1.

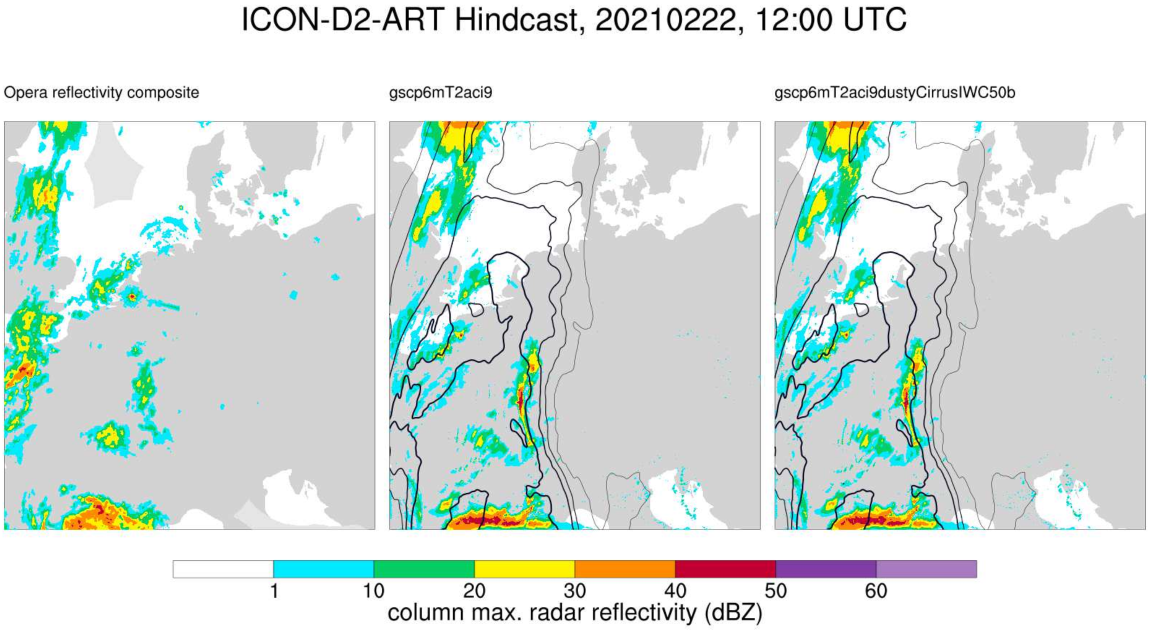

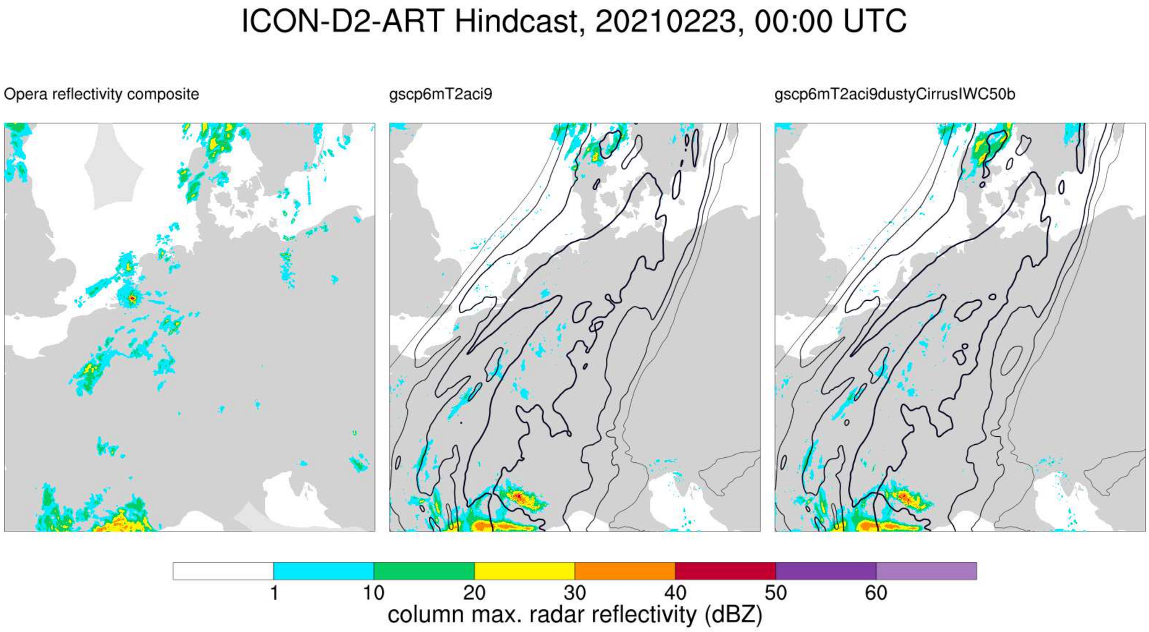

Figure S70. Column-maximum radar reflectivity factor in dBZ for 22 Feb 2021 12 UTC and 23 Feb 2021 12 UTC. Shown is the Opera composit (left), the ACI simulation (center), and the ACI-dusty simulation (right). Isolines are the mineral dust AOD at 0.1, 0.2, 0.3 and 0.5

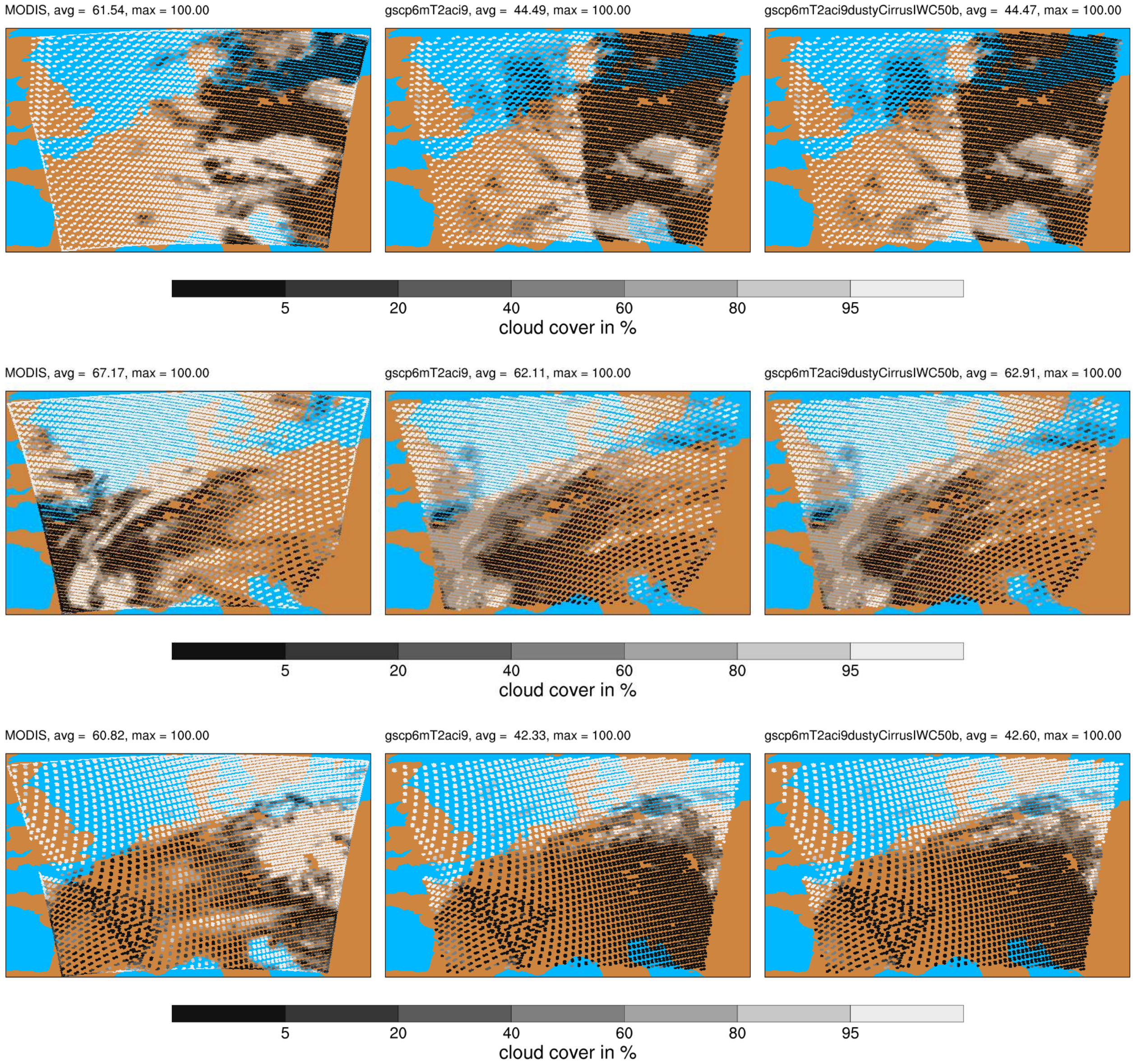

Figure S71. MODIS cloud cover vs ICON-ART for 22 Feb 2021 10:10 UTC, 23 Feb 2021 10:56 UTC, and 24 Feb 11:47 UTC

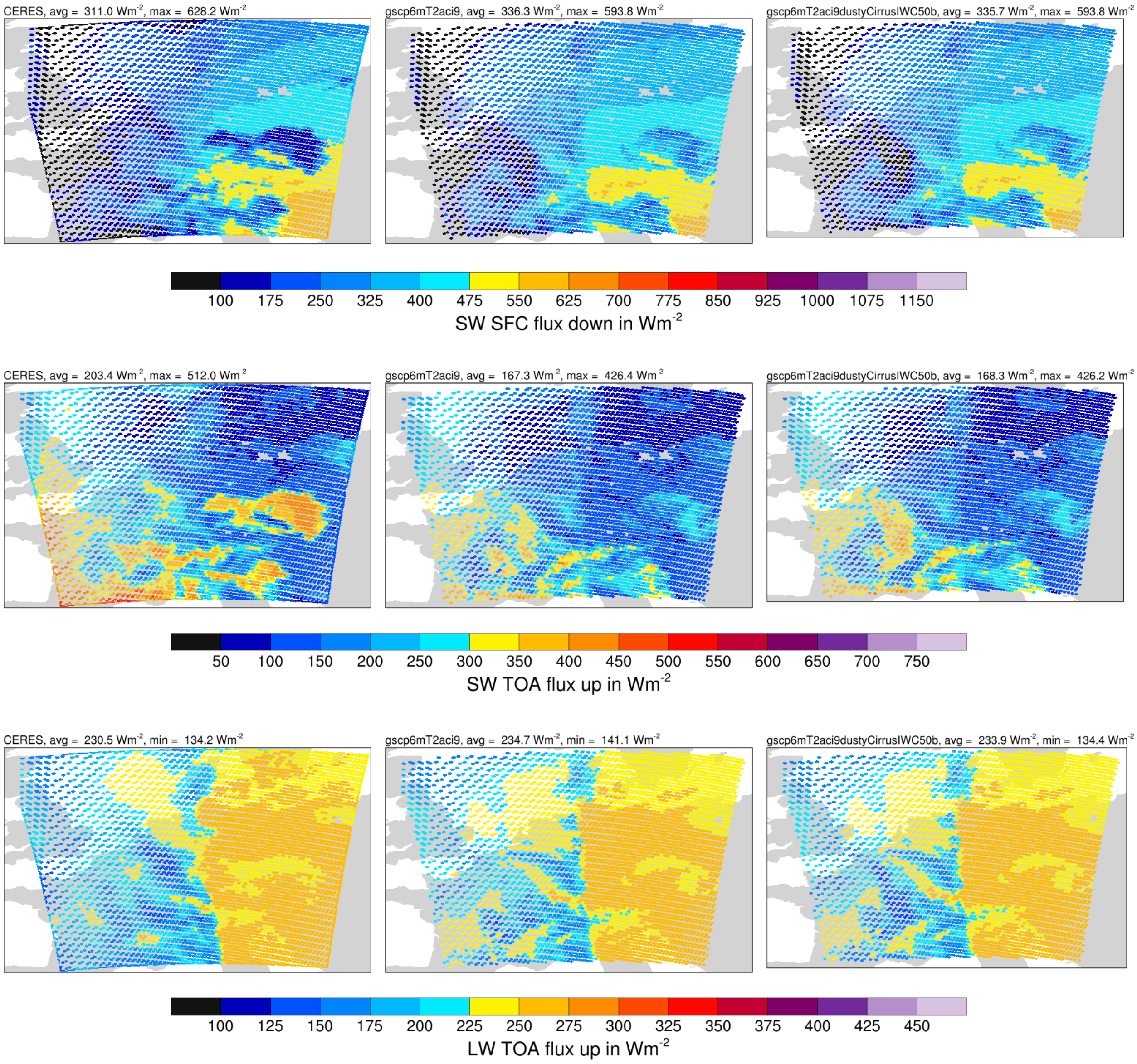

Figure S72. CERES SSF vs ICON-ART for 22 Feb 2021, 10:10 UTC.

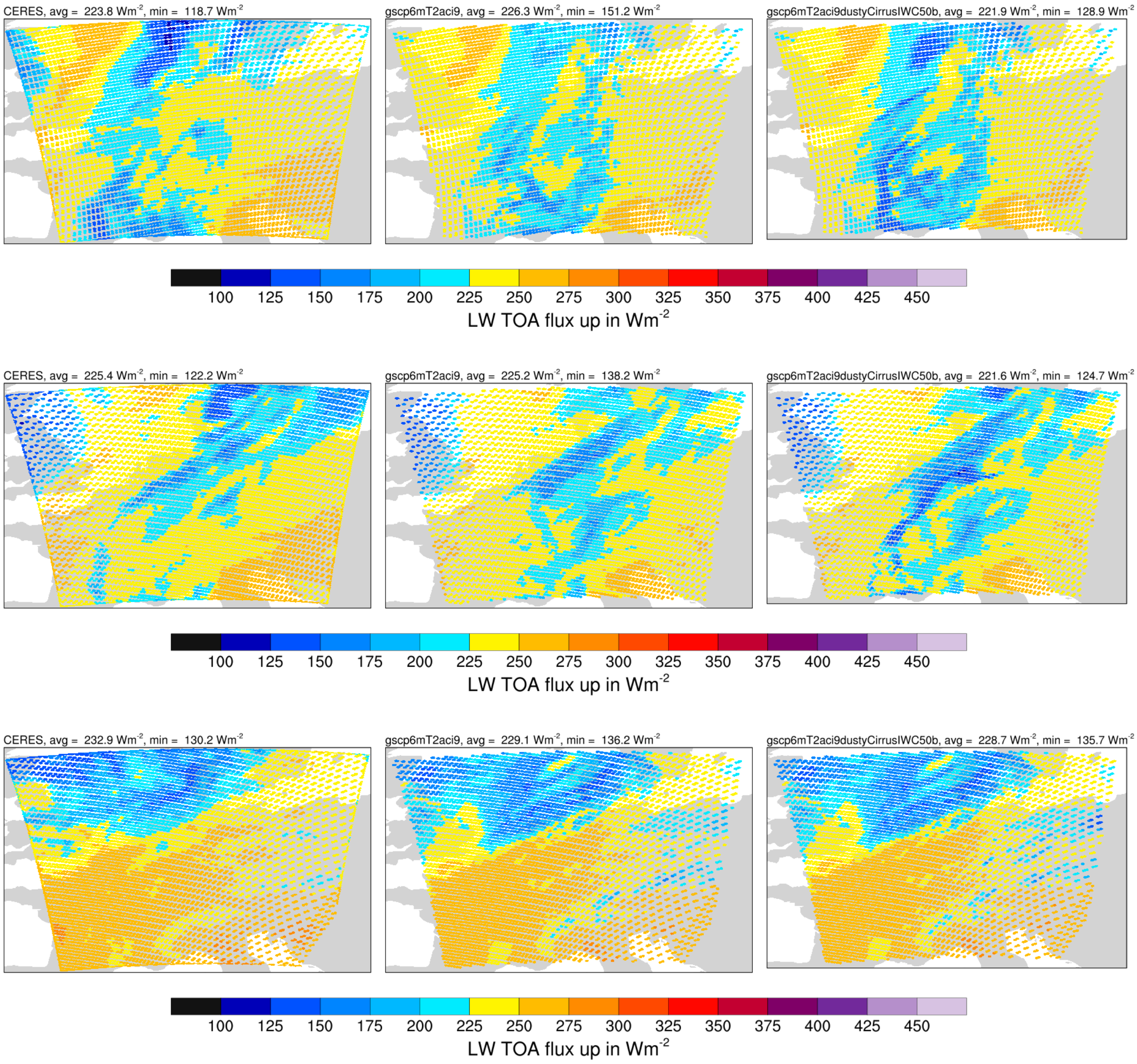

Figure S73. CERES SSF outgoing longwave radiation vs ICON-ART for 22 Feb 2021 21:47 UTC (top), 23 Feb 2021 01:30 UTC (middle), and 23 Feb 2021 10:55 UTC (bottom).

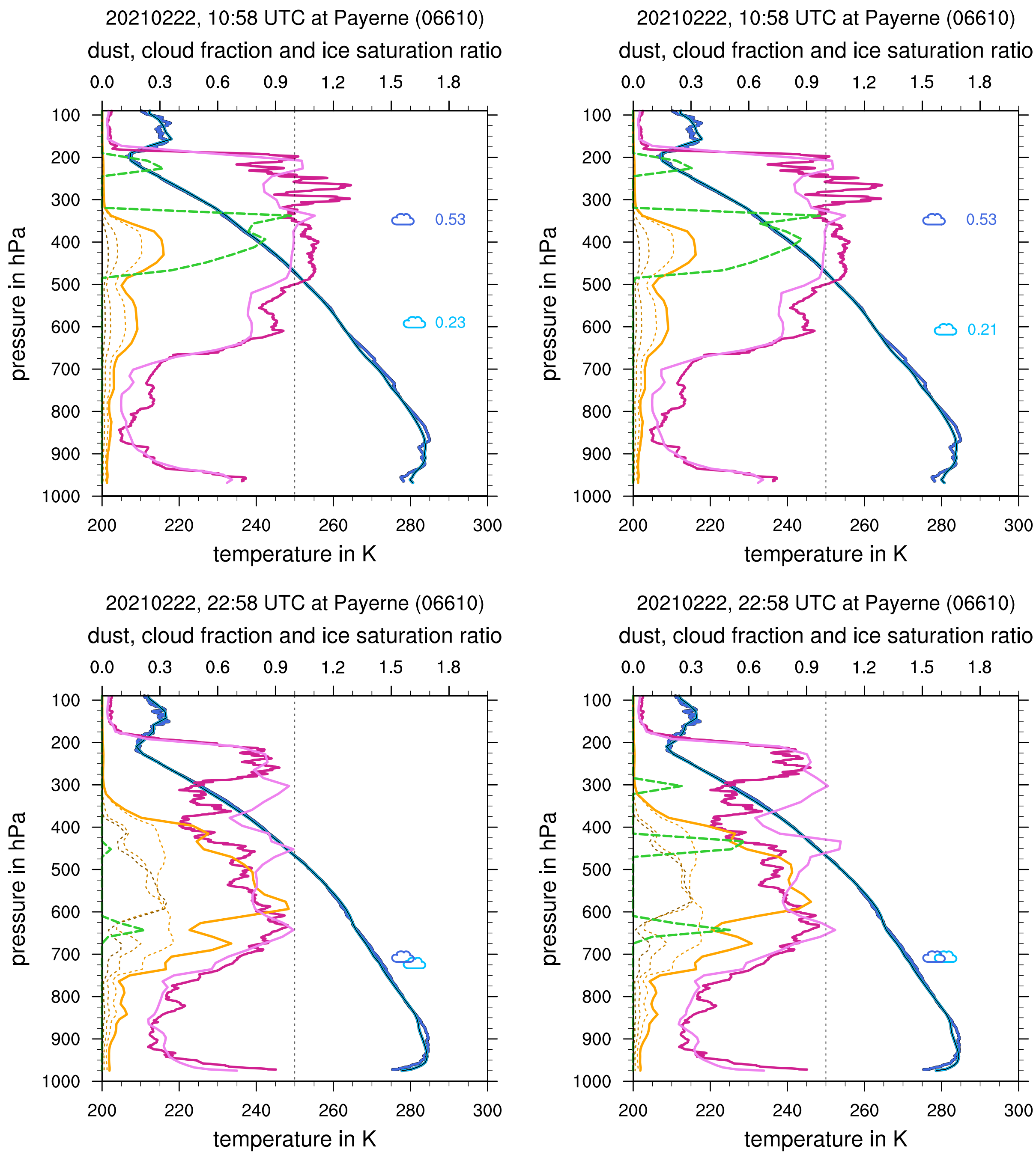

Figure S74. Vertical profiles from radiosonde measurements at Payerne (Switzerland) on 22 Feb 2021 11 UTC and 23 UTC and the corresponding ICON-ART profiles. Observed temperature (black), ICON-ART temperature (blue), observed saturation ratio for ice (dark pink), ICON-ART saturation ratio (lighter pink), normalized total dust concentration of ICON-ART (thick orange), dust modes (other orange and browns), and ICON-ART cloud fraction (green). Cloud symbols indicate the SEVIRI BT (dark blue) and ICON-ART RTTOV BT (light blue) at 10.8 μm for this grid point. Numbers next to the cloud symbol give the visible reflectance (only daytime). Shown are ACI (left) and ACI-dusty (right).

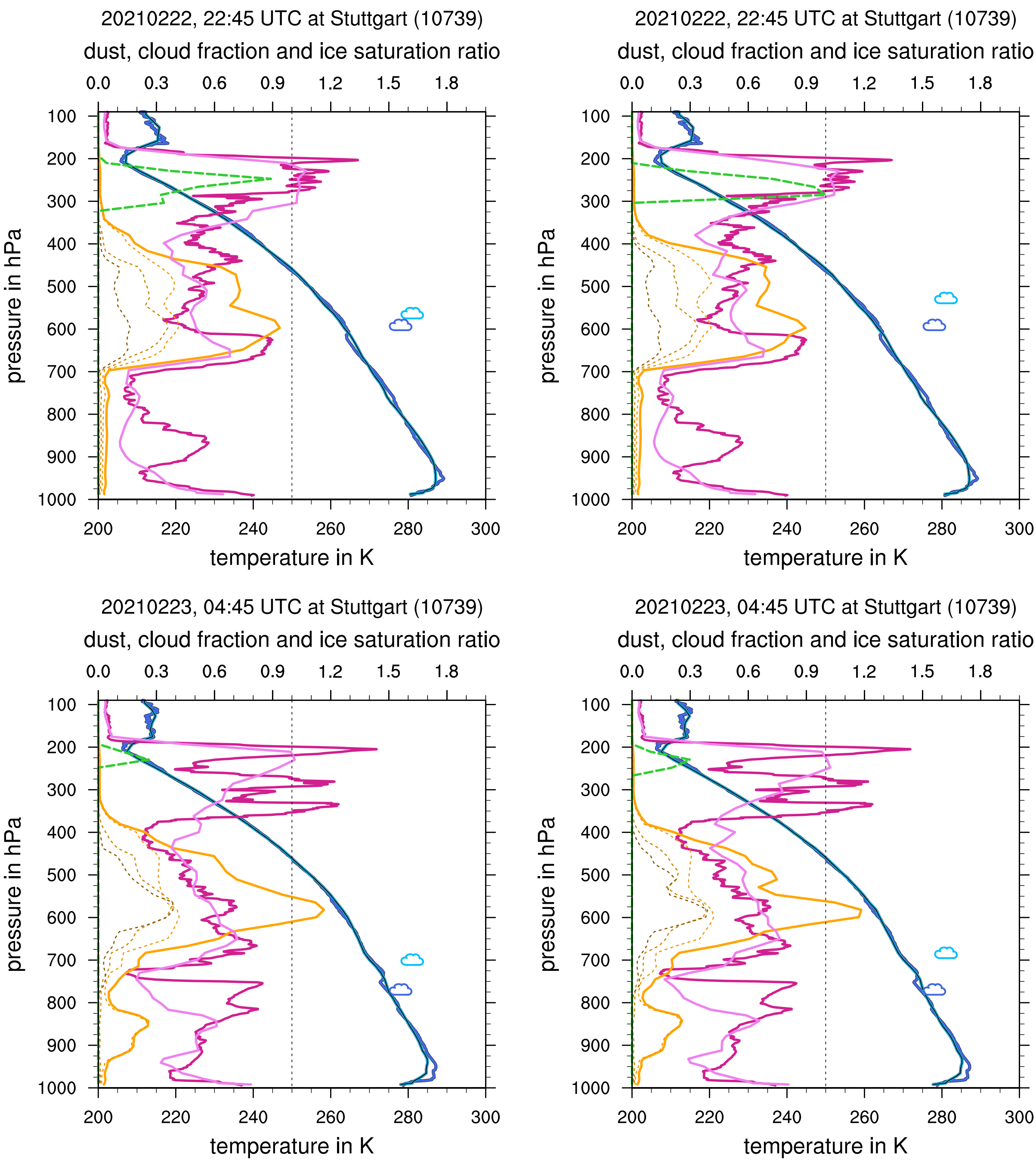

Figure S75. Vertical profiles from radiosonde measurements at Stuttgart (Germany) on 22 Feb 2021 11 UTC and 23 UTC and the corresponding ICON-ART profiles. Shown are ACI (left) and ACI-dusty (right).

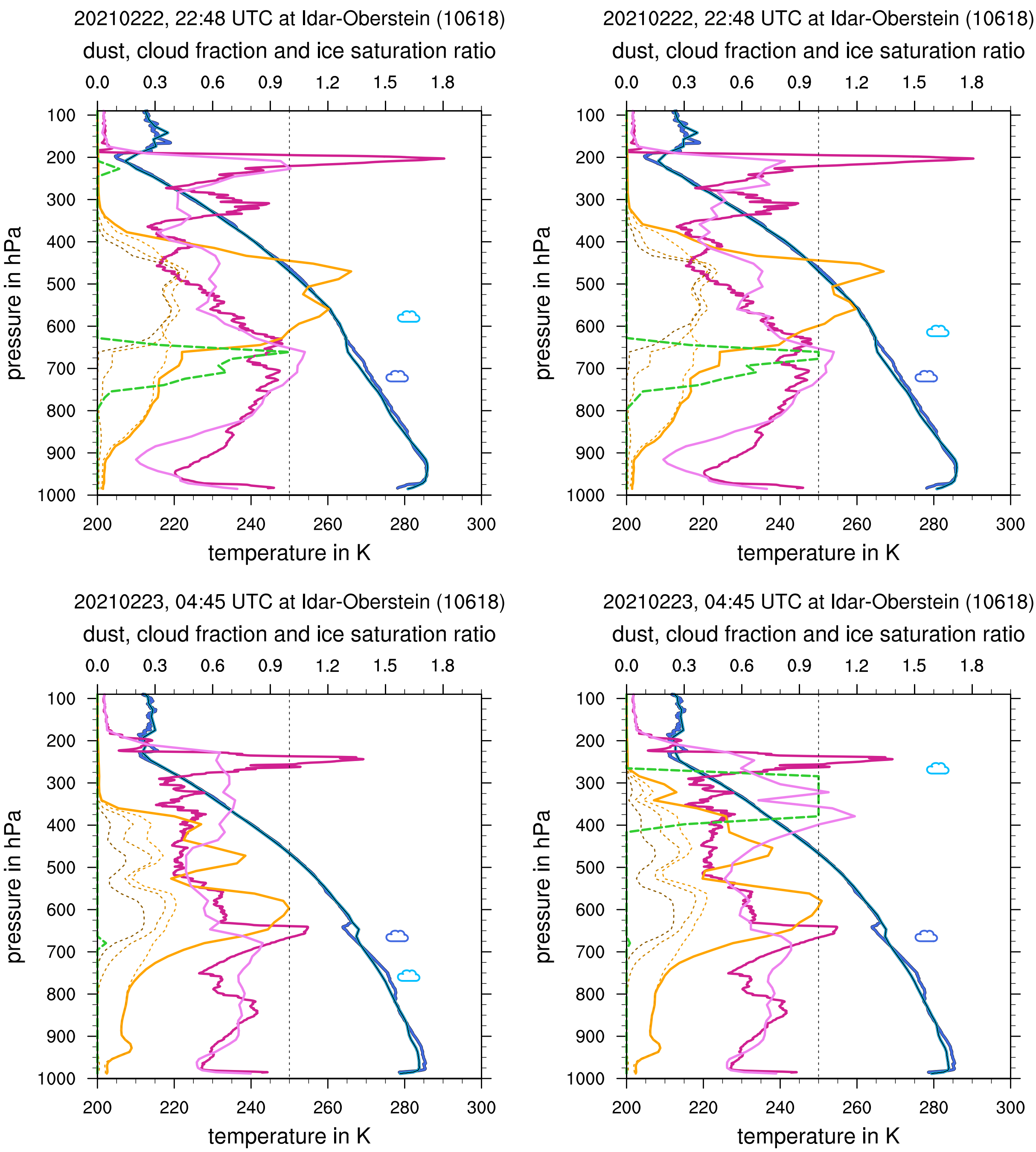

Figure S76. Vertical profiles from radiosonde measurements at Idar-Oberstein (Germany) on 22 Feb 2021 23 UTC and 23 Feb 5 UTC and the corresponding ICON-ART profiles. Shown are ACI (left) and ACI-dusty (right).

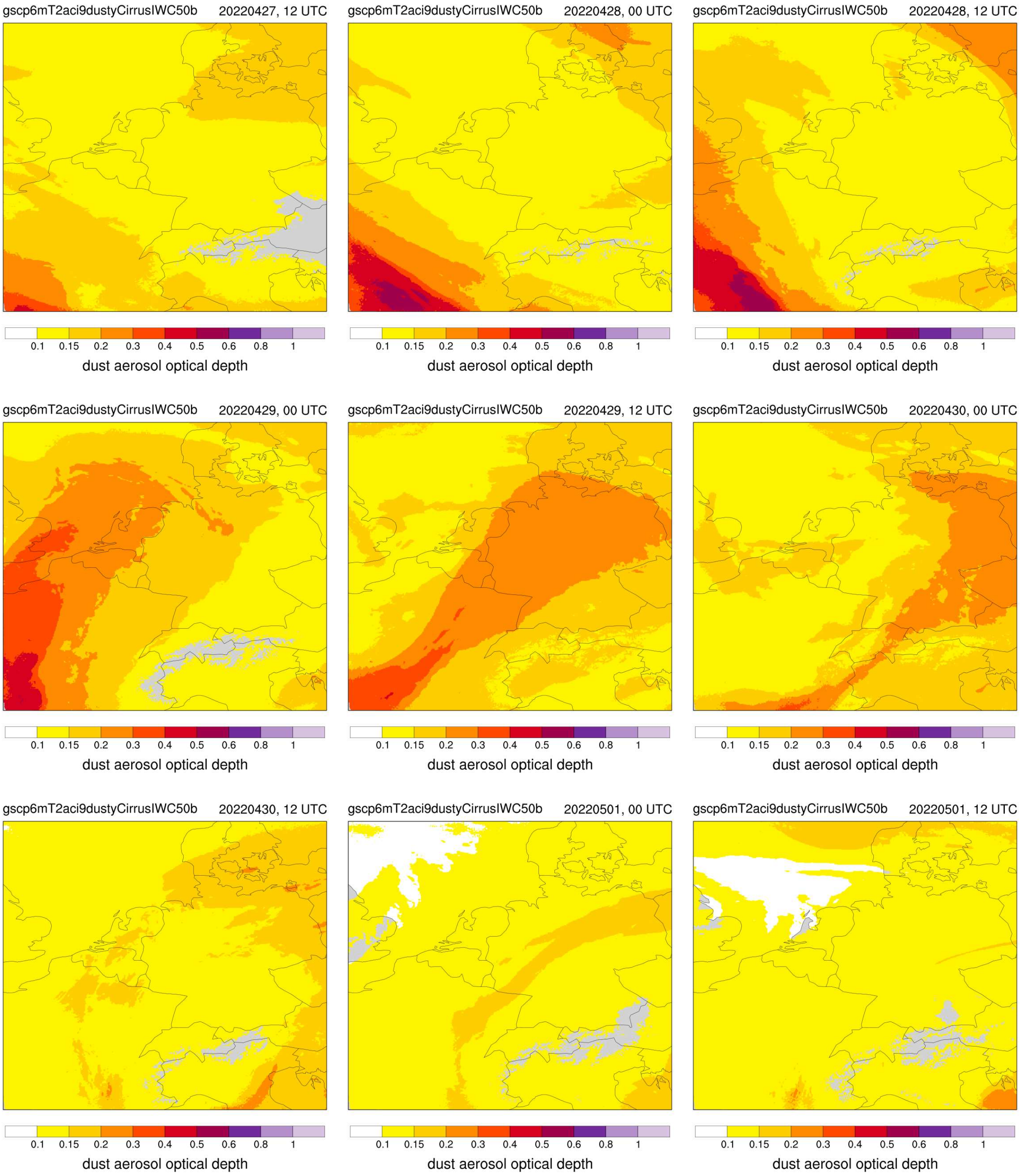

Figure S77. ICON-ART mineral dust AOD for 27-19 April 2022.

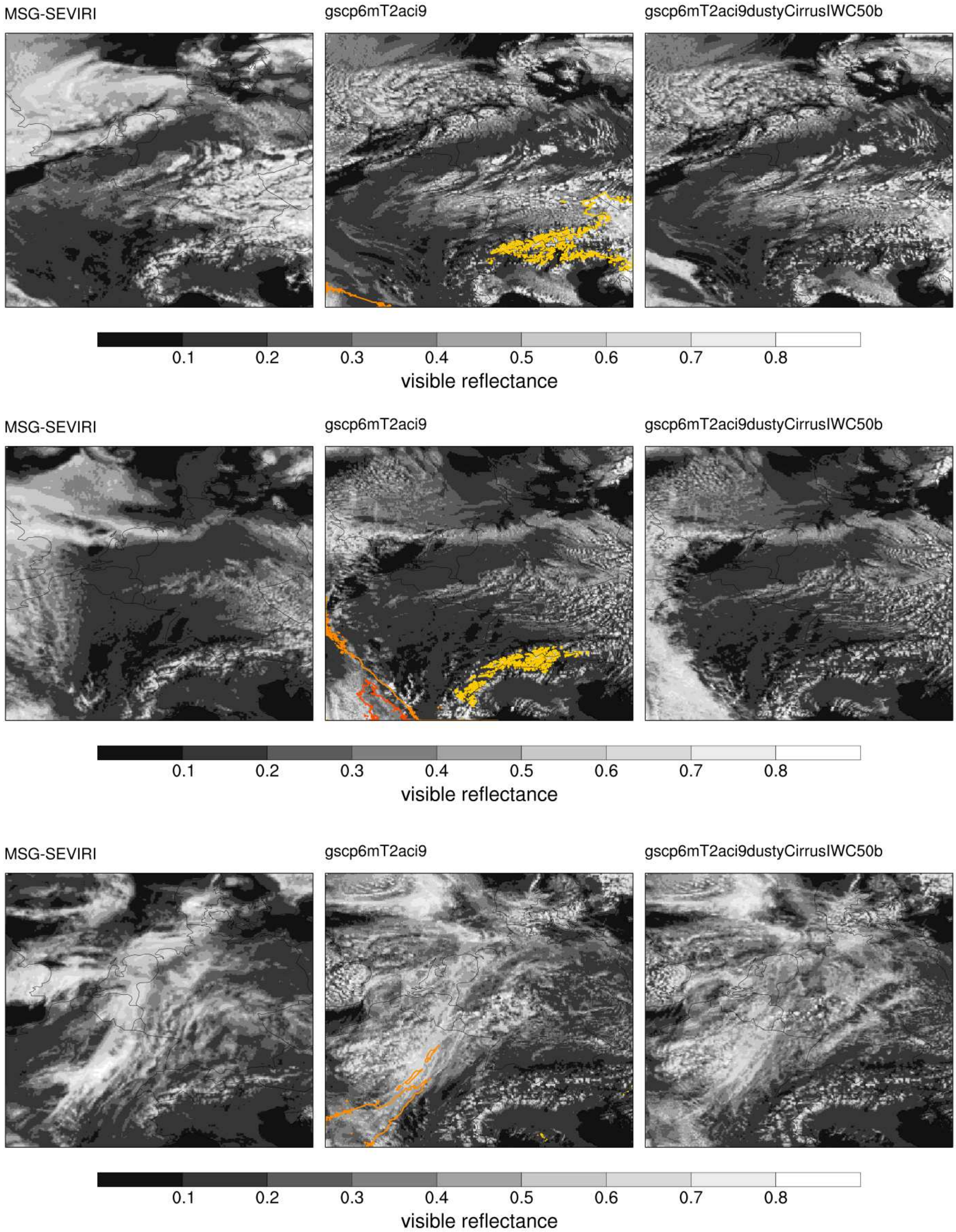

Figure S78. MSG SEVIRI visible reflectance vs ICON-ART for or 27 April 2022 12 UTC, 28 April 12 UTC and 29 April 12 UTC (top to bottom). For ICON-ART the mineral dust AOD is shown with isolines from 0.1 to 0.7 (yellow-orange-red) with intervals of 0.2.

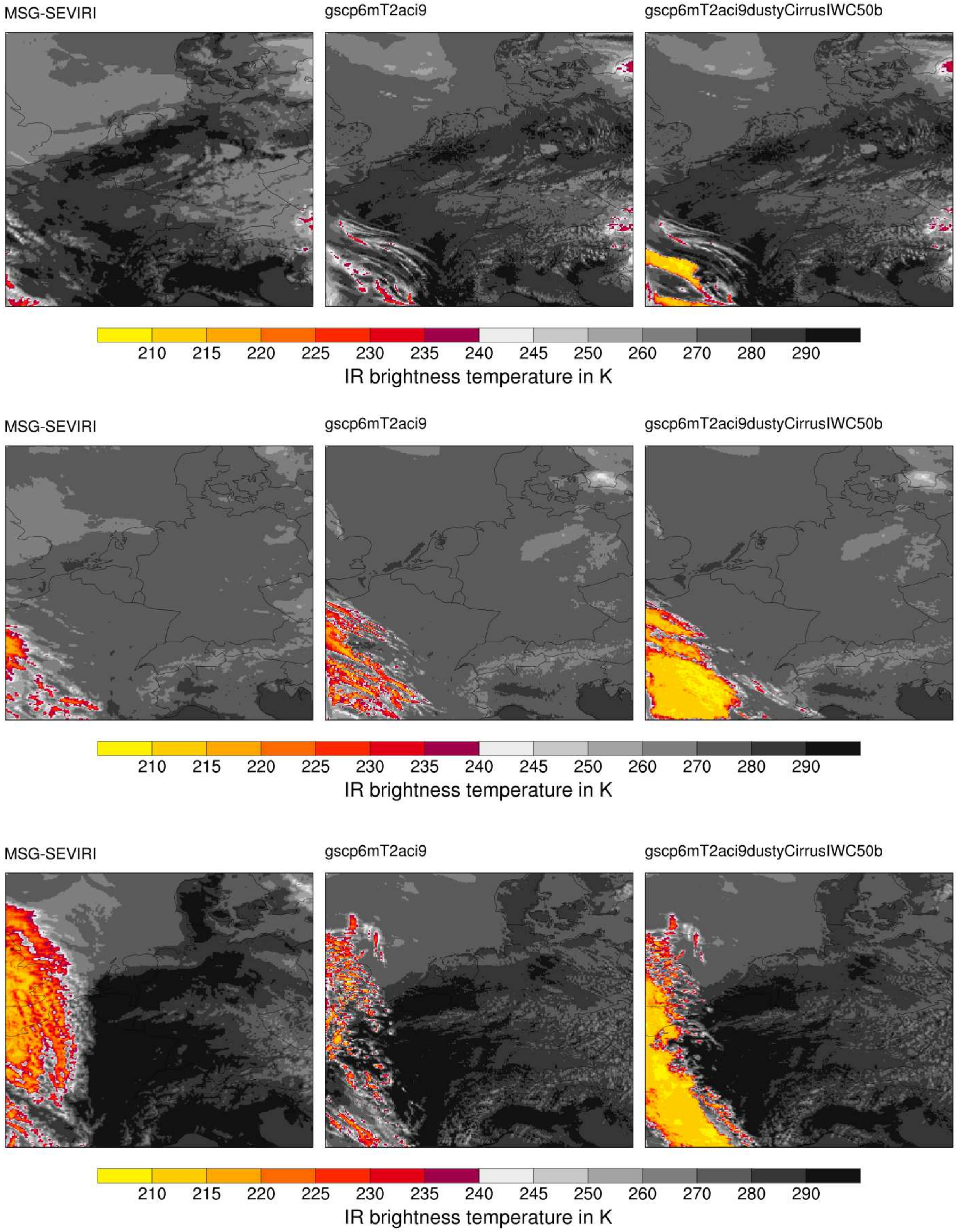

Figure S79. MSG SEVIRI infrared at 10.8 μm vs ICON-ART for 27 April 2022 12 UTC, 28 April 00 UTC and 28 April 12 UTC (top to bottom).

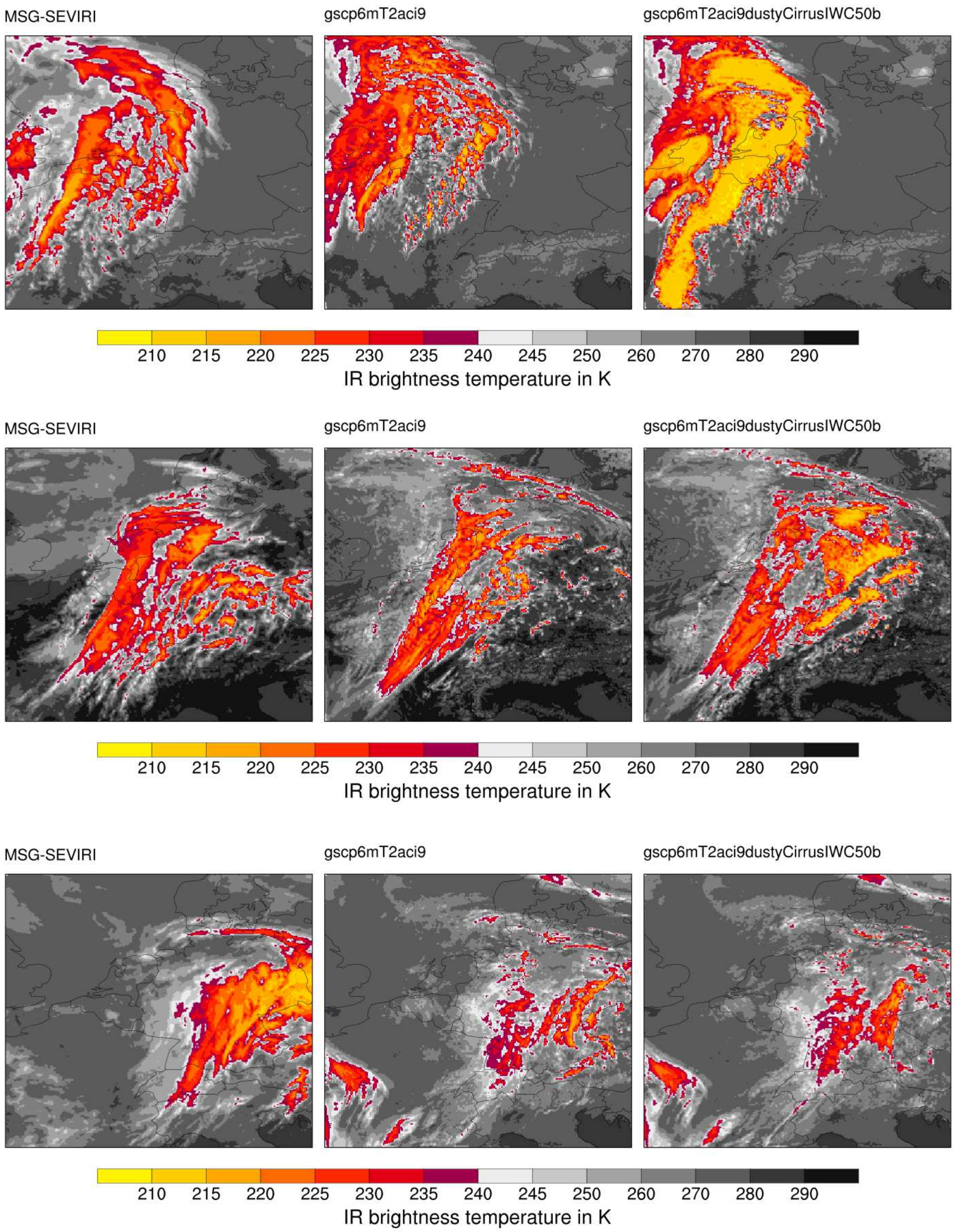

Figure S80. MSG SEVIRI infrared at 10.8 μm vs ICON-ART for 29 April 2022 00 UTC, 29 April 12 UTC and 30 April 00 UTC (top to bottom).

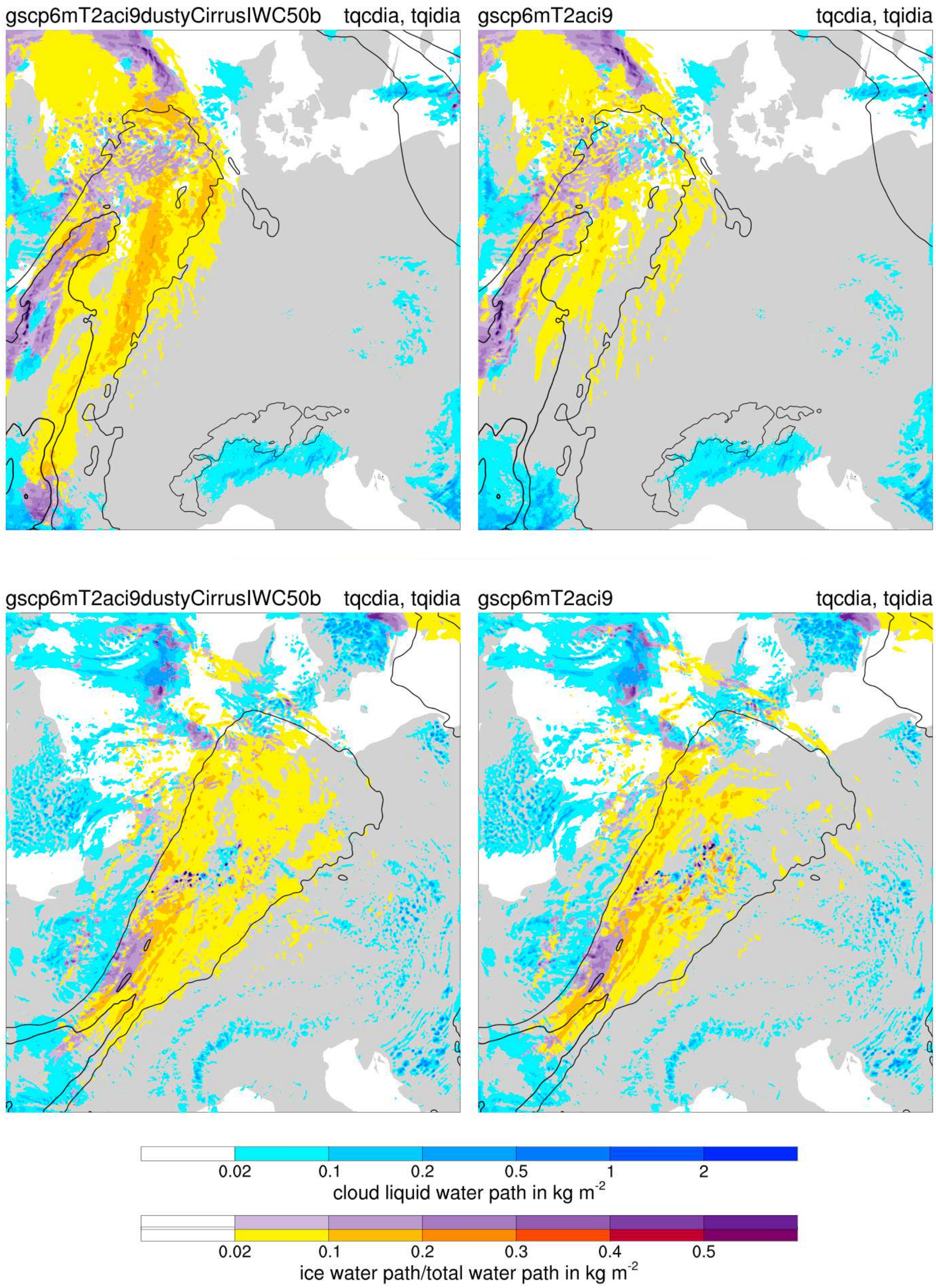

Figure S81. Ice water path (orange-red), cloud water path (blue), and total water path (magenta) for 29 April 2022 00 UTC and 29 April 2022 12 UTC. IWP is shown for column with only ice, LWP for columuns with liquid only, and TWP for column with mixed-phase or multi-layer clouds that contain ice and liquid. The IWP and TWP do include the sub-grid diagnostic contribution, e.g., from the dusty cirrus parameterization. Shown are the ACI (right) and the ACI-dusty (left) simulations of ICON-ART. Isolines are the mineral dust AOD from 0.1 to 0.5 with intervals of 0.1.

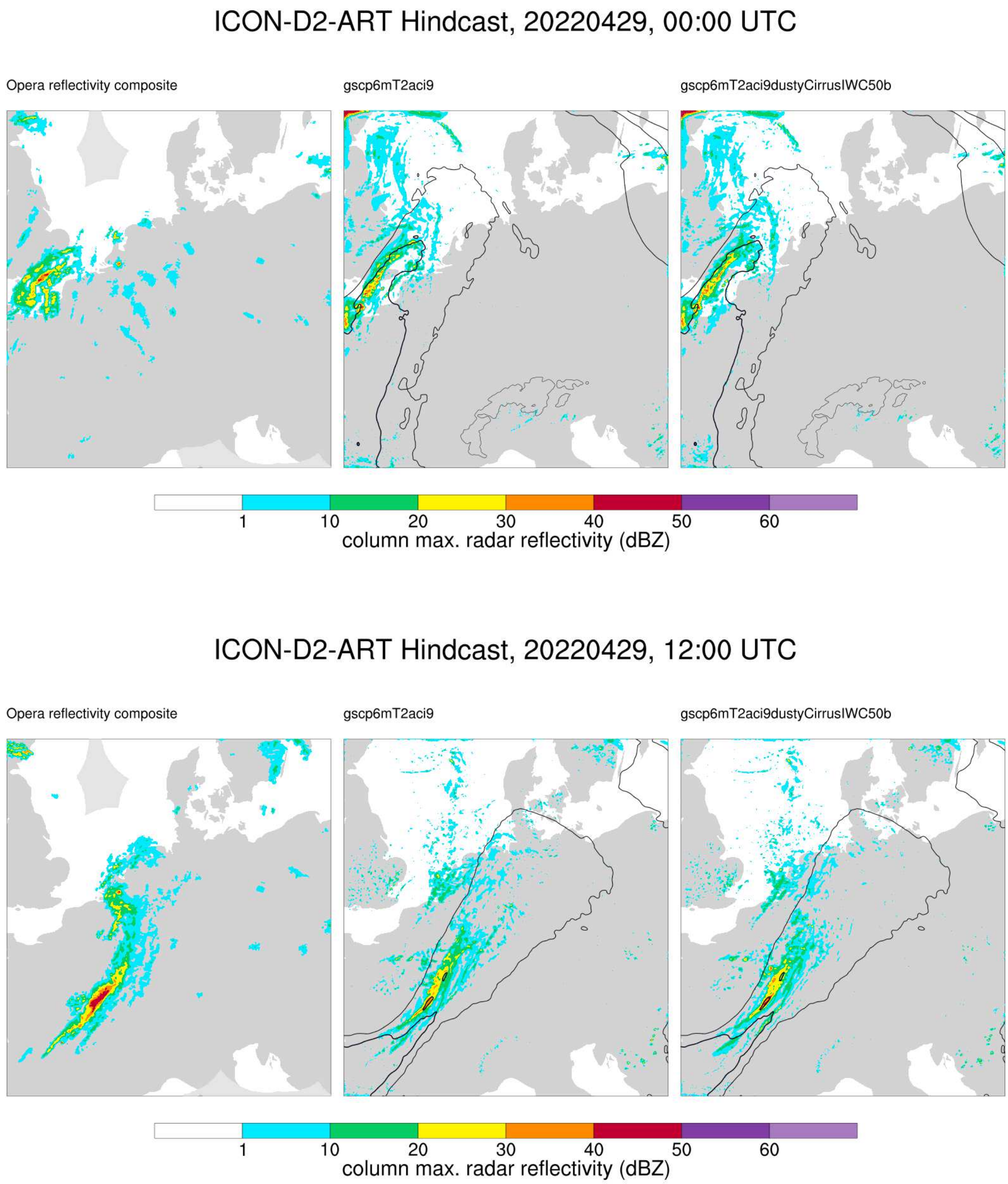

Figure S82. Column-maximum radar reflectivity factor in dBZ for 29 April 2022 00 UTC and 29 April 2022 12 UTC. Shown is the Opera composit (left), the ACI simulation (center), and the ACI-dusty simulation (right). Isolines are the mineral dust AOD at 0.1, 0.2, 0.3 and 0.5

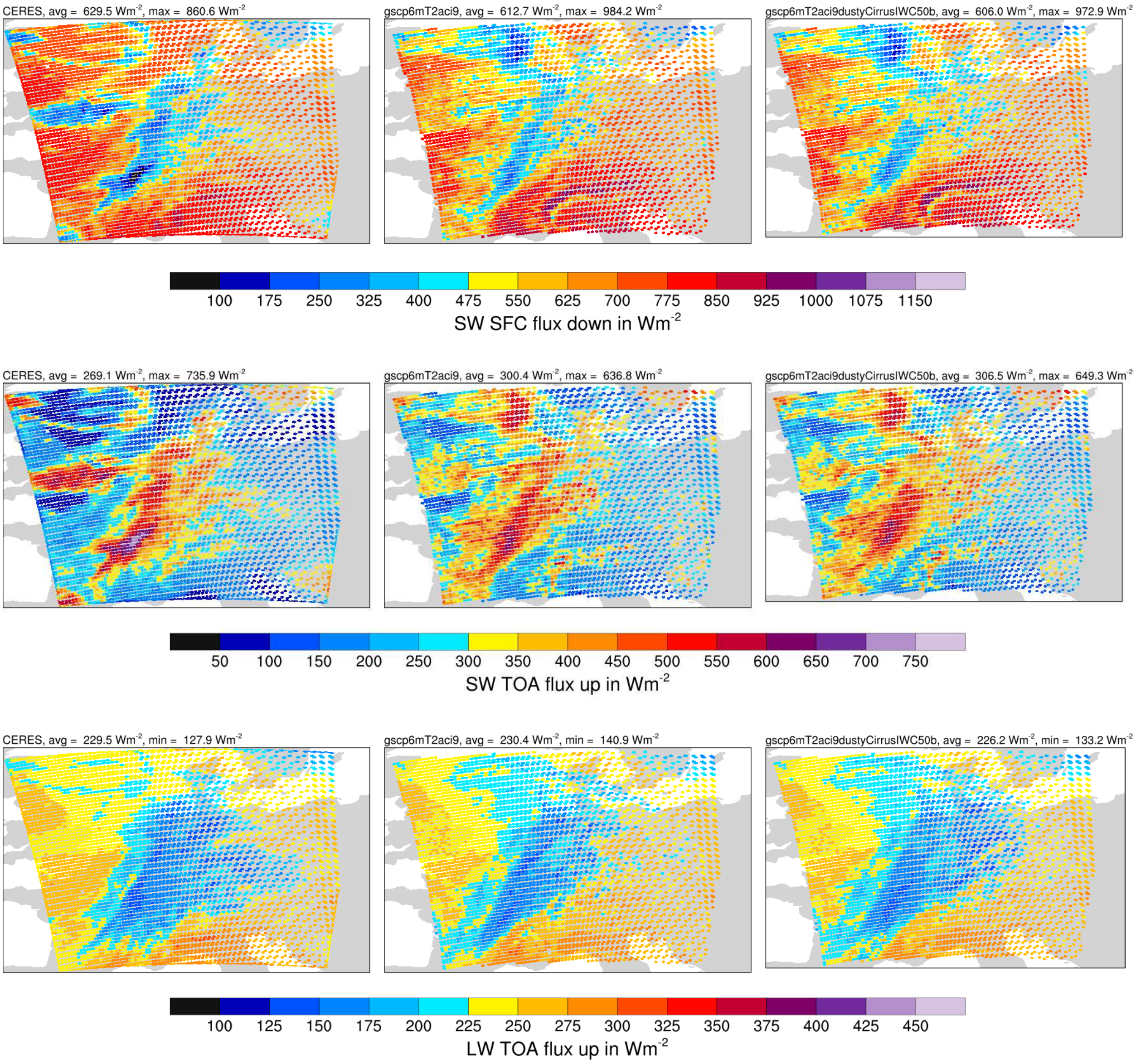

Figure S83. CERES SSF vs ICON-ART for 29 April 2022, 12:50 UTC.

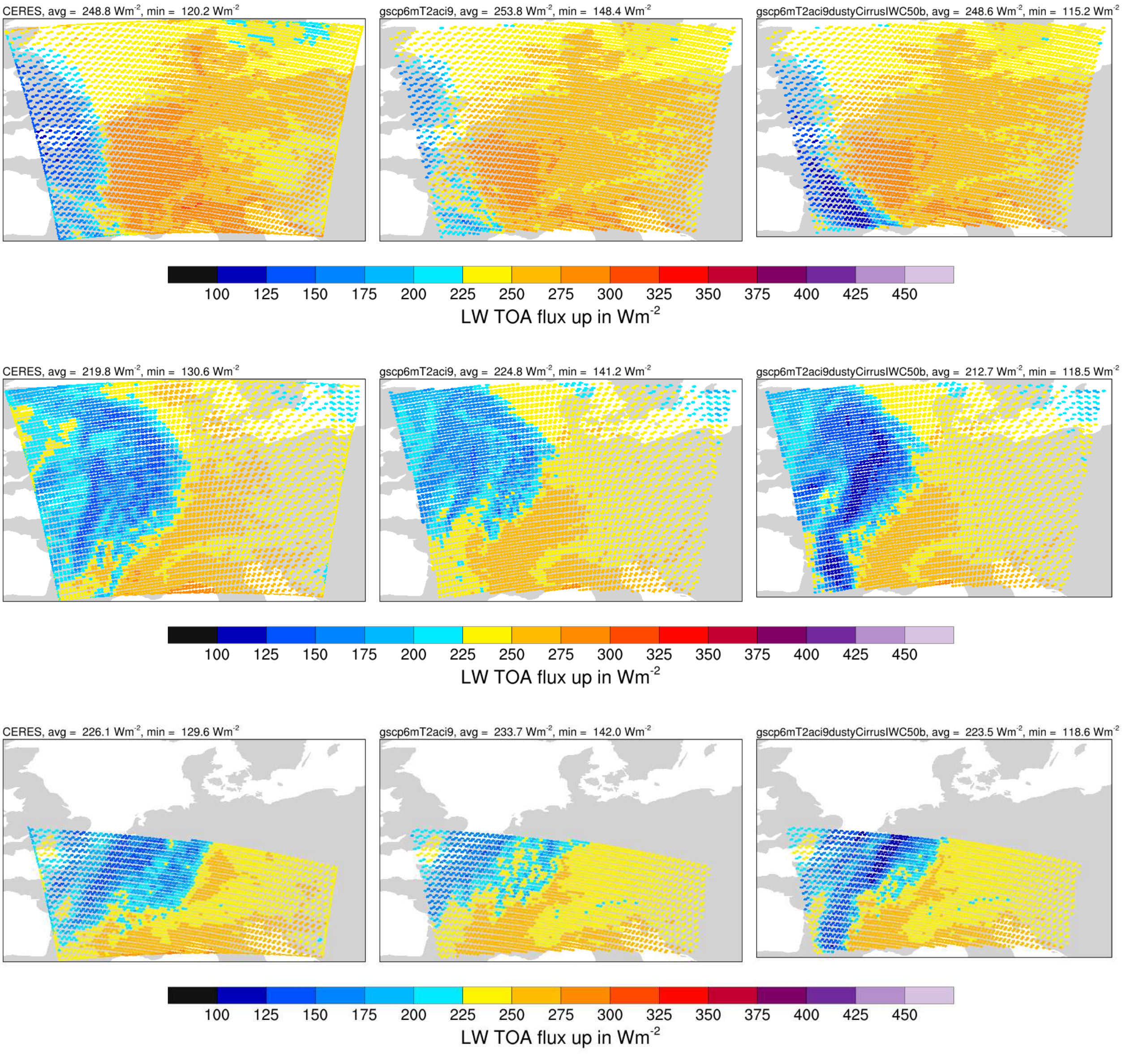

Figure S84. CERES SSF outgoing longwave radiation vs ICON-ART for 28 April 2022 10:17 UTC (top), 28 April 2022 21:28 UTC (middle), and 29 April 2022 01:41 UTC (bottom).

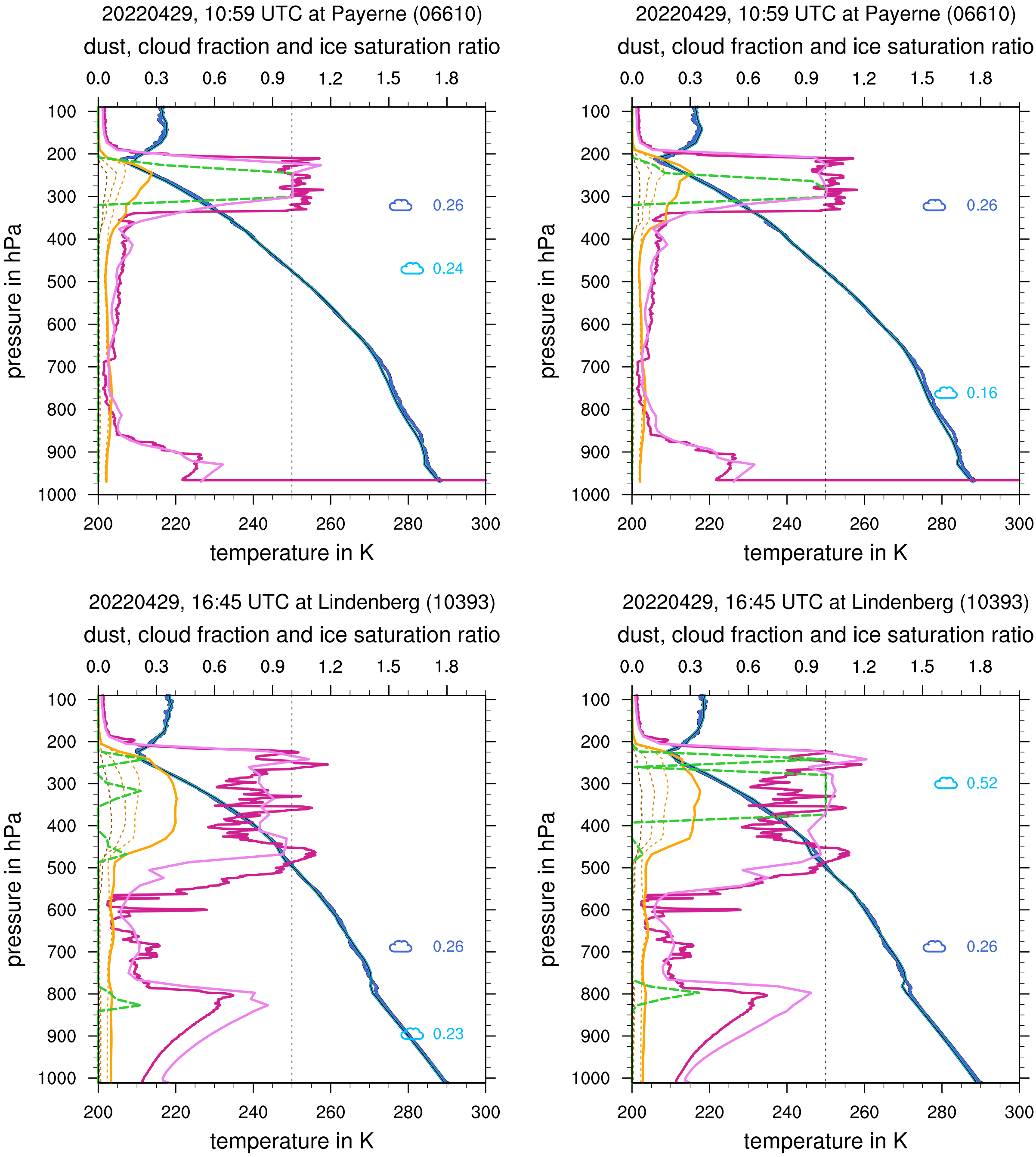

Figure S85. Vertical profiles from radiosonde measurements at Payerne (Switzerland) on 29 April 2022 11 UTC and at Lindenberg (Germany) on 29 April 2022 17 UTC and the corresponding ICON-ART profiles. Observed temperature (black), ICON-ART temperature (blue), observed saturation ratio for ice (dark pink), ICON-ART saturation ratio (lighter pink), normalized total dust concentration of ICON-ART (thick orange), dust modes (other orange and browns), and ICON-ART cloud fraction (green). Cloud symbols indicate the SEVIRI BT (dark blue) and ICON-ART RTTOV BT (light blue) at 10.8 μm for this grid point. Numbers next to the cloud symbol give the visible reflectance (only daytime). Shown are ACI (left) and ACI-dusty (right).

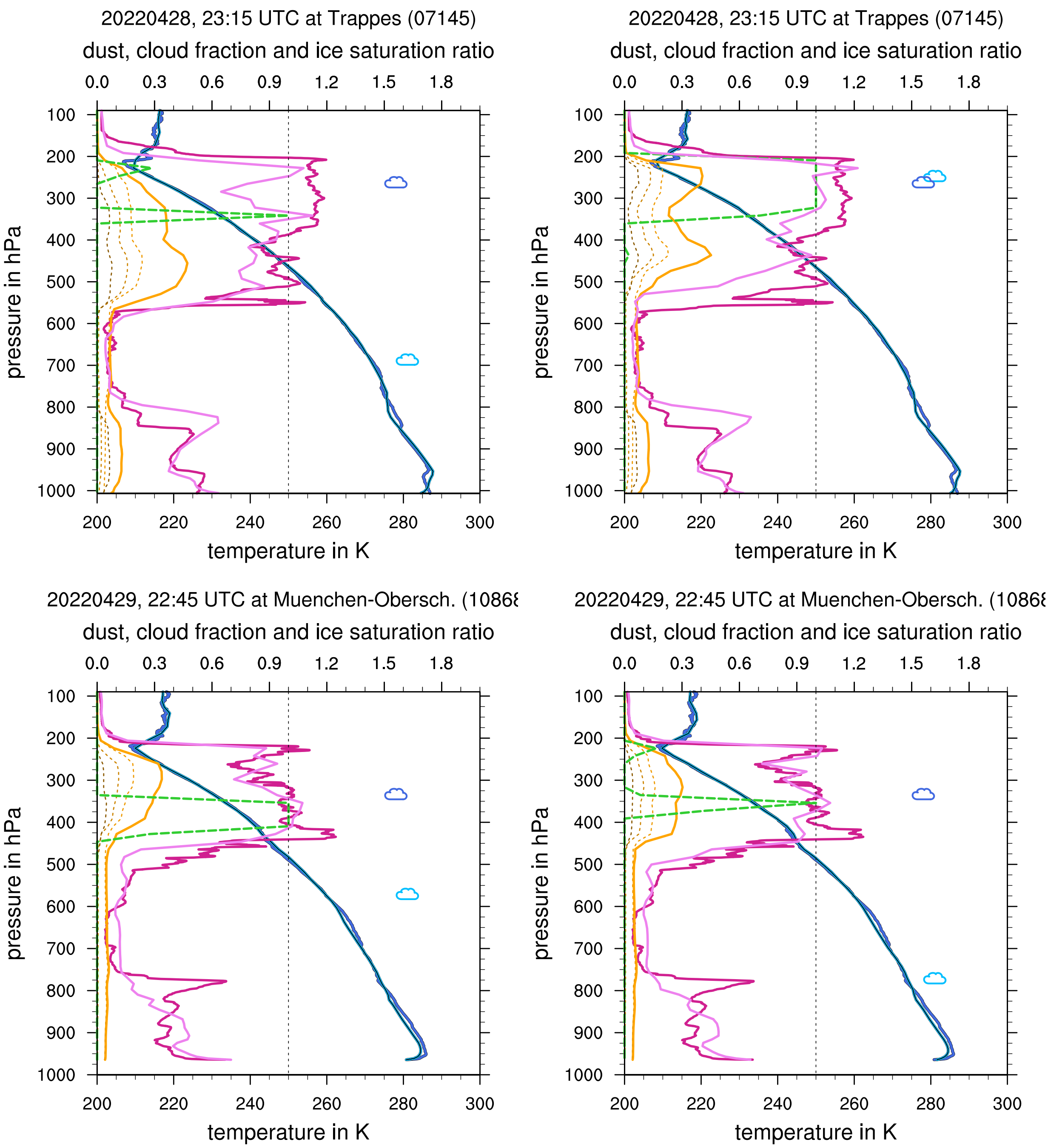

Figure S86. Vertical profiles from radiosonde measurements at Trappes (France) on 28 April 2022 23 UTC and at Munich (Germany) on 29 April 2022 23 UTC and the corresponding ICON-ART profiles. Shown are ACI (left) and ACI-dusty (right).

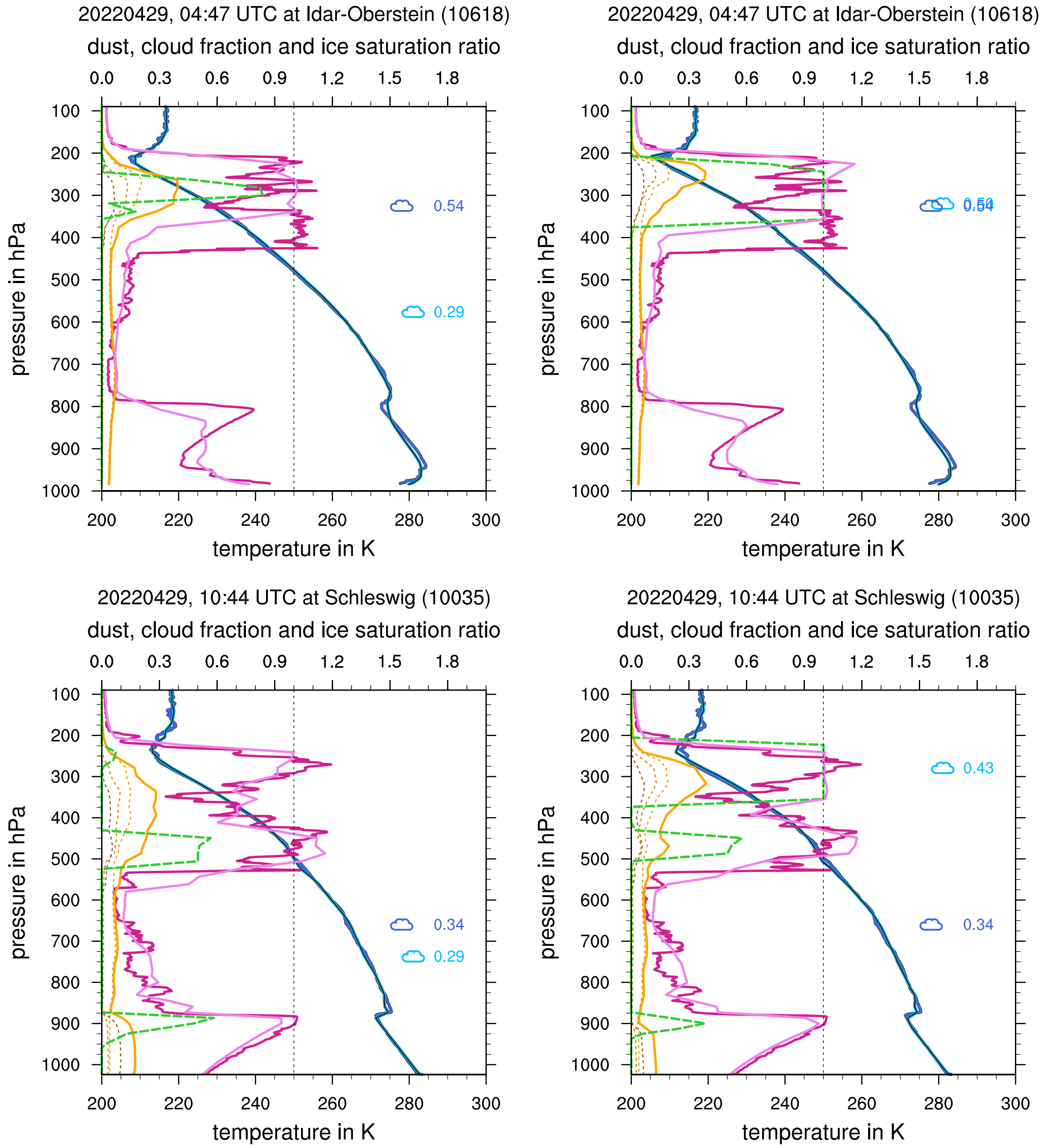

Figure S87. Vertical profiles from radiosonde measurements at Idar-Oberstein (Germany) on 29 April 2022 5 UTC and at Schleswig (Germany) on 29 April 2022 11 UTC and the corresponding ICON-ART profiles. Shown are ACI (left) and ACI-dusty (right).

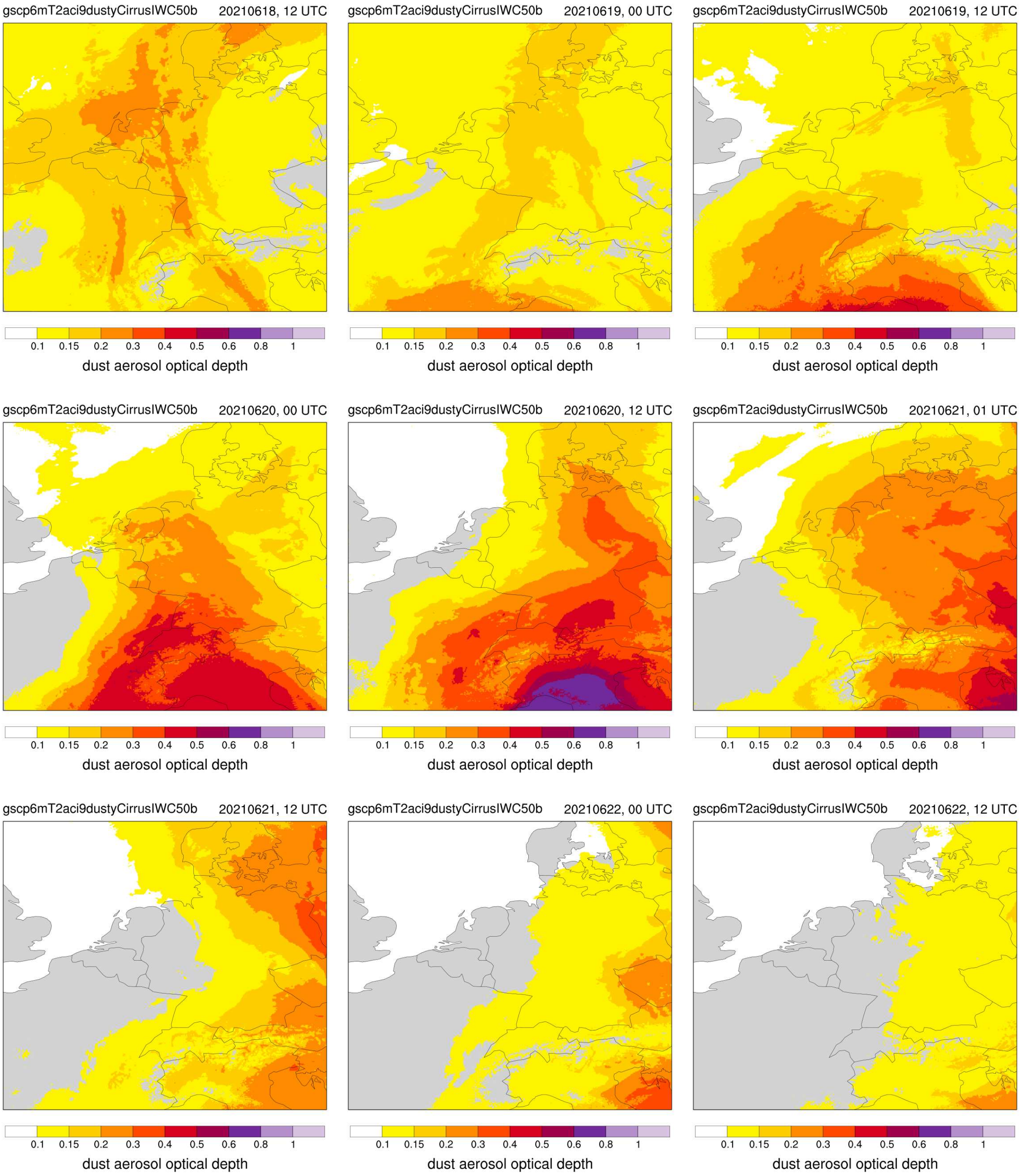

Figure S88. ICON-ART mineral dust AOD for 18-22 June 2021.

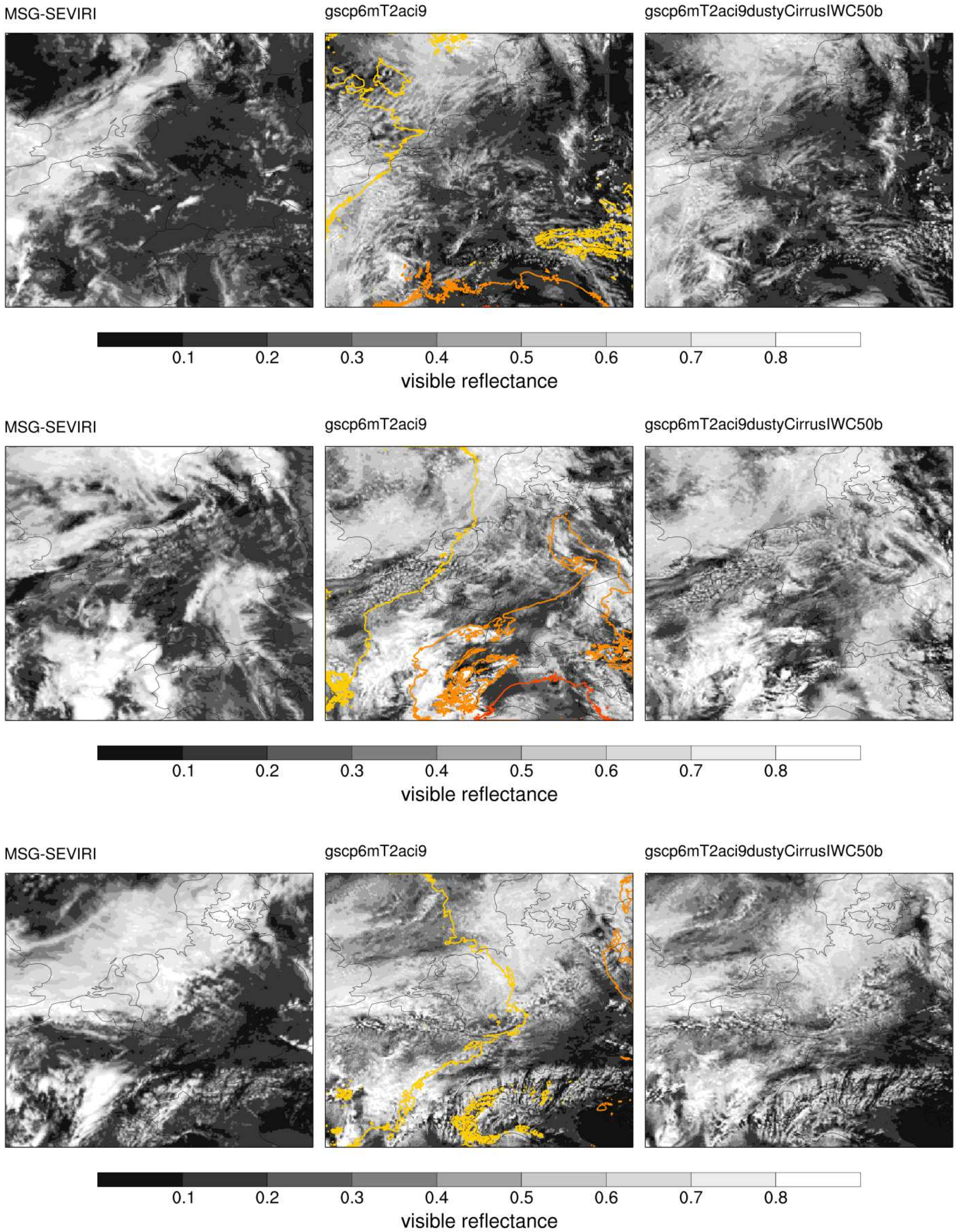

Figure S89. MSG SEVIRI visible reflectance vs ICON-ART for or 19-21 June 2021 at 12 UTC (top to bottom). For ICON-ART the mineral dust AOD is shown with isolines from 0.1 to 0.7 (yellow-orange-red) with intervals of 0.2.

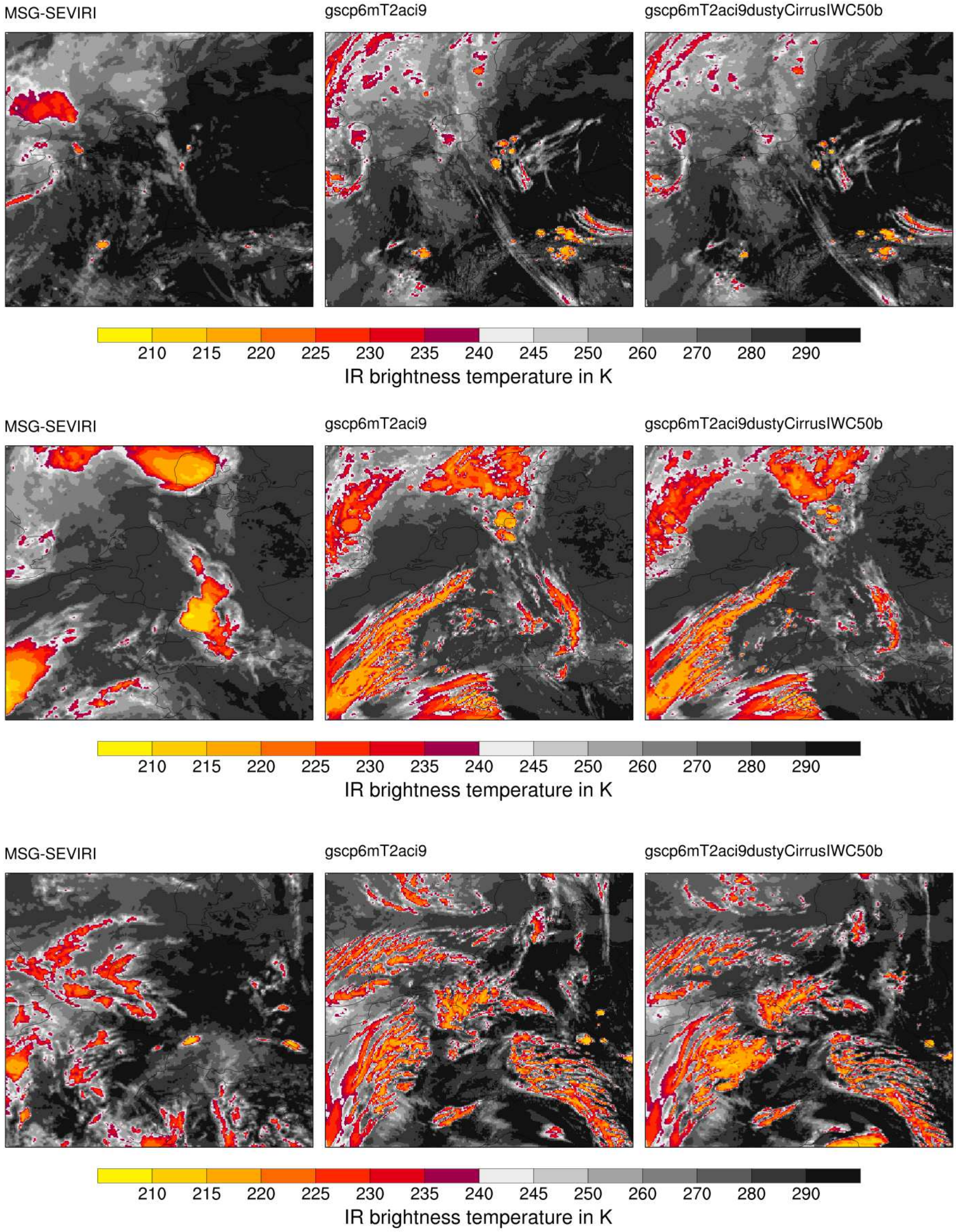

Figure S90. MSG SEVIRI infrared at 10.8 μm vs ICON-ART for 18 June 2021 12 UTC, 19 June 00 UTC and 19 June 12 UTC (top to bottom).

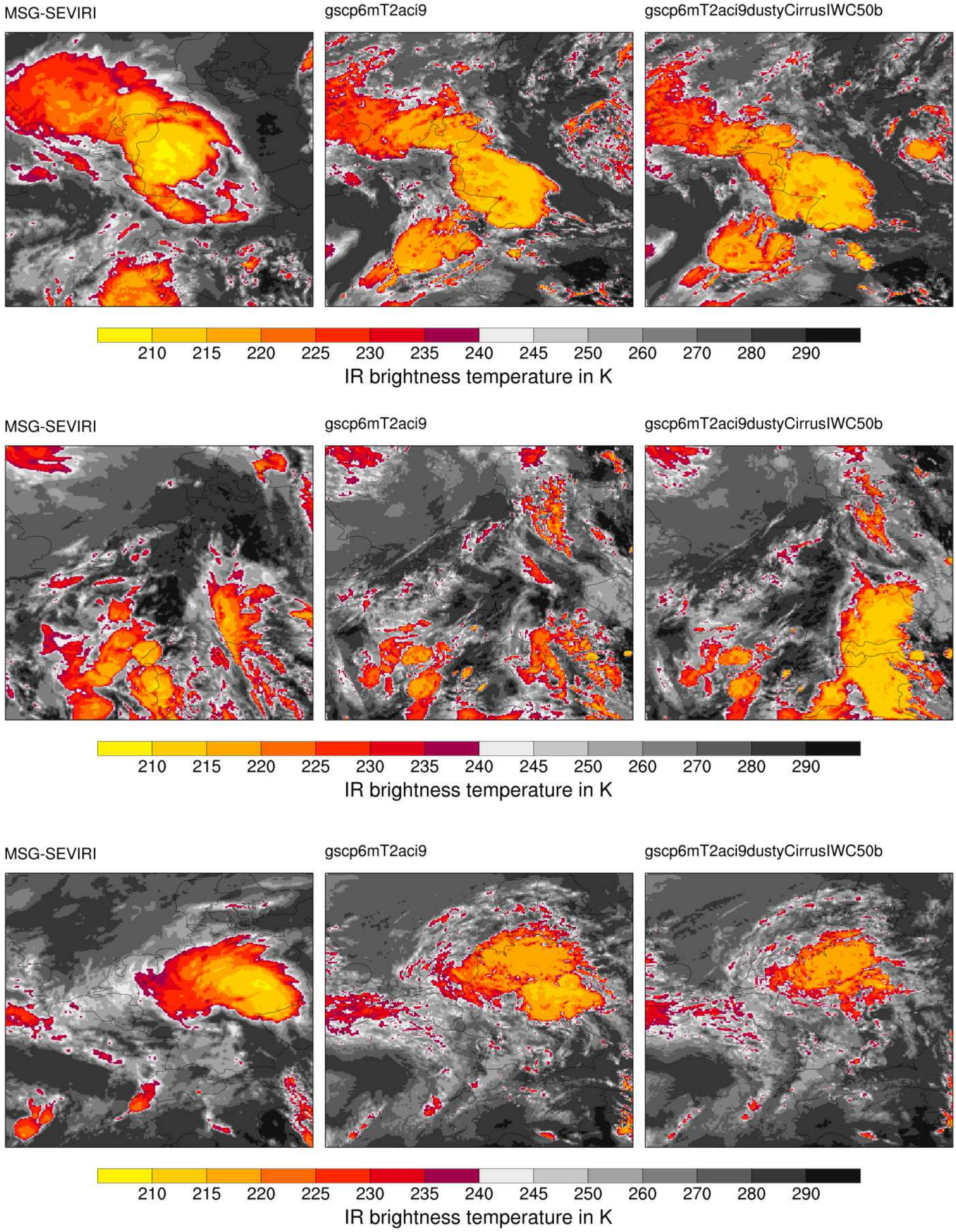

Figure S91. MSG SEVIRI infrared at 10.8 μm vs ICON-ART for 20 June 2021 00 UTC, 20 June 12 UTC and 21 June 01 UTC (top to bottom).

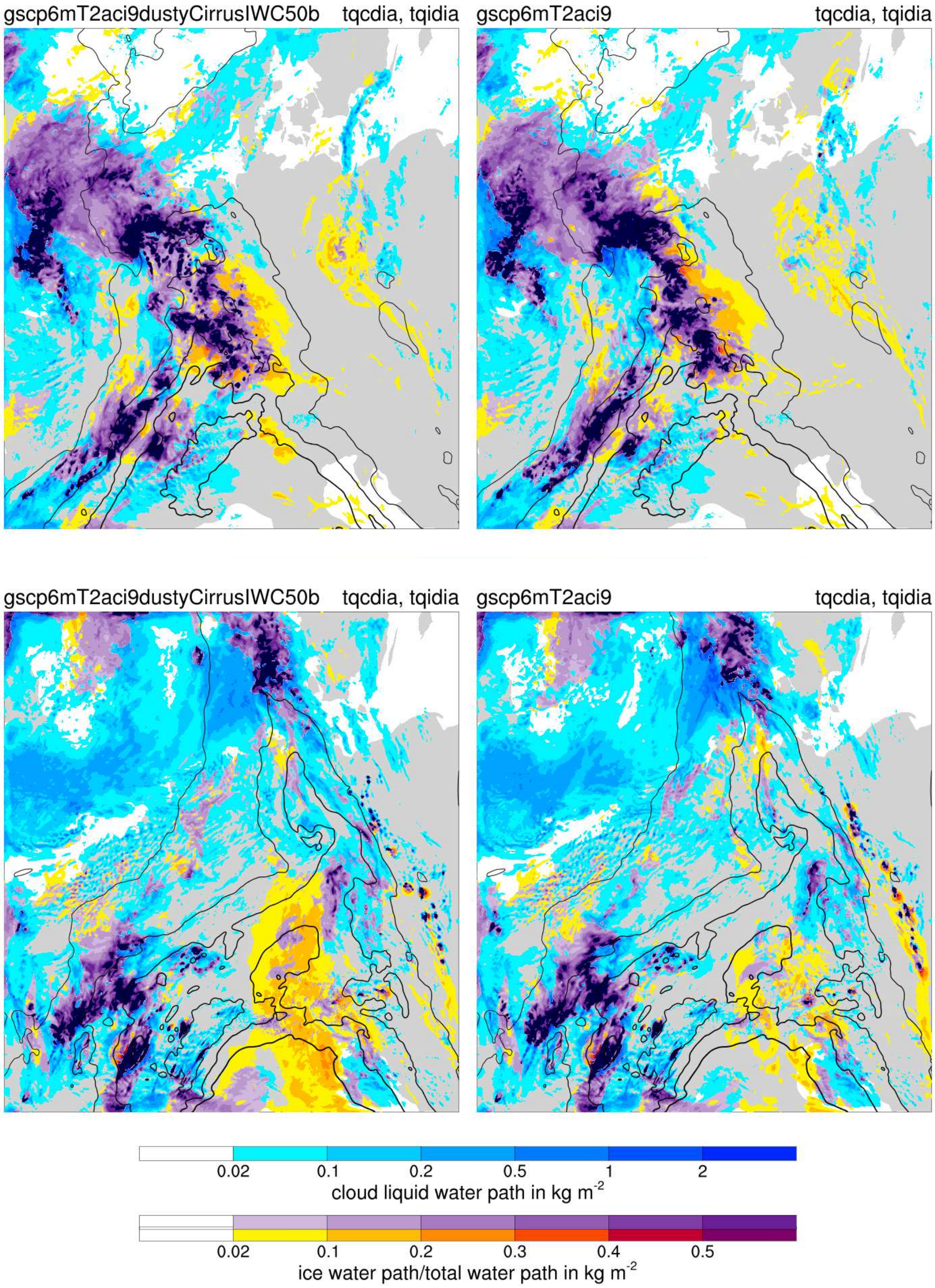

Figure S92. Ice water path (orange-red), cloud water path (blue), and total water path (magenta) for 16 June 2021 12 UTC and 17 June 2021 06 UTC. IWP is shown for column with only ice, LWP for columuns with liquid only, and TWP for column with mixed-phase or multi-layer clouds that contain ice and liquid. The IWP and TWP do include the sub-grid diagnostic contribution, e.g., from the dusty cirrus parameterization. Shown are the ACI (right) and the ACI-dusty (left) simulations of ICON-ART. Isolines are the mineral dust AOD from 0.1 to 0.5 with intervals of 0.1.

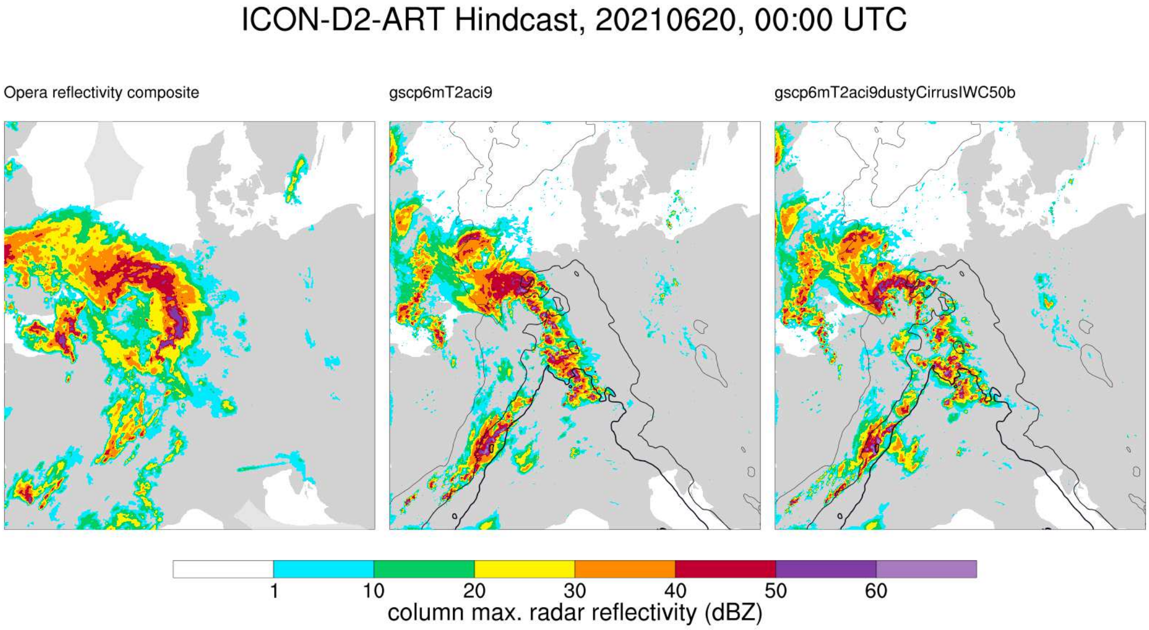

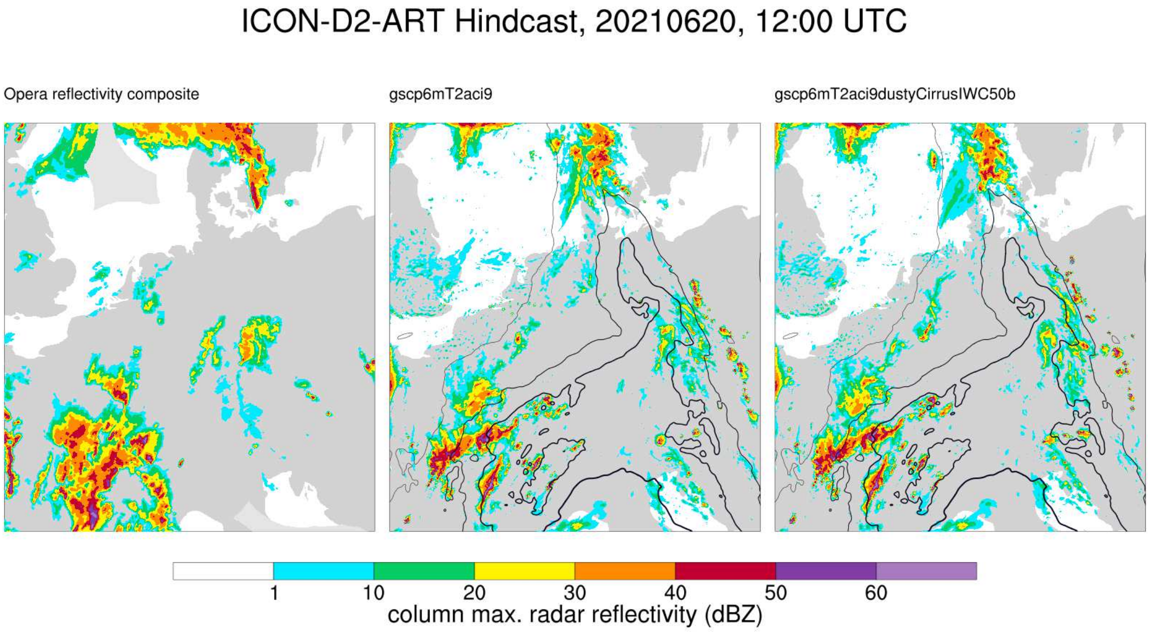

Figure S93. Column-maximum radar reflectivity factor in dBZ for 20 June 2021 00 UTC and 20 June 2022 12 UTC. Shown is the Opera composit (left), the ACI simulation (center), and the ACI-dusty simulation (right). Isolines are the mineral dust AOD at 0.1, 0.2, 0.3 and 0.5

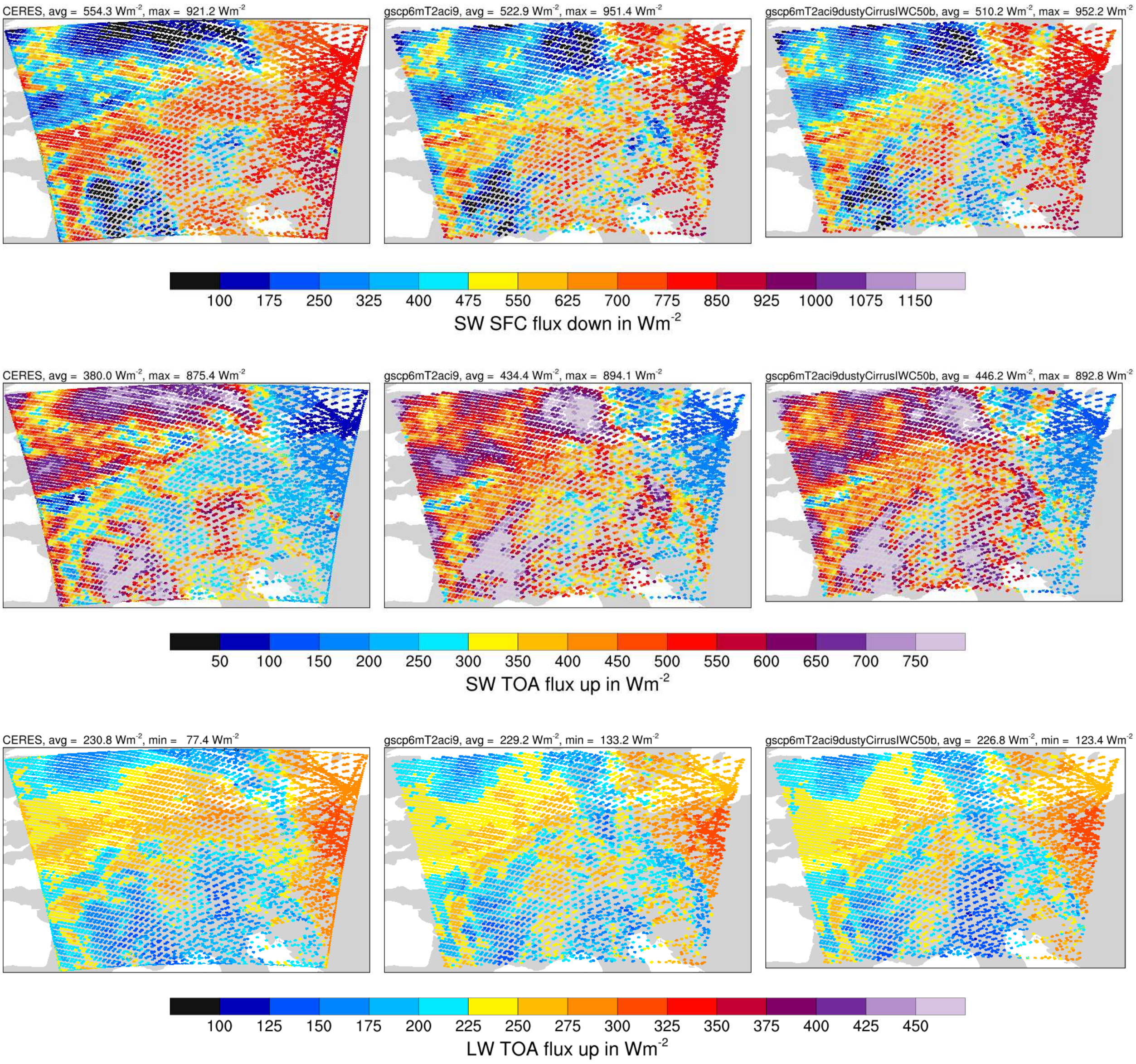

Figure S94. CERES SSF vs ICON-ART for 20 June 2021, 11:15 UTC.

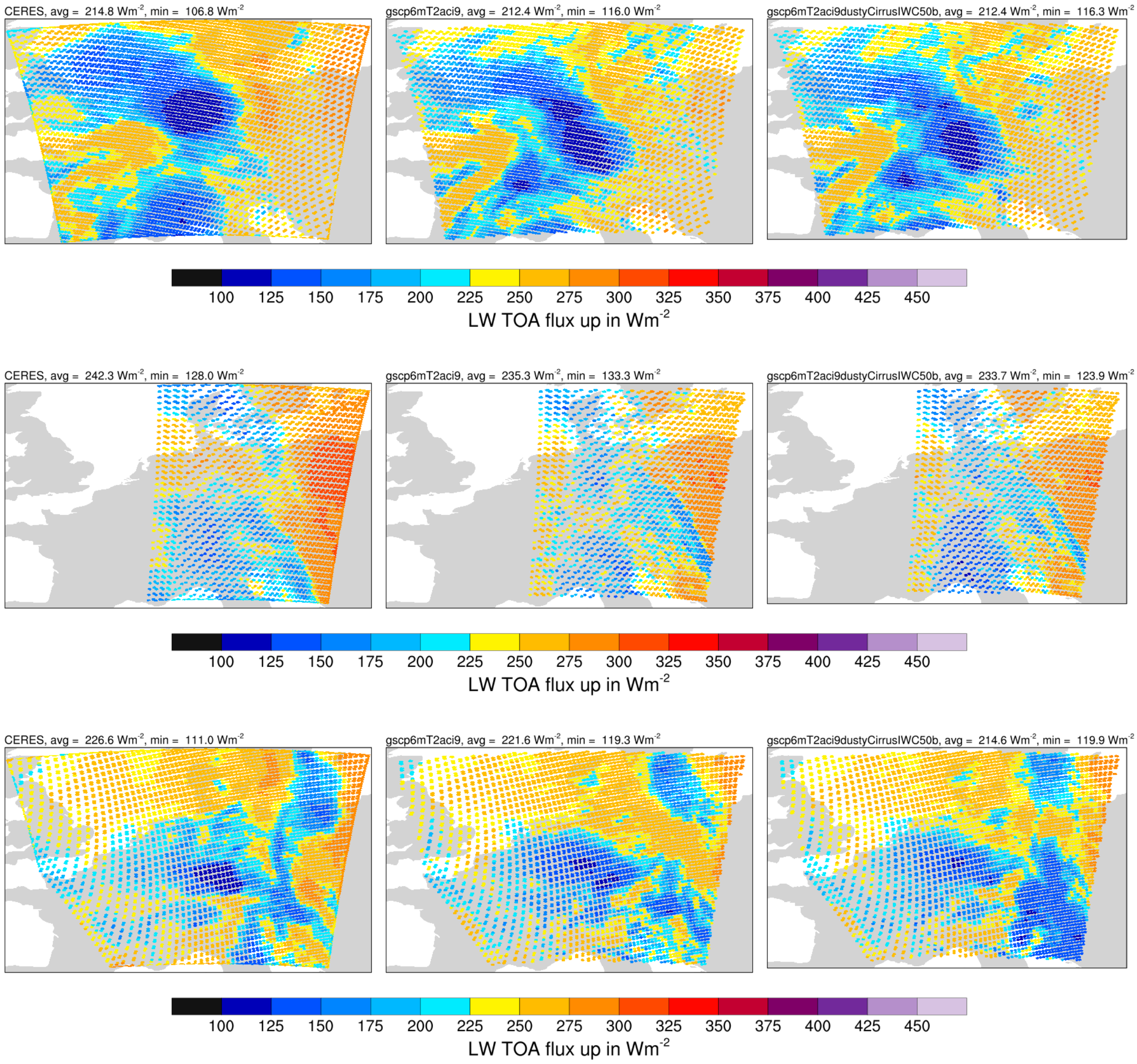

Figure S95. CERES SSF outgoing longwave radiation vs ICON-ART for 20 June 2021 1:50 UTC (top), 9:35 UTC (middle), and 20:46 UTC (bottom).

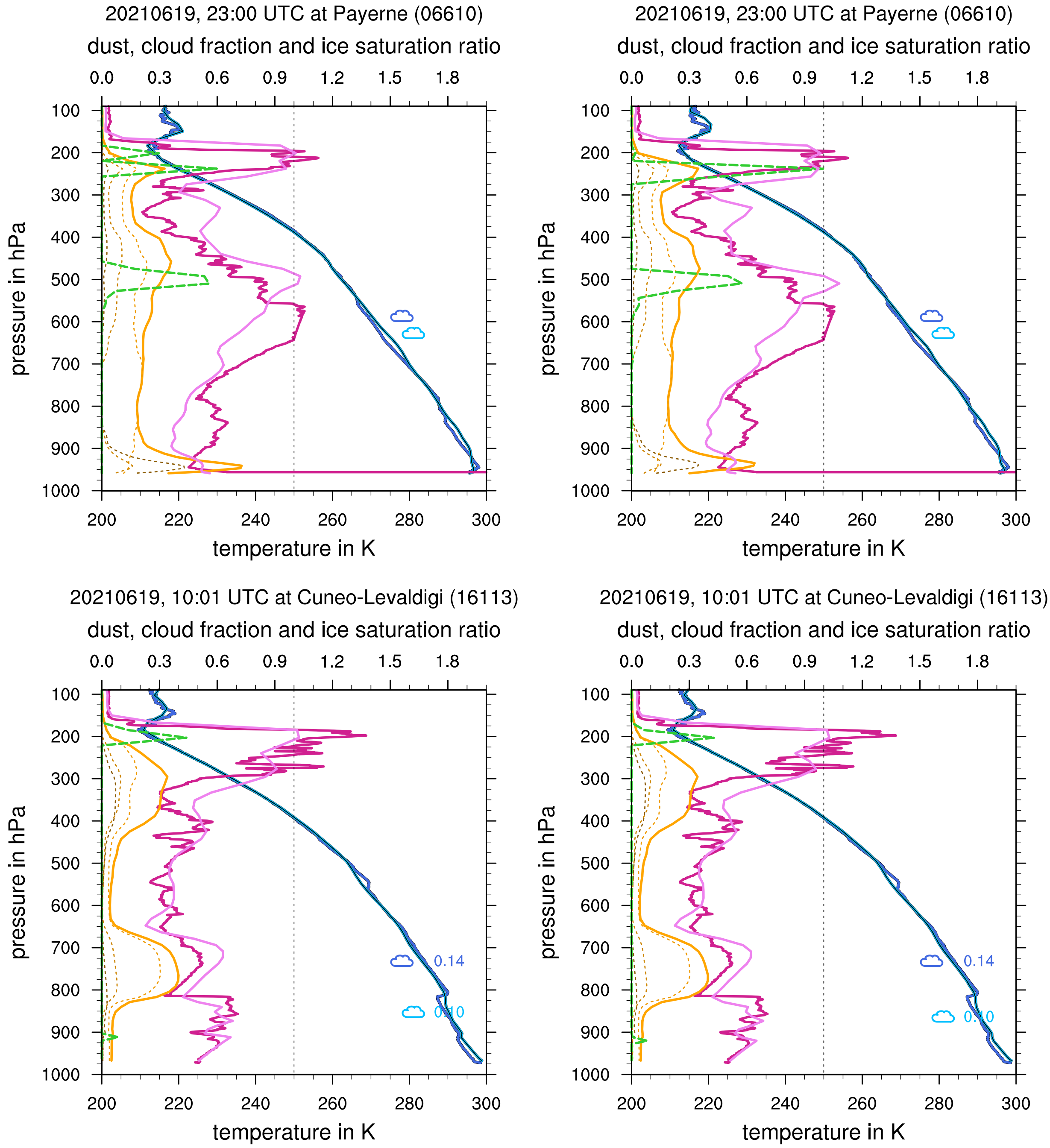

Figure S96. Vertical profiles from radiosonde measurements at Payerne (Switzerland) on 19 June 2021 23 UTC and at Cuneo-Levaldigi (Italy) on 19 June 2021 10 UTC and the corresponding ICON-ART profiles. Observed temperature (black), ICON-ART temperature (blue), observed saturation ratio for ice (dark pink), ICON-ART saturation ratio (lighter pink), normalized total dust concentration of ICON-ART (thick orange), dust modes (other orange and browns), and ICON-ART cloud fraction (green). Cloud symbols indicate the SEVIRI BT (dark blue) and ICON-ART RTTOV BT (light blue) at 10.8 μm for this grid point. Numbers next to the cloud symbol give the visible reflectance (only daytime). Shown are ACI (left) and ACI-dusty (right).

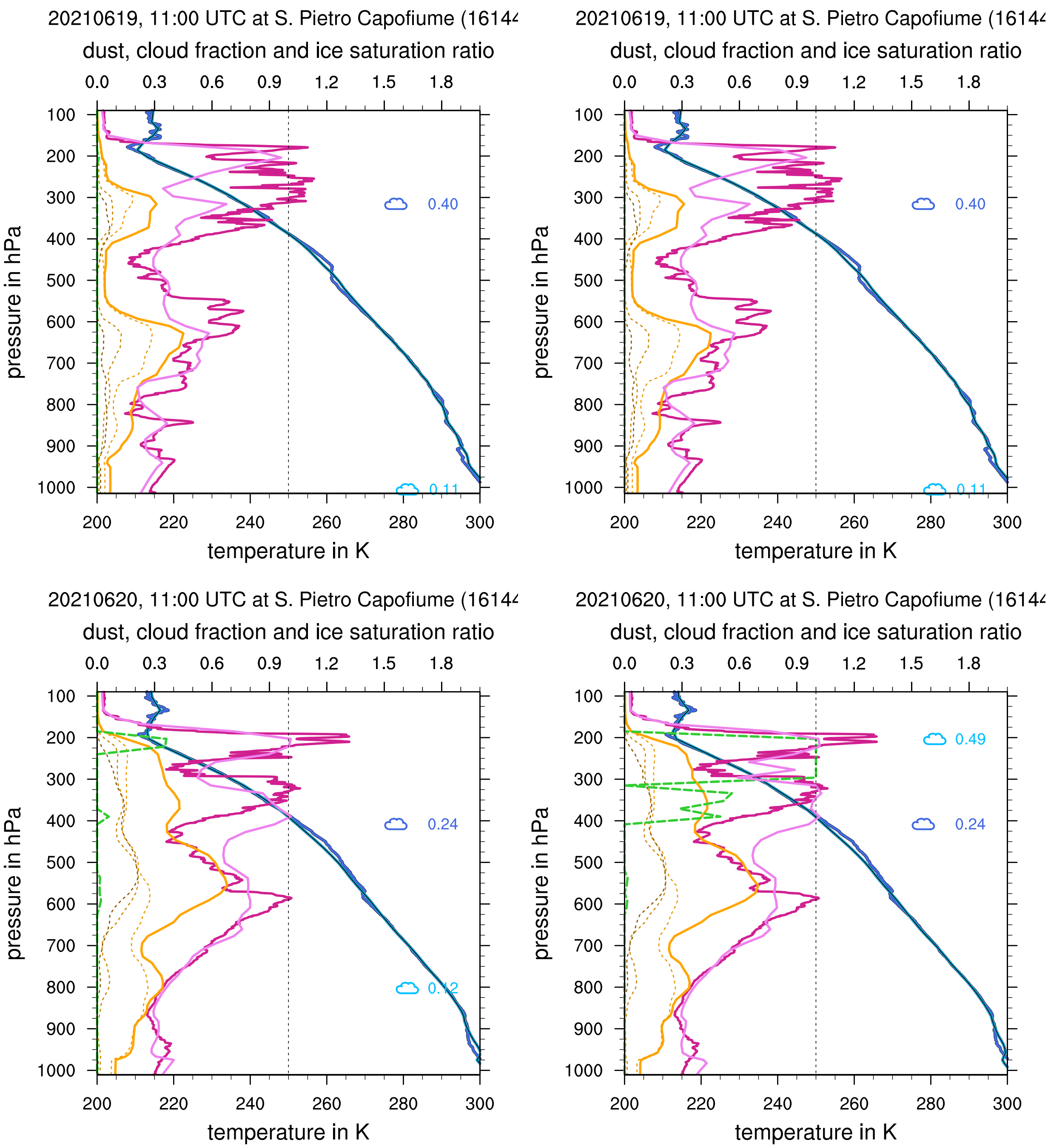

Figure S97. Vertical profiles from radiosonde measurements at S. Pietro Capofiume (Italy) on 19 June 2021 23 UTC and 20 June 2021 11 UTC and the corresponding ICON-ART profiles. Shown are ACI (left) and ACI-dusty (right).

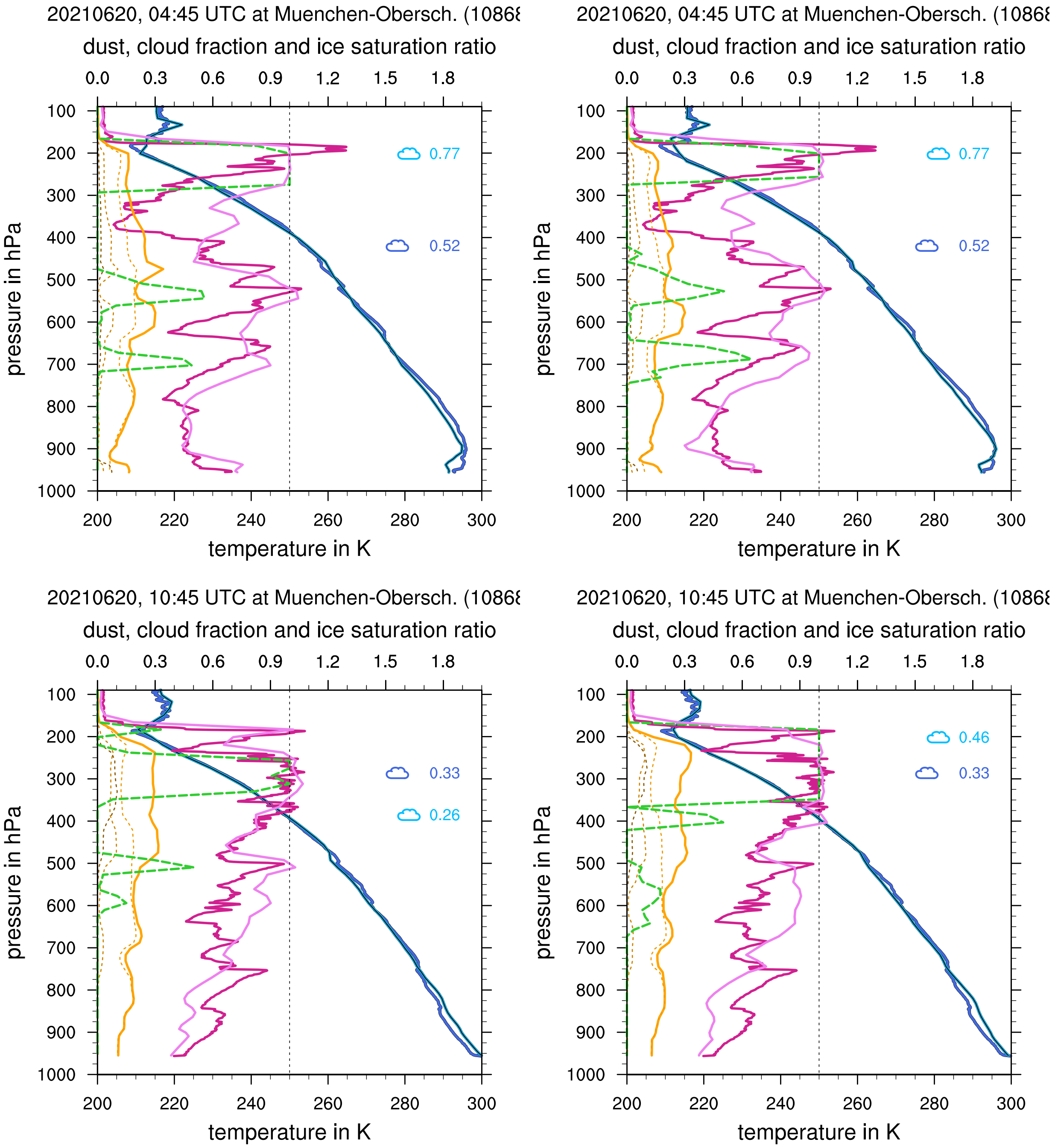

Figure S98. Vertical profiles from radiosonde measurements at Munich (Germany) on 20 June 2021 5 UTC and 11 UTC and the corresponding ICON-ART profiles. Shown are ACI (left) and ACI-dusty (right).

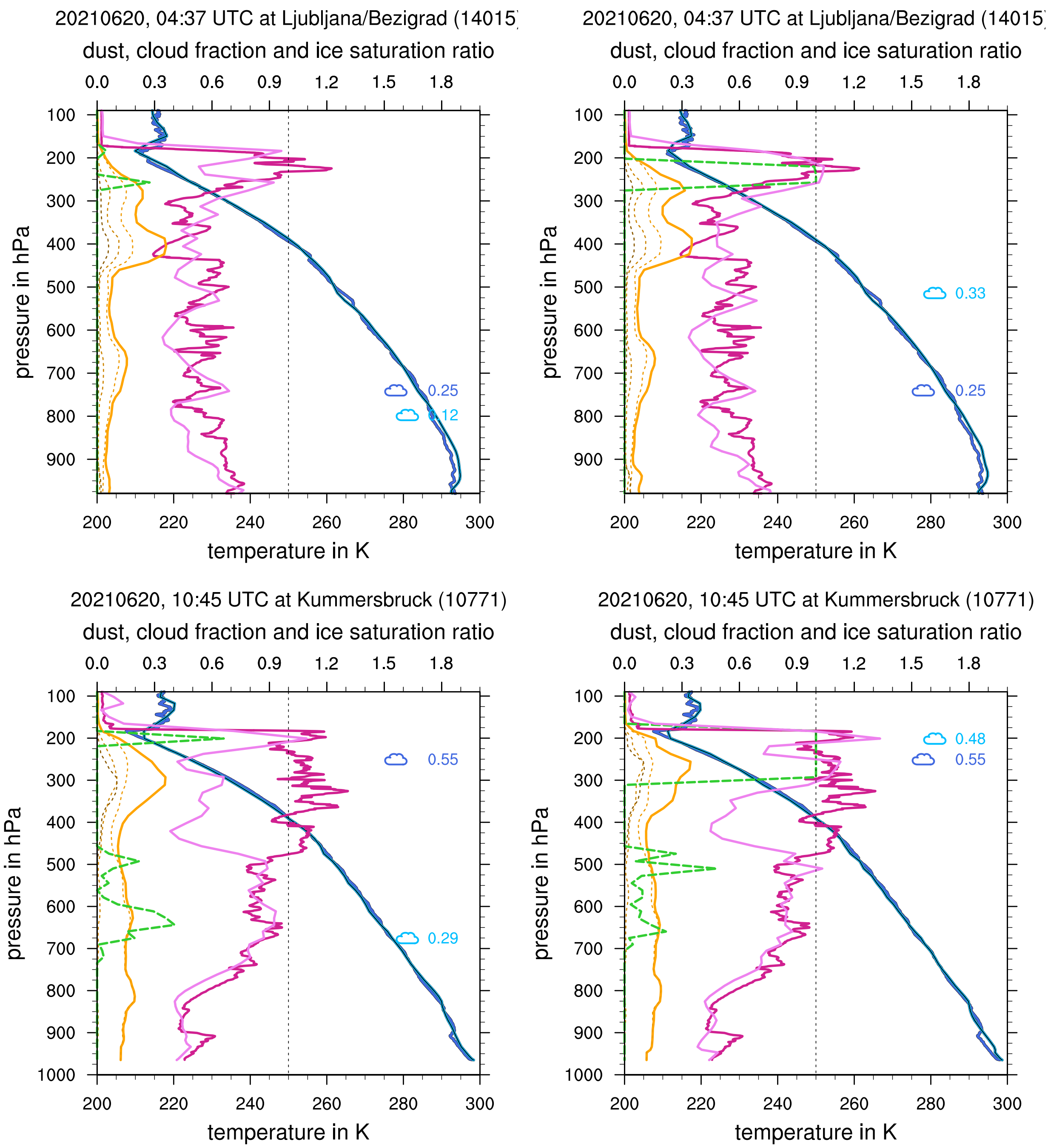

Figure S99. Vertical profiles from radiosonde measurements at Ljubljana (Slovenia) on 20 June 2021 5 UTC and at Kümmersbruck (Germany) on 20 June 2021 11 UTC and the corresponding ICON-ART profiles. Shown are ACI (left) and ACI-dusty (right).

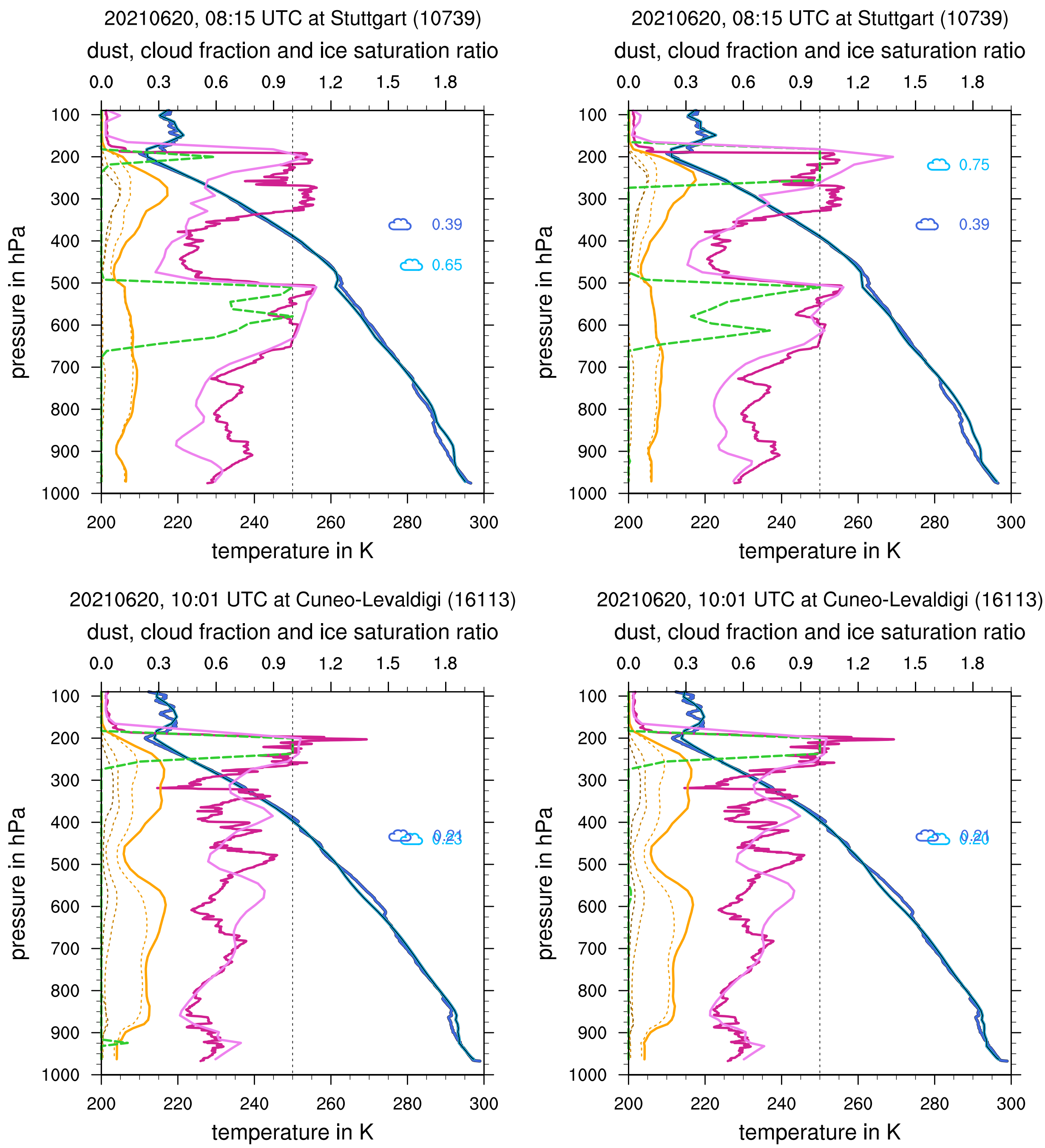

Figure S100. Vertical profiles from radiosonde measurements at Stuttgart (Germany) on 20 June 2021 8 UTC and at Cuneo-Levaldigi (Italy) on 20 June 2021 10 UTC and the corresponding ICON-ART profiles. Shown are ACI (left) and ACI-dusty (right).

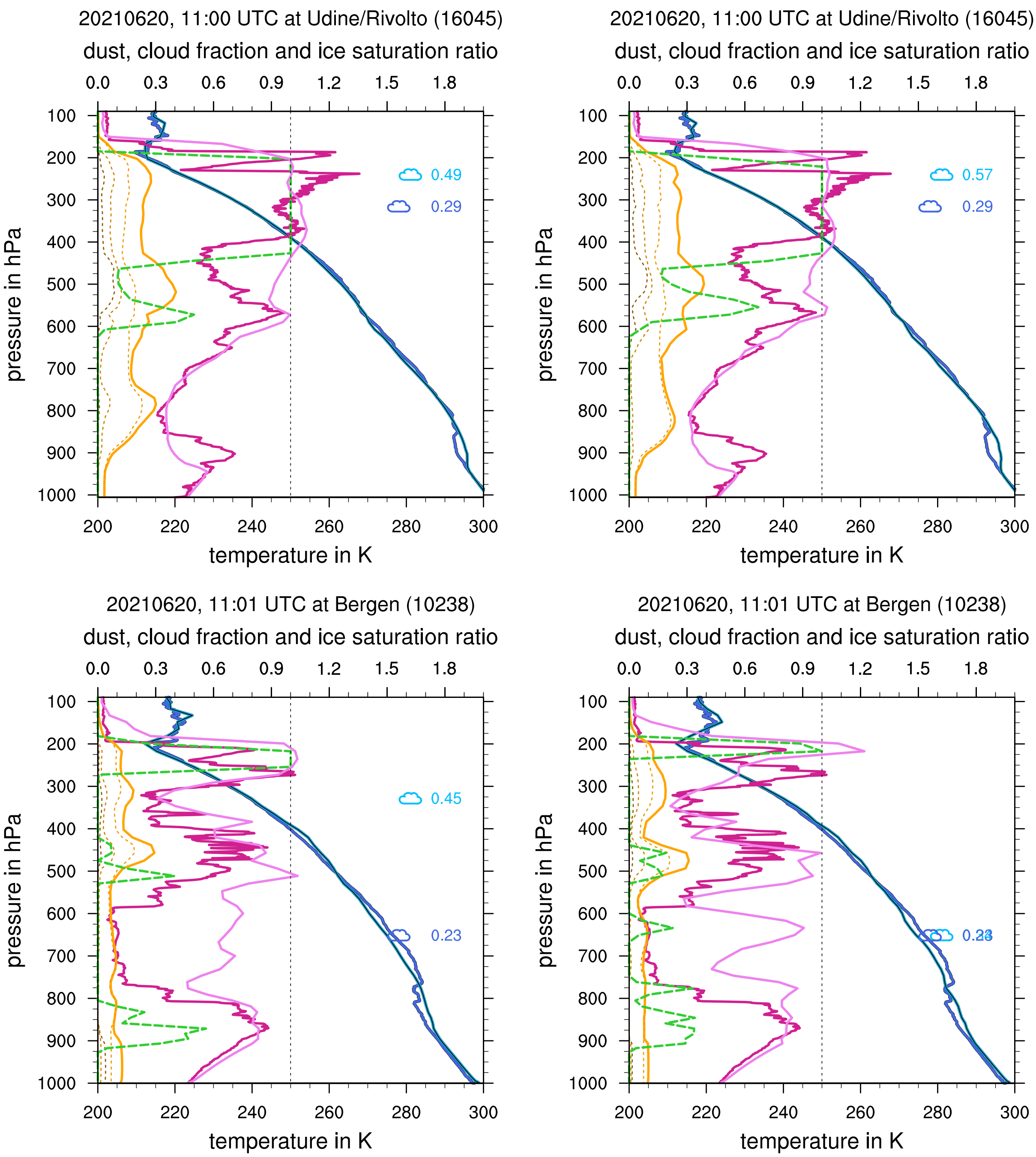

Figure S101. Vertical profiles from radiosonde measurements at Udine-Rivolto (Italy) on 20 June 2021 11 UTC and at Bergen (Norway) on 20 June 2021 11 UTC and the corresponding ICON-ART profiles. Shown are ACI (left) and ACI-dusty (right).